Large Deformation Dynamic Analysis Method for Partially Saturated Elasto-Viscoplastic Soils

2011

Babak SHAHBODAGH KHAN

Abstract

In most of the geotechnical problems there are several complexities which make the computational analysis of earth structures complicated. First, geomaterials usually fall into the field of multiphase porous materials. Second, the constitutive behavior of soil is nonlinear and rate-dependent. Third, most of earth structures must be designed and constructed to resist the effects of large ground motions. Finally, they can experience large deformation during large ground motions.

The main objective of this study is to develop a method to concern all the four mentioned challenges in computational geomechanics. In this study, a cyclic elasto-viscoplastic model and its application is presented to simulate the behavior of fully saturated and partially saturated soil specimens under cyclic triaxial loading conditions. In the constitutive model, the skeleton stress and suction are adopted as the basic stress variables. The collapse behavior, which occurs with a decrease in suction, is considered with the shrinkage of the overconsolidation boundary surface, the static yield function, and the viscoplastic potential surface.

In this research, the finite element formulation suitable for large deformation dynamic analysis is extended to the case of multiphase materials. Base on the formulation, a new computer program entitled "COMVI3D-DY011" is developed for the large deformation dynamic analysis of partially saturated elasto-viscoplastic soils.

Using "COMVI3D-DY011", the dynamic strain localization phenomenon in saturated and partially saturated clay is studied. In addition, mesh-size dependency is analyzed to provide stable and convergent solutions. Also, the effects of the initial suction, loading rate, and confining pressure on shear band development are studied and discussed. By comparing the saturated and partially saturated cases, it is seen that in partially saturated clay the strain localizes more prominently, and more brittleness, i.e. strain softening, is observed due to the collapse of suction force caused by shearing.

In this dissertation, the potential failure modes affecting embankments as a consequence of earthquake shaking is, also, presented and discussed. Furthermore, the seismic behavior of a partially saturated embankment on non-liquefiable soft clay is numerically studied in two cases with different ground water levels. As the results of this simulation, the subsidence of the crest and lateral stretching is observed in the embankment.

Acknowledgements

The task of undertaking a PhD education requires a lot of sacrifice and support from many people. I have been fortunate to have the support of teachers, friends and family, and it is a pleasure to express my gratitude to all these people.

First and foremost, I would like to express my profound gratitude and appreciation to my supervisor, Professor Fusao Oka, for his invaluable advice and encouragement, and his continuous and generous support throughout my PhD study. Without his guidance and support, based on his deep insight and experience in the field of geomechanics and geotechnical engineering, this work could not have been completed. I owe him not only for this study, but also for extending his help on various aspects of my life in Japan.

I am also deeply indebted to Associate professor Sayuri Kimoto for her valuable suggestions and advice during my doctoral research. In addition, I have greatly benefited by constructive advice and help from Assistant Professor Yosuke Higo, which I would like to appreciate it. I gratefully thank Ms. Chikako Itoh, secretary of Oka laboratory, who has been so kind in assisting me with all Japanese daily life matters during three years of my stay in Japan.

My appreciation is also extended to the member of the dissertation committee, Professor Takeshi Katsumi, for his advice and suggestions as well as for his time and efforts in reviewing this thesis.

I appreciate the students of Oka laboratory for their friendship, assistance, and support. In particular, I would like to thank my friends Dr. Edwin Garcia, Dr. Mojtaba Mirjalili, and Mr. Hamidreza Sadeghi with whom I spent the most time during the years of my stay in Kyoto. Their valuable friendship, support, and encouragement are greatly appreciated. I would like to extend also my gratitude to the foreign students: Dr. Quoc Huy Nguyen, Ms. Ana Paula Ribeiro, and Mr. Chung Won Lee with whom I shared great time in Kyoto.

I would like to express my thanks to the financial support provided by the Ministry of Education, Science and Culture, Government of Japan (MONBUSHO), which made this

study possible.

My most deeply-felt gratitude goes to my family in Iran for all their love, support, and faith in my entire life and in particular during my study abroad in Kyoto University, and I dedicate this dissertation to them.

Kyoto, August 2011
Babak Shahbodagh Khan

Table of Contents

List of Figures

List of Tables

Chapter 1

INTRODUCTION

1.1 Background and Objectives

Predicting the response of structures under various loading conditions is the major key to design the safe and economical structures. In most of the geotechnical problems, however, there are several complexities which make the computational analysis of earth structures less straightforward. First, geomaterials usually fall into the field of multi-phase porous materials. They are composed of soil particles, water and gas. Therefore, any comprehensive analysis must take into consideration the interaction among these various phases. Second, the constitutive behavior of soil is nonlinear and rate-dependent. Third, most of earth structures must be designed and constructed to resist the effects of large ground motions. This presence of the inertia forces in the different phases makes the solution of the coupled system computationally demanding. Finally, large deformations often take place during the large ground motions; hence, the widely used infinitesimal strain theory cannot be applied to the analysis. The main objective of this study is to develop a mathematical framework to concern all the four mentioned challenges in computational geomechanics.

Using the theory of porous media is essential in most of the geotechnical problems, where the interactions between the constituent phases have significant effects on the mechanical behavior of geomaterials. The modern concept of mixture theory was first established by Paul Fillunger (1936). Fillunger introduced the volume fraction concept, and he formulated the balance of mass and momentum as the foundations of porous media theory. The two-phase coupled mixture theory was further developed by Maurice Biot (1956, 1962) for quasi-static and dynamic analyses. Over the last fifty years, several researchers

have described the partially saturated porous solid materials within the theory of porous media to produce the behavior of partially saturated soils (e.g., Atkin and Craine, 1976; Bowen, 1976; Coussy, 2004; de Boer, 1998; Ehlers, 2003). In case of partially saturated soils, the relationship between the degree of saturation and suction, namely, the soil water characteristic curve is, also, required in order to complete the coupled multiphase governing equations (Houlsby, 1997). A finite element model based on two-phase mixture theory was presented by Oka et al. (2001) for the analysis of fully saturated earth structures in the regime of finite deformation with an updated Lagrangian description. Based on this model, Oka et al. (2001) developed the computer program "LIQCA3D-FD" for the three-dimensional analysis. In this dissertation, the finite element formulation is extended for partially saturated soils based on the multiphase mixture theory, and the new computer program entitled "COMVI3D-DY011" is introduced for the large deformation dynamic analysis of partially saturated elasto-plastic and elasto-viscoplastic soils. In this study, a van Genuchten type of equation is employed as a constitutive equation between the saturation and the suction (van Genuchten, 1980).

To analyze unsaturated soils, it is necessary to choose appropriate stress variables. Bishop (1960) proposed an effective stress equation for unsaturated soils; however, this effective stress concept cannot provide the explanation for the collapse phenomenon (Jennings and Burland, 1962). To reflect the collapse behavior, researchers (Bishop and Donald, 1961; Coleman, 1962; Matyas and Radhakrishna, 1968; Fredlund and Morgenstern, 1977) have suggested the independent stress variable approach, where two stresses are proposed for both the soil particles and the fluids. According to their studies any pair of stress fields among the following three stress states, $(\sigma_{ij} - u_a\delta_{ij})$, $(\sigma_{ij} - u_w\delta_{ij})$, and $(u_a - u_w)\delta_{ij}$, can be applied as a suitable stress framework to describe the stress-strain-strength behavior of partially saturated soils. The adoption of net stress $(\sigma_{ij} - u_a\delta_{ij})$ is valid for dry soil and unsaturated soil only when the air pressure is thought to be constant. However, drained conditions for water and air cannot always be attained in engineering problems. Alternatively, other generalized effective stress formulations have also been used to explain the collapse phenomenon (e.g., Bolzon et al., 1996; Khalili and Khabbaz, 1998; Loret and Khalili, 2000; Kohgo et al., 2001). Most of these models are defined by the generalized effective stress concept with the introduction of a new constitutive parameter for the effective stress. Recently, the terms "effective stress" (Bolzon et al. 1996; Houlsby, 1997; Ehlers, 2004), "Average soil skeleton stress" (Jommi, 2000; Oka et al., 2006; Wheeler et al., 2003), "Generalized effective stress" (Laloui and Nuth, 2009),

and "Skeleton stress" (Oka et al., 2008, 2010), which are consistent with a view point of the multiphase mixture theory, have been used where the skeleton stress averaged over the total mixture volume. Note that Oka et al. (2010) used "Skeleton stress" instead of "Average soil skeleton stress" to avoid confusing with the mean skeleton stress.

The ability of a nonlinear computational analysis to provide realistic simulations of the behavior of soil depends on the capability of the constitutive model used to describe the mechanical response of the soil. One of the most important reasons that the prediction of the dynamic responses of partially saturated earth structures is complex is the non-linear, suction-dependent, time-dependent and cyclic behaviors of soil. This becomes even more complicated as the destructuration and microstructural changes in the soil particles are taken into consideration. During last twenty years, Many constitutive models have been proposed for unsaturated soils (e.g., Alonso et al., 1990; Wheeler and Sivakumar, 1995; Wheeler and Karube, 1995; Cui and Delage, 1996; Thomas and He, 1998; Muraleetharan and Nedunri, 1998 ; Muraleetharan and Wei, 2000; Sheng et al., 2003, Oka et al., 2008; Nuth and Laloui, 2008). Most of the models, however, are within the framework of rate-independent model, such as elasto-plastic models, or they can only describe the rheological behavior of soils under static loading conditions. Oka (1992) developed a cyclic elasto-viscoplastic constitutive model for clay based on nonlinear kinematic hardening rule (Chaboche and Rousselier, 1983). Later on, Oka et al. (2004) proposed a cyclic viscoelastic-viscoplastic model by incorporating the viscoelastic feature into the constitutive equations, in which the behavior of clay can be described not only in the range of middle to high level of strain, but also in the range of low level of strain. Despite the ability of these models to explain the deformation characteristics under cyclic loading conditions, the effect of structural degradation of clay particles was disregarded. Taking into account the structural degradation and microstructural changes, a cyclic elasto-viscoplastic model was developed based on the nonlinear kinematic hardening rules for the changes in both the stress ratio and the mean effective stress (Hoizumi 1996, Watanabe et al. 2007). In order to improve the prediction of the behavior during cyclic loading process, the nonlinear kinematic hardening rule for changes in viscoplastic volumetric strain was included into the model (Sawada 2008). In the present study, the cyclic elasto-viscoplastic constitutive model presented by Sawada (2008) is extended for partially saturated soils using the skeleton stress and the suction effect in the constitutive model (Oka et al., 2006; Kimoto et al., 2007).

It is well known that strain localization, and in general plastic instability phenomena play important roles as precursors of the failure of geomaterials. Strain localization is the phenomenon by which plastic deformations localize into narrow bands of intense straining. The proper modeling of strain localization can be very significant in precautions against failure in many engineering problems. Strain localization of geomaterials has been widely studied numerically by using the mixture theory under quasi-static and dynamic loading conditions. Loret and Prévost (1991), Schrefler et al. (1995, 1996), and Ehlers and Volk (1998) numerically studied the localization problem of water-saturated geomaterials with the rate independent constitutive model. Under quasi-static deformations, Oka et al. (1994, 1995, 2000, and 2005) have studied the shear band development of water-saturated clays by using an elasto-viscoplastic constitutive model. They used the Biot's type two-phase mixture theory in the formulation to reduce the material instability problems. They found that strain localization is closely linked to material instability, and it can be effectively simulated through the finite element analysis using the elasto-viscoplastic model, for both normally consolidated and over consolidated water-saturated clays. Although many geotechnical problems such as landslide, the stability of embankments, retaining walls, and excavations are related to partially saturated soils, and despite the fact that the role of strain localization in deformation and progressive of failure in these geotechnical problems can be very significant, strain localization in partially saturated porous media has received less attention than fully saturated soils and single phase materials. In this study, the dynamic strain localization in saturated and partially saturated clay is numerically studied using the finite element method and the cyclic elasto-viscoplastic constitutive model.

Earth embankments have often experienced severe damage during past large earthquakes. Failure of an embankment can cause significant economic damage and loss of life. Although most of the damage was triggered by the occurrence of soil liquefaction beneath the embankments, some case histories demonstrated that earth embankments resting on non-liquefiable soft soils have also experienced extensive seismic failure. In this study, the different modes of failure affecting embankments as a consequence of earthquake shaking are presented and discussed. Furthermore, the seismic behavior of a partially saturated embankment on non-liquefiable soft clay is numerically studied.

1.2 Scope and Organization

The outline of the work presented in this doctoral thesis is briefly described in the followings.

Chapter 2, presents a cyclic elasto-viscoplastic model and its application to simulate the behavior of fully saturated and partially saturated soil specimens under cyclic triaxial loading conditions. In the constitutive model, the skeleton stress and suction are adopted as the basic stress variables. The collapse behavior, which occurs with a decrease in suction, is considered with the shrinkage of the overconsolidation boundary surface, the static yield function, and the viscoplastic potential surface.

Chapter 3, extends the finite element formulation suitable for large deformation dynamic analysis to the case of multiphase materials. Detailed derivations of the governing equations and the conservation laws of multiphase porous media are presented. Newmark's β method is adopted as a time integration algorithm to discretize the governing equations in time. The van Genuchten type of equation is, also, employed as a constitutive equation between the saturation and the suction. In addition, a new computer program entitled "COMVI3D-DY011" is introduced for the large deformation dynamic analysis of partially saturated elasto-viscoplastic soils.

Chapter 4, presents the numerical results of the dynamic strain localization analysis of saturated and partially saturated clay in the regime of finite deformation using the multiphase mixture theory and the cyclic elasto-viscoplastic constitutive model. In addition, mesh-size dependency is analyzed to provide stable and convergent solutions. Also, the effects of the initial suction, loading rate, and confining pressure on shear band development are studied and discussed.

Chapter 5, presents the potential failure modes affecting embankments as a consequence of earthquake shaking. Furthermore, the seismic behavior of a partially saturated embankment on non-liquefiable soft clay is numerically studied in two cases with different ground water levels.

Chapter 6, gives the conclusions of this dissertation and recommendations for future works.

Chapter 2

Cyclic Elasto-Viscoplastic Constitutive Model for Partially Saturated Soils

2.1 Introduction

It is well known that strain rate sensitivity is an important characteristic of both fully saturated and partially saturated soils. In particular, in clayey soil a unique stress-strain curve exists for each different loading rate. Extensive studies have, thus, been conducted over the years to describe this time-dependent behavior of soil under static loading conditions (e.g., Adachi and Oka, 1982; Dafalias, 1982; Katona, 1984; Matsui and Abe, 1985; Kaliakin and Dafalias, 1990; Kimoto and Oka, 2005; Kutter and Sathialingam, 1992; Yin and Graham, 1999). However, a few viscoplastic constitutive models are available for the analysis under dynamic loading conditions (e.g., Oka, 1992; Modaressi and Laloui, 1997; Oka et al., 2004; Maleki and Cambou, 2009).

Oka (1992) developed a cyclic elasto-viscoplastic constitutive model for clay based on nonlinear kinematic hardening rule (Chaboche and Rousselier, 1983). Later on, Oka et al. (2004) proposed a cyclic viscoelastic-viscoplastic model by incorporating the viscoelastic feature into the constitutive equations, in which the behavior of clay can be described not only in the range of middle to high level of strain, but also in the range of low level of strain. Despite the ability of these models to explain the deformation characteristics under cyclic loading conditions, the effect of structural degradation of clay particles was disregarded. Taking into account the structural degradation and microstructural changes, a cyclic elasto-viscoplastic model was developed based on the nonlinear kinematic hard-

ening rules for the changes in both the stress ratio and the mean effective stress (Hoizumi, 1996; Watanabe et al., 2007). In order to improve the prediction of the behavior during cyclic loading process, the nonlinear kinematic hardening rule for changes in viscoplastic volumetric strain was included into the model (Sawada, 2008).

For unsaturated soils many constitutive models have been proposed (e.g., Alonso et al., 1990; Wheeler and Sivakumar, 1995; Wheeler and Karube, 1995; Cui and Delage, 1996; Thomas and He, 1998; Sheng et al., 2003; Oka et al., 2008; Nuth and Laloui, 2008). Most of the models, however, are derived within the framework of rate-independent model, such as elasto-plastic models. From the experimental studies (Kim, 2004; Oka et al., 2010), the time-dependent property of unsaturated soils has been observed, which illustrates the necessity of constructing a cyclic elasto-viscoplastic model for predicting the mechanical behavior of partially saturated soils.

In the present study, the cyclic elasto-viscoplastic constitutive model improved by Sawada (2008) is extended for partially saturated soils using the skeleton stress and the suction effect in the constitutive model (Oka et al., 2006; Kimoto et al., 2007). The collapse behavior of unsaturated soil is macroscopic evidence of the structural instability of the soil skeleton, and it is totally independent of the stress variables adopted in the constitutive modeling (Oka, 1988; Jommi, 2000). In the model the collapse behavior is described by the shrinkage of the overconsolidation boundary surface, the static yield surface, and the viscoplastic surface due to the decrease in suction.

After presenting the constitutive model, the element test simulations are conducted by integration of the constitutive equations on fully saturated and partially saturated soil specimens. To validate the model the results are compared with the experimental data from the cyclic and the monotonic triaxial tests.

2.2 Skeleton Stress in Partially Saturated Soil

Terzaghi (1936) introduced the effective stress concept to describe the deformation behaviour of water saturated soil. This concept was based on results of experiments on the strength and the deformation of soil. Terzaghi's effective stress in one-dimensional form is defined as:

$$\sigma^{'} = \sigma - u_w \tag{2.1}$$

where $\sigma^{'}$ is the effective stress, σ is the total stress and u_w is the pore-water pressure.

In this equation u_w is negative when the water is in compression. Equation (2.1) is only effective for saturated soils with incompressible grains and a pore space completely filled with incompressible fluid.

Oka (1996) presented the validity and limits of the effective stress concept in Geomechanics describing that the behaviour of saturated soil depends on both the balance of forces and the compressibility of the constituents.

Many researches have been discussing the effective stress for unsaturated soil (e.g. Simons and Menzies, 1974; Jennings and Burland, 1962; Lade and Boer, 1997; Nuth and Laloui, 2008). Bishop (1960) proposed an effective stress equation for unsaturated soils as:

$$\sigma_{ij}^{'} = (\sigma_{ij} - u_a\delta_{ij}) + \chi\,(u_a - u_w)\,\delta_{ij} \tag{2.2}$$

where, $\sigma_{ij}^{'}$ is the effective stress tensor or the Bishop stress tensor, σ_{ij} is the total stress tensor, u_a and u_w are the pore-air pressure and the pore-water pressure, respectively, δ_{ij} is Kronecker's delta, and χ is a constitutive material parameter that ranges from zero for dry soil to 1.0 for saturated soil depending on the degree of saturation. The term $(\sigma_{ij} - u_a\delta_{ij})$ is called net stress, and the product $\chi\,(u_a - u_w)$ represents the interparticle effective stress due to capillary cohesion. The following considerations are mentioned about Equation (2.2):

1. The equation averages the stresses over a representative elementary volume containing all constituents: air, water and solid grains.

2. Bishop's effective stress tensor cannot be applied to explain the issues related to collapsible soil, such as the collapse behaviour, because suction $(u_a - u_w)$ and effective stress decrease during wetting (Jennings and Burland, 1962).

3. This expression does not consider the compressibility of the constituents because it relies solely on the balance force (Oka, 1996).

4. χ is implemented to scale down the influence of suction in the function of the volumetric ratios of the different fluid phases. But this parameter can be different for shear strength and volumetric deformation (Nuth and Laloui, 2008).

To reflect the collapse behavior of unsaturated soils, researchers (Bishop and Donald, 1961; Coleman, 1962; Matyas and Radhakrishna, 1968; Fredlund and Morgenstern, 1977)

have suggested the independent stress variable approach, where two stresses are proposed for both the soil particles and the fluids. According to their studies any pair of stress fields among the following three stress states, $(\sigma_{ij} - u_a\delta_{ij})$, $(\sigma_{ij} - u_w\delta_{ij})$, and $(u_a - u_w)\,\delta_{ij}$, can be applied as a suitable stress framework to describe the stress-strain-strength behavior of partially saturated soils. For instance, two stress variables, $(\sigma_{ij} - u_a\delta_{ij})$ and suction $(u_a - u_w)\,\delta_{ij}$, have been adopted to describe the mechanical behavior of unsaturated soil by some researchers (Fredlund and Morgenstern, 1977; Alonso et al., 1990; Wheeler and Sivakumar, 1995; Gens, 1995; Cui and Delage, 1996). The limitations of the independent stress variables approach are:

1. Net stress and suction could fail to provide straightforward transition between saturated and unsaturated states. That is, Terzaghi's effective stress cannot be recovered.

2. A double constitutive matrix is needed.

3. The adoption of net stress $\sigma_{ij} - u_a\delta_{ij}$ is valid for unsaturated soil only when the air pressure is thought to be constant. This is because the net stress is affected by the changes in air pressure and it is not an independent stress variable. However, drained conditions for water and air cannot always be attained in engineering problems. For example, the air pressure in river embankments or slopes increases during the seepage process or rainfall infiltration and may vary for soils during the soil compaction process.

Meanwhile, using the net stress and the suction as stress variables, it is very difficult to apply many constitutive models which have been developed for saturated soils, to unsaturated soils (Kohgo et al., 1993).

Recently, other generalized effective stress formulations have also been used to explain the collapse phenomenon (Bolzon et al., 1996; Khalili and Khabbaz, 1998; Loret and Khalili, 2000; Kohgo et al., 2001). Most of these models are defined by the generalized effective stress concept with the introduction of a new constitutive parameter for the effective stress. Recently, the terms "Effective stress" (Bolzon et al. 1996; Houlsby, 1997; Ehlers, 2004), "Average soil skeleton stress" (Jommi, 2000; Oka et al., 2006; Wheeler et al., 2003), "Generalized effective stress" (Laloui and Nuth, 2009), and "Skeleton stress" (Oka et al., 2008; 2010) have been used from a view point of the mixture theory; where the skeleton stress σ'_{ij} in Equation (2.3) is averaged over the total mixture volume. In

this formulation the fluid pressure contributions are linked to their respective volumetric fraction.

$$\sigma_{ij}^{'} = \sigma_{ij} + P^F \delta_{ij} \tag{2.3}$$

where P^F is the average pressure of the fluids surrounding the soil skeleton. In this equation P^F is positive when the fluids are in compression.

In the present model, the skeleton stress and suction are adopted as the basic stress variables. Suction is incorporated into the constitutive model to describe the collapse behavior of partially saturated soil. The skeleton stress is the same as the average soil skeleton stress by Jommi (2000) and the generalized effective stress by Laloui and Nuth (2009). Note that we use the "Skeleton stress" instead of "Average soil skeleton stress" to avoid confusing with the mean skeleton stress (Oka et al., 2010). The Skeleton stress is consistent with the theory of mixture for multiphase materials, and it will be derived in Section 3.4.

2.3 Elastic Strain Rate

The total strain rate tensor is assumed to be decomposable into two parts as

$$\dot{\varepsilon}_{ij} = \dot{\varepsilon}_{ij}^e + \dot{\varepsilon}_{ij}^{vp} \tag{2.4}$$

where $\dot{\varepsilon}_{ij}^e$ denotes the elastic strain rate tensor and $\dot{\varepsilon}_{ij}^{vp}$ is the viscoplastic strain rate tensor.

The elastic strain rate tensor $\dot{\varepsilon}_{ij}^e$ can be expressed as

$$\dot{\varepsilon}_{ij}^e = \dot{e}_{ij}^e + \frac{1}{3}\dot{\varepsilon}_v^e \delta_{ij} \tag{2.5}$$

where $\dot{e}_{ij}^e$ is the deviatoric elastic strain rate tensor given by

$$\dot{e}_{ij}^e = \frac{1}{2G}\dot{S}_{ij} \tag{2.6}$$

and $\dot{\varepsilon}_v^e$ is the volumetric elastic strain rate tensor given by

$$\dot{\varepsilon}_v^e = \dot{\varepsilon}_{11}^e + \dot{\varepsilon}_{22}^e + \dot{\varepsilon}_{33}^e \tag{2.7}$$

which can be obtained from the following relationship during the isotropic swelling process

$$\dot{\varepsilon}_v^e = \frac{\kappa}{1+e}\frac{\dot{\sigma}'_m}{\sigma'_m} \tag{2.8}$$

where κ is the swelling index, σ'_m is the mean skeleton stress, and e is the void ratio σ'_m denotes the mean skeleton stress given by

$$\sigma'_m = \frac{1}{3}\sigma'_{kk} = \frac{1}{3}(\sigma'_{11} + \sigma'_{22} + \sigma'_{33}) \tag{2.9}$$

In Equation (2.6), S_{ij} is the deviatoric stress tensor given by

$$S_{ij} = \sigma'_{ij} - \sigma'_m \delta_{ij} \tag{2.10}$$

and G is the elastic shear modulus. The degradation of elastic shear modulus G as a function of strain will be presented in the next section.

2.4 Strain Dependency of the Elastic Shear Modulus

The non-linearity of soil stiffness has been studied extensively on materials such as sands, clays, and gravel, and has been well summarized by Ishihara (1996). For cohesive soils, several empirical equations have been proposed by considering the dependency of the shear modulus on the effective confining stress (Kokusho et al., 1982). In the original configuration by Kimoto and Oka (2005), the change in the elastic shear modulus of the elasto-viscoplastic model is given by the square root function of the normalized mean skeleton stress as

$$G = G_0\sqrt{\frac{\sigma'_m}{\sigma'_{m0}}} \tag{2.11}$$

in which G_0 is the initial shear modulus. G_0 is definitely an important parameter in all kinds of dynamic response analyses. The initial shear modulus depends on the initial void ratio, and the initial confining stress. It can be expressed empirically as follows:

$$G_0 = Af(e_0)(\sigma'_{m0})^n \tag{2.12}$$

where A and n are the material parameters and $f(e_0)$ is the function of the initial void ratio e_0.

Equation (2.11) considers only the effect of the confining pressure, which can accurately approximate the variation in shear modulus at very small levels of strain. In regions with large levels of strain, however, as demonstrated by the experimental results, the strain dependency of the shear modulus should be considered as well. Various empirical formulations have been provided from the laboratory test results to express the strain dependency of the shear modulus (e.g., Hardin and Drnevich, 1972; Wang and Kuwano, 1999). Ogisako et al. (2007) have introduced a normalized shear modulus reduction function based on the viscoplastic shear strain in soft clay specimens and have proposed a hyperbolic equation for that expression, namely,

$$G = G_0(e_0)\frac{1}{(1+\alpha(\gamma^{vp})^r)} \tag{2.13}$$

where α is the strain-dependent parameter, r is the experimental constant, and γ^{vp} is the accumulated viscoplastic shear strain given by an accumulation of the viscoplastic deviatoric strain rate as $\gamma^{vp} = \int \sqrt{de_{ij}^{vp} de_{ij}^{vp}}$.

In this study, based on the experimental results, $r = 0.4$ is chosen. Therefore, the final formulation for the variation in shear modulus can be incorporated as

$$G = G_0(e_0)\frac{1}{\left(1+\alpha(\gamma^{vp})^{0.4}\right)}\sqrt{\frac{\sigma'_m}{\sigma'_{m0}}} \tag{2.14}$$

2.5 Overconsolidation Boundary Surface

In the stress space an overconsolidation boundary surface f_b is defined as the boundary between the normally consolidated (NC) region and the overconsolidated (OC) region by

$$f_b = \bar{\eta}^*_{(0)} + M^*_m \ln\left(\sigma'_m/\sigma'_{mb}\right) = 0 \tag{2.15}$$

where $f_b < 0$ indicates the overconsolidated region and $f_b \geq 0$ shows the normally consolidated region. $\bar{\eta}^*_{(0)}$ is the relative stress ratio defined by

$$\bar{\eta}^*_{(0)} = \left\{\left(\eta^*_{ij} - \eta^*_{ij(0)}\right)\left(\eta^*_{ij} - \eta^*_{ij(0)}\right)\right\}^{\frac{1}{2}} \tag{2.16}$$

in which subscript (0) denotes the initial state before deformation and η_{ij}^* is the stress ratio tensor. σ_{mb}' is the hardening parameter, which controls the size of the OC boundary surface. M_m^* is the value of $\eta^* = \sqrt{\eta_{ij}^* \eta_{ij}^*}$ when the volumetric strain increment changes from compression to swelling. The stress ratio at triaxial compression state M_{mc}^* and the stress ratio at the extension state M_{me}^* can be obtained by the internal frictional angle ϕ as

$$M_{mc}^* = \sqrt{\frac{2}{3}} \frac{6\sin\phi}{3-\sin\phi} \tag{2.17}$$

$$M_{me}^* = \sqrt{\frac{2}{3}} \frac{6\sin\phi}{3+\sin\phi} \tag{2.18}$$

For sands, due to the material anisotropy, method of sample preparation, degree of compaction, aging, etc., the initial value of $\sigma_{mb}^{'}$, $\sigma_{mbi}^{'}$, is not always equal to the initial mean skeleton stress $\sigma_{m0}^{'}$. Therefore, it is appropriate to define the quasi-overconsolidation ratio as

$$OCR^* = \frac{\sigma_{mbi}'}{\sigma_{m0}'} \tag{2.19}$$

The overconsolidation boundary surface described in Equation (2.15) can be written in the triaxial stress state of $(\sigma_{11}', \sigma_{22}', \sigma_{33}')$ as follows

$$f_b = \left| \left(\frac{q}{\sigma_m'} \right) - \left(\frac{q}{\sigma_m'} \right)_{(0)} \right| + M_m ln \frac{\sigma_m'}{\sigma_{mb}'} = 0 \tag{2.20}$$

in which q is the deviator stress ($q = \sigma_{11}' - \sigma_{33}'$), $\sigma_{22}' = \sigma_{33}'$, and $M_m = \sqrt{\frac{3}{2}} M_m^*$.

In order to describe the structure degradation on natural clay, strain-softening with viscoplastic strain is introduced into the hardening parameter in addition to strain hardening with the viscoplastic volumetric strain. Meanwhile, to describe the suction effect on the unsaturated soil, suction is incorporated into the value of $\sigma_{mb}^{'}$ as

$$\sigma_{mb}^{'} = \sigma_{mau}^{'} \exp\left(\frac{1+e_0}{\lambda-\kappa} \varepsilon_{kk}^{vp}\right) \tag{2.21}$$

$$\sigma_{mau}^{'} = \sigma_{ma}^{'} \left[1 + S_I \exp\left\{ -s_d \left(\frac{P_i^C}{P^C} - 1 \right) \right\} \right] \tag{2.22}$$

where ε_{kk}^{vp} is the viscoplastic volumetric strain, λ and κ are the compression and the swelling indexes, respectively, and e_0 is the initial void ratio. $\sigma_{ma}^{'}$ is a strain-softening parameter used to describe the structure degradation effect, which is assumed to decrease with an increasing in viscoplastic strain, namely,

$$\sigma_{ma}^{'} = \sigma_{maf}^{'} + (\sigma_{mai}^{'} - \sigma_{maf}^{'}) \exp(-\beta z) \tag{2.23}$$

where z is the accumulation of the second invariant of the viscoplastic strain rate given by

$$z = \int_0^t \dot{z} dt, \qquad \dot{z} = \sqrt{\dot{\varepsilon}_{ij}^{vp} \dot{\varepsilon}_{ij}^{vp}} \tag{2.24}$$

In Equation (2.23), $\sigma_{mai}^{'}$ and $\sigma_{maf}^{'}$ are the initial and the final values for $\sigma_{ma}^{'}$, respectively, β is a material parameter which controls the rate of structural changes, and z is the accumulation of the second invariant of viscoplastic strain rate $\dot{\varepsilon}_{ij}^{vp}$. Since the viscoplastic strain is equal to zero at the initial state, we can obtain the consolidation yield stress $\sigma_{mbi}^{'}$ equal to $\sigma_{mai}^{'}(1 + S_I)$.

In Equation (2.22), S_I is the strength ratio of unsaturated soils when the value of suction P^C equals to P_i^C, and s_d controls the decreasing ratio of strength with decreasing suction. The term P_i^C is set to be the initial value of suction. At initial state when $P^C = P_i^C$, the strength ratio of the unsaturated soil to the saturated soil is $1 + S_I$ and decreases with a decline in suction. The change of hardening parameter with change in suction and the effect of parameter s_d is shown in Figure 2.1.

2.6 Static Yield Function

Static yield function is obtained by considering the nonlinear kinematic hardening rule for the changes in the stress ratio, in the mean effective stress, and in the viscoplastic volumetric strain, as

$$f_y = \bar{\eta}_\chi^* + \tilde{M}^* \left(\ln \frac{\sigma_{mk}^{'}}{\sigma_{my}^{'(s)}} + \left| \ln \frac{\sigma_m^{'}}{\sigma_{mk}^{'}} - y_{m1}^* \right| \right) = 0 \tag{2.25}$$

$$\bar{\eta}_\chi^* = \left\{ (\eta_{ij}^* - \chi_{ij}^*) (\eta_{ij}^* - \chi_{ij}^*) \right\}^{\frac{1}{2}} \tag{2.26}$$

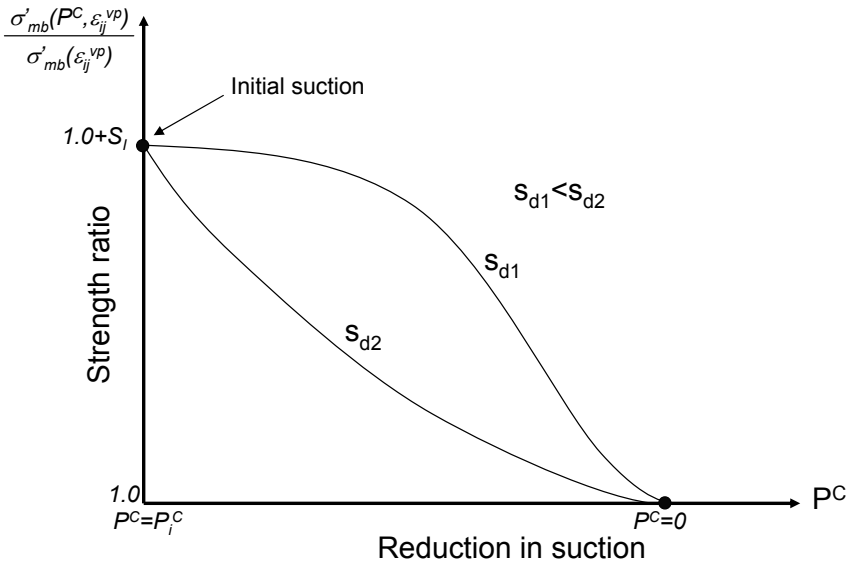

Figure 2.1 Strength degradation due to the reduction in suction

in which $\sigma^{'}_{mk}$ is the unit value of the mean effective stress, y^{*}_{m1} is the scalar kinematic hardening parameter, and $\sigma^{'(s)}_{my}$ denotes the static hardening parameter. χ^{*}_{ij} is so-called back stress parameter, which has the same dimensions as stress ratio η^{*}_{ij}. Incorporating the strain softening for the structural degradation, the hardening rule of $\sigma^{'(s)}_{my}$ can be expressed as

$$\sigma^{'(s)}_{my} = \frac{\sigma^{'}_{mau}}{\sigma^{'}_{mai}} \sigma^{'(s)}_{myi} \tag{2.27}$$

Note that Equation (2.27) is different from the one presented by Sawada (2008). In Sawada's formulation the hardening rule of $\sigma^{'(s)}_{my}$ includes the effect of volumetric strain twice (Mirjalili, 2010). Hence, it has been modified in the current formulation by replacing $\sigma^{'}_{mb}$ with $\sigma^{'}_{mau}$.

2.7 Viscoplastic Potential Function

In the same manner as for the static yield function, viscoplastic potential function f_p is given by

$$f_p = \bar{\eta}^{*}_{\chi} + \tilde{M}^{*} \left(\ln \frac{\sigma'_{mk}}{\sigma'_{mp}} + \left| \ln \frac{\sigma'_{m}}{\sigma'_{mk}} - y^{*}_{m1} \right| \right) = 0 \tag{2.28}$$

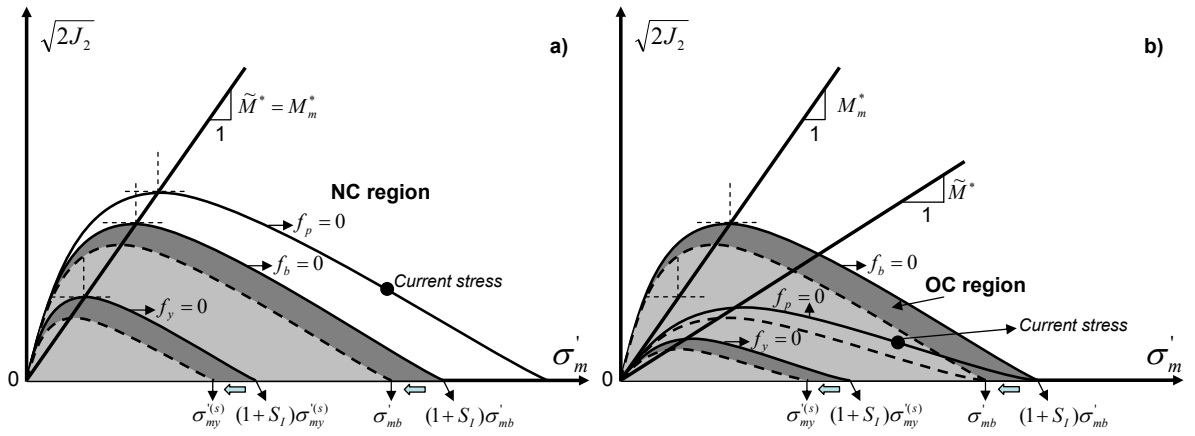

Figure 2.2 Shrinkage of the OC boundary surface, static yield function and potential function: a) In the NC region, b) In the OC region

The dilatancy coefficient $\tilde{M}^*$ is defined separately for the normally consolidated region (NC) and the overconsolidated region (OC) as

$$\tilde{M}^* = \begin{cases} M_m^* & \text{:NC region} \\ (\dfrac{\sigma_m^*}{\sigma_{mc}'})M_m^* & \text{:OC region} \end{cases} \tag{2.29}$$

where σ_{mc}' is the mean effective stress at the intersection of the overconsolidation boundary surface and σ_m' axis, which is defined by

$$\sigma_{mc}' = \sigma_{mb}' \exp\left(\frac{\sqrt{\eta_{ij(0)}^* \eta_{ij(0)}^*}}{M_m^*}\right) \tag{2.30}$$

In addition, σ_m^* denotes the mean effective stress at the intersection of the surface, which has the same shape as f_b, and is given by

$$\sigma_m^* = \sigma_m' \exp\left(\frac{\bar{\eta}_\chi^*}{M_m^*}\right) \tag{2.31}$$

The effect of the decrease in the suction on the shrinkage of the overconsolidation boundary surface, f_b, the static yield function, f_y, and the viscoplastic potential function, f_p, for $\eta_{ij(0)}^* = 0$, are illustrated schematically in the $\sigma_m' - \sqrt{2J_2}$ space, Figure 2.2. It can be seen that σ_{mb}' and $\sigma_{my}^{'(s)}$ decrease with decreasing suction owing to wetting. The increments in viscoplastic strain for the overstress type model depend on the difference between the current stress state and the static yield stress state, therefore, the shrinkage of f_y due to the wetting yields in the viscoplastic strain increments.

2.8 Kinematic Hardening Rule

The evolution equation for the nonlinear kinematic hardening parameter χ_{ij}^* is given by

$$d\chi_{ij}^* = B^* \left(A^* de_{ij}^{vp} - \chi_{ij}^* d\gamma^{vp} \right) \tag{2.32}$$

where A^* and B^* are material parameters, de_{ij}^{vp} is the viscoplastic deviatoric strain increment tensor, and $d\gamma^{vp} = \sqrt{de_{ij}^{vp} de_{ij}^{vp}}$ is the viscoplastic shear strain increment tensor. A^* is related to the stress ratio at failure, namely, $A^* = M_f^*$, and B^* is proposed to be dependent on the viscoplastic shear strain as

$$B^* = (B_{\max}^* - B_1^*) \exp\left(-C_f \gamma_{(n)}^{vp*}\right) + B_1^* \tag{2.33}$$

in which B_1^* is the lower boundary of B^*, C_f is the parameter controlling the amount of reduction, $\gamma_{(n)}^{vp*}$ is the accumulated value of the viscoplastic shear strain between two sequential stress reversal points in the previous cycle. $B_{\max}^*$ is the maximum value of parameter B^*, which was proposed by Oka et al (1999) as

$$B_{\max}^* = \begin{cases} B_0^* & : \text{Before reaching failure line} \\ \dfrac{B_0^*}{1 + \dfrac{\gamma_{(n)\max}^{vp*}}{\gamma_{(n)r}^{vp*}}} & : \text{After reaching failure line} \end{cases} \tag{2.34}$$

where B_0^* is the initial value of B^* , $\gamma_{(n)\max}^{vp*}$ is the maximum value of $\gamma_{(n)}^{vp*}$ in past cycles, and $\gamma_{(n)r}^{vp*}$ is the viscoplastic reference strain. In order to improve the predicted results under cyclic loading conditions, the scalar nonlinear kinematic hardening parameter y_{m1}^* is introduced as

$$dy_{m1}^* = B_2^* \left(A_2^* d\varepsilon_v^{vp} - y_{m1}^* \left| d\varepsilon_v^{vp} \right| \right) \tag{2.35}$$

where A_2^* and B_2^* are material parameters, and $d\varepsilon_v^{vp}$ is the increment of the viscoplastic volumetric strain. The values of A_2^* and B_2^* are determined by data-adjusting method from the laboratory test data. The relation between the scalar nonlinear kinematic hardening y_{m1}^* and the viscoplastic volumetric strain $d\varepsilon_v^{vp}$ is shown in Figure 2.3.

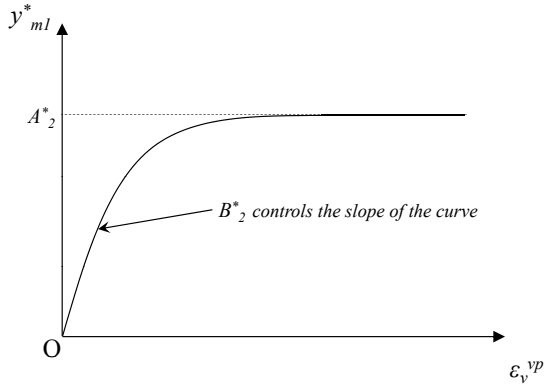

Figure 2.3 Scalar nonlinear kinematic hardening function y^*_{m1}

2.9 Viscoplastic Flow Rule

Based on the overstress type of viscoplastic theory first adopted by Perzyna (1963), viscoplastic strain rate tensor $\dot{\varepsilon}^{vp}_{ij}$ is defined as

$$\dot{\varepsilon}^{vp}_{ij} = C_{ijkl} \left\langle \Phi \left(f_y \right) \right\rangle \frac{\partial f_p}{\partial \sigma'_{kl}} \tag{2.36}$$

$$\left\langle \Phi \left(f_y \right) \right\rangle = \begin{cases} \Phi(f_y) & : \ f_y > 0 \\ 0 & : \ f_y \leq 0 \end{cases} \tag{2.37}$$

$$C_{ijkl} = a\delta_{ij}\delta_{kl} + b\left(\delta_{ik}\delta_{jl} + \delta_{il}\delta_{jk}\right) \tag{2.38}$$

where $\langle\rangle$ are Macaulay's brackets, $\Phi\left(f_y\right)$ is the rate-sensitive material function, and C_{ijkl} is a fourth order isotropic tensor. a and b in Equation (2.38) are material constants. The material function $\Phi\left(f_y\right)$ is determined as

$$\Phi\left(f_y\right) = \sigma'_m \exp\left\{ m' \left(\bar{\eta}^*_\chi + \tilde{M}^* \left(\ln \frac{\sigma'_{mk}}{\sigma'_{mau}} + \left| \ln \frac{\sigma'_m}{\sigma'_{mk}} - y^*_{m1} \right| \right) \right) \right\} \tag{2.39}$$

in which m' is the viscoplastic parameter. Finally, by combining Equations (2.36) to (2.39) viscoplastic deviatoric strain rate $\dot{e}^{vp}_{ij}$ and viscoplastic volumetric strain rate $\dot{\varepsilon}^{vp}_{ij}$ can be expressed as

$$\dot{e}^{vp}_{ij} = C_1 \exp\left\{ m' \left(\bar{\eta}^*_\chi + \tilde{M}^* \left(\ln \frac{\sigma'_{mk}}{\sigma'_{mau}} + \left| \ln \frac{\sigma'_m}{\sigma'_{mk}} - y^*_{m1} \right| \right) \right) \right\} \frac{\eta^*_{ij} - \chi^*_{ij}}{\bar{\eta}^*_\chi} \tag{2.40}$$

$$\dot{\varepsilon}_{kk}^{vp} = C_2 \exp\left\{ m' \left(\bar{\eta}_\chi^* + \tilde{M}^* \left(\ln \frac{\sigma'_{mk}}{\sigma'_{mau}} + \left| \ln \frac{\sigma'_m}{\sigma'_{mk}} - y_{m1}^* \right| \right) \right) \right\} \left\{ \tilde{M}^* \frac{\ln \dfrac{\sigma'_m}{\sigma'_{mk}} - y_{m1}^*}{\left| \ln \dfrac{\sigma'_m}{\sigma'_{mk}} - y_{m1}^* \right|} - \frac{\eta_{mn}^* \left(\eta_{mn}^* - \chi_{mn}^* \right)}{\bar{\eta}_\chi^*} \right\} \tag{2.41}$$

where $C_1 = 2b$ and $C_2 = 3a + 2b$ are the viscoplastic parameters for the deviatoric and the volumetric strain components, respectively.

2.10 Determination of Material Parameters

In the proposed constitutive model, some parameters are directly determined from in-situ or laboratory tests, while others are estimated by empirical equations or calibrated by a data adjusting method through an element simulation. The parameters can be set by using the following methods:

- The compression index λ and swelling index κ can be determined by the slope of the e-ln$p$ relation during the isotropic consolidation and swelling tests, respectively.

- The initial void ratio can be calculated with the specific gravity of the soil particles, the water contents, and the bulk density based on the results of tests conducted on undisturbed samples.

- The overconsolidation ratio can usually be estimated from the consolidation yield stress and the current effective overburden pressure. For sandy soils, the consolidation yield stress of which is not clear under a normal confining pressure, quasi-overconsolidation ratio should be calculated from the volume change characteristics, including the Dilatancy of sand.

- Elastic shear modulus can be calculated by the initial slope of the undrained triaxial compression tests, namely,

$$G_0 = \frac{1}{3} \frac{\Delta q}{\Delta \varepsilon_{11}} \tag{2.42}$$

where Δq is the increment in deviator stress and $\Delta \varepsilon_{11}$ is the increment in axial strain.

- The stress ratios at the compression and the extension state are calculated from the internal friction angle using Equations (2.17) and (2.18).

- Viscoplastic parameter m' is determined from undrained triaxial compression tests conducted at different strain rates. Adachi and Oka (1982) noted that viscoplastic pa-

rameter m' is estimated from the slope of the relation between the stress ratio and the logarithm of the strain rate. By having m', the other viscoplastic parameters, C_1 and C_2, are obtained from Equations (2.40) and (2.41) in the monotonic triaxial stress state.

- Structural parameter $\sigma^{'}_{maf}$ can be obtained by the deviator stress at the residual stress state.

The other parameters can be determined by an element simulation which tries to reproduce the results of mechanical laboratory tests under the same boundary and initial conditions as the tests. An element simulation results are approximate solutions of the constitutive equations, using the Runge-Kutta method, under the tiraxial stress state. The values for the material parameters are selected in order to provide a good description of the stress-strain relations and the stress paths under cyclic loading conditions.

2.11 Triaxial Test Simulation for Nakanoshima Clay

The ability of a nonlinear computational analysis to provide realistic simulations of the behavior of soil depends on the capability of the constitutive model used to describe the mechanical response of the soil skeleton. In this section, numerical simulations of cyclic and monotonic undrained triaxial tests for fully saturated Nakanoshima clay are conducted to investigate the performance of the proposed cyclic elasto-viscoplastic model.

Following the procedures explained in previous chapter, the material parameters of Nakanoshima clay are determined and listed in Table 2.1. The soil samples, which are used for the cyclic triaxial test and the monotonic test, appear to be slightly different. Therefore, different sets of parameters are obtained for each sample. Comparing the initial void ratio of the samples, the cyclic sample has smaller void ratio, which emphasizes the stiffer behavior compared with the sample for monotonic test. Accordingly, the values of the hardening parameter and the structural parameters have been determined in a manner that more softening behavior can be reproduced for the monotonic sample.

The results of the simulation under monotonic triaxial conditions are illustrated in Figure 2.4, in which the symbols show the experimental values and the solid lines represent the simulated results. The simulated results for stress-strain relation and stress path provide good agreement with the experimental data. Efforts are made for adjusting the parameters such as the structural parameters, the hardening parameters, and the strain-dependent parameter, so that the best possible agreement can be achieved between the simulation and the experimental results.

The results of the stress-strain relation and stress path for the simulation and for

Table 2.1 Material parameters of Nakanoshima clay*

		Cyclic test	Monotonic test
Compression index	λ	0.2173	0.2173
Swelling index	κ	0.0344	0.0344
Initial shear elastic modulus (kPa)	G_0	22670	22670
Initial void ratio	e_0	1.373	1.573
Initial mean skeleton stress (kPa)	$\sigma^{'}_{m0}$	200.0	200.0
Softening parameter (kPa)	$\sigma^{'}_{mai}$	200.0	200.0
Stress ratio at failure in compression	M^*_{mc}	1.143	1.143
Stress ratio at failure in extension	M^*_{me}	1.061	1.061
Viscoplastic parameter	$m^{'}$	22.7	22.7
Viscoplastic parameter (1/s)	C_1	1.0×10^{-5}	1.0×10^{-5}
Viscoplastic parameter (1/s)	C_2	3.3×10^{-6}	3.3×10^{-6}
Structural parameter	$n = \sigma^{'}_{maf}/\sigma^{'}_{mai}$	0.325	0.325
Structural parameter	β	3.7	5.7
Hardening parameter	B^*_0	105	105
Hardening parameter	B^*_1	1.0	1.0
Hardening parameter	C_f	5	75
Reference value of viscoplastic strain (%)	$\gamma^{vp*}_{(n)r}$	3.5	3.5
Strain-dependent modulus parameter	α	10	1
Hardening parameter	A^*_2	5.1	5.1
Hardening parameter	B^*_2	2.6	2.6

* Samples are different in two tests.

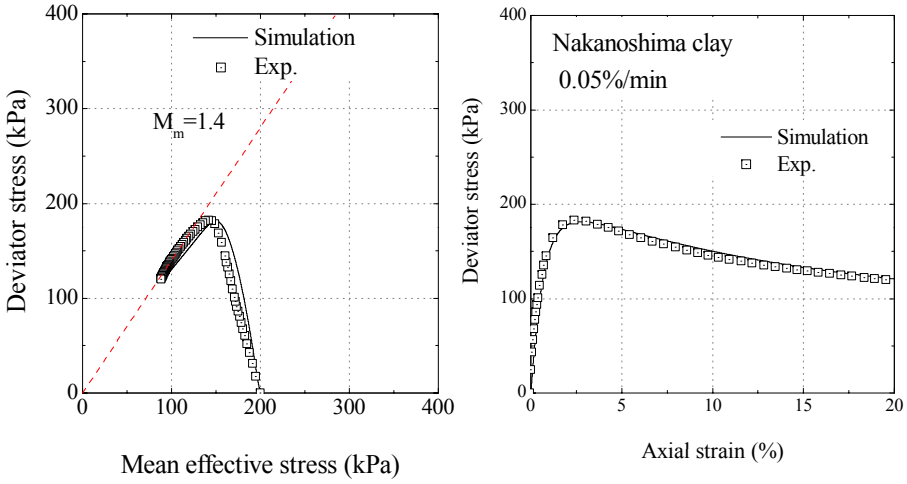

Figure 2.4 Stress-strain relations and stress paths for Nakanoshima clay under the monotonic undrained triaxial conditions

the experimental test under cyclic triaxial conditions are presented in Figure 2.5. The cyclic test was accomplished with the cyclic stress ratio ($CSR = q/2\sigma'_{m0}$) equal to 0.30. The stress-strain relation of the simulated results demonstrate a good tendency with the experimental data, in terms of the strain levels in both compression and extension sides and the number of cycles. The simulated result of stress path, on the other hand, does not show such good agreement with the experimental data. This might be attributed to the different mechanism of measurement for the pore water pressure during the experiments, which is based on the average values of the whole specimen, while in the simulation the results of the one-point response is considered.

2.12 Triaxial Test Simulation for the Partially Saturated Sandy Soil

The simulation of the cyclic suction-controlled triaxial test was conducted to obtain the material parameters of the partially saturated sandy soil by using the cyclic elasto-viscoplastic constitutive model. The parameters are listed in Table 2.2.

Efforts were made to determine the parameters so that the simulated results provide the closest trend to the experimental data under three different strain rates, namely, $0.01\%/min$, $0.1\%/min$, $0.75\%/min$ with the cyclic stress ratio (CSR) equal to 0.2 and the number of cycles equal to 100. Figures 2.6 to 2.8 indicate the deviator stress-axial strain and volumetric strain-axial strain relations of the predicted results and the corresponding

Table 2.2 Material parameters of the partially saturated sandy soil*

Compression index	λ	0.061
Swelling index	κ	0.004
Initial shear elastic modulus (kPa)	G_0	20000
Initial void ratio	e_0	0.65
Initial mean skeleton stress (kPa)	$\sigma^{'}_{m0}$	127.0
Softening parameter (kPa)	$\sigma^{'}_{mai}$	150.0
Stress ratio at failure in compression	M^*_{mc}	1.18
Stress ratio at failure in extension	M^*_{me}	0.799
Viscoplastic parameter	$m^{'}$	40.0
Viscoplastic parameter (1/s)	C_1	1.0×10^{-5}
Viscoplastic parameter (1/s)	C_2	1.0×10^{-5}
Structural parameter	$n = \sigma^{'}_{maf}/\sigma^{'}_{mai}$	0.53
Structural parameter	β	5.0
Hardening parameter	B^*_0	200
Hardening parameter	B^*_1	15.0
Hardening parameter	C_f	5.0
Strain-dependent modulus parameter	α	1.0
Hardening parameter	A^*_2	9.0
Hardening parameter	B^*_2	3.6
Initial suction (kPa)	P^C_i	50.0
Suction parameter	S_I	0.2
Suction parameter	s_d	0.6

*Used for the construction of the Yodo river embankment

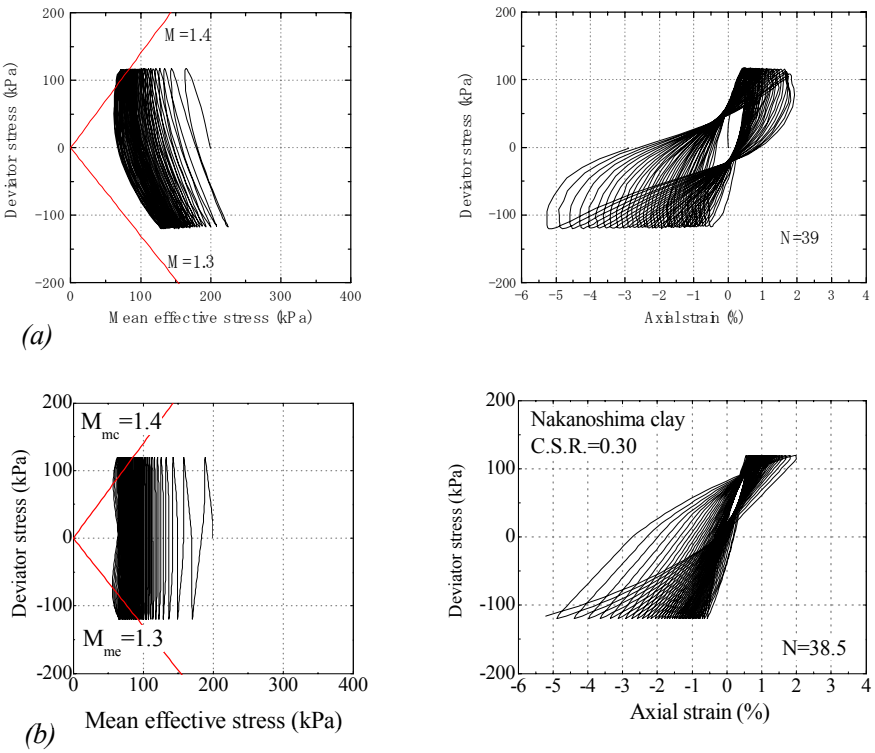

Figure 2.5 Stress-strain relations and stress paths for Nakanoshima clay under the cyclic undrained triaxial conditions: (a) experimental results, (b) simulated results

experimental results. Applying smaller strain rate, higher axial strain level is expected to be observed. However, in the experimental results it is seen that the maximum level of axial strain in the case of $\dot{\varepsilon} = 0.1\%/min$ is higher than the one in the case of $\dot{\varepsilon} = 0.01\%/min$; this might be due to experimental errors in the performance of the test. In the cases of $\dot{\varepsilon} = 0.01\%/min$ and $\dot{\varepsilon} = 0.75\%/min$, the simulation results demonstrate a good tendency with the experimental results.

2.13 Summary

The cyclic Elasto-viscoplastic constitutive model presented by Sawada (2008) was extended in this study for partially saturated soils using the skeleton stress and suction effect in the constitutive model. The performance of the model was verified, first through the modeling of fully saturated soft clay specimens under undrained cyclic and monotonic triaxial conditions, and then through the simulation of partially saturated sand specimens under cyclic suction-controlled triaxial conditions.

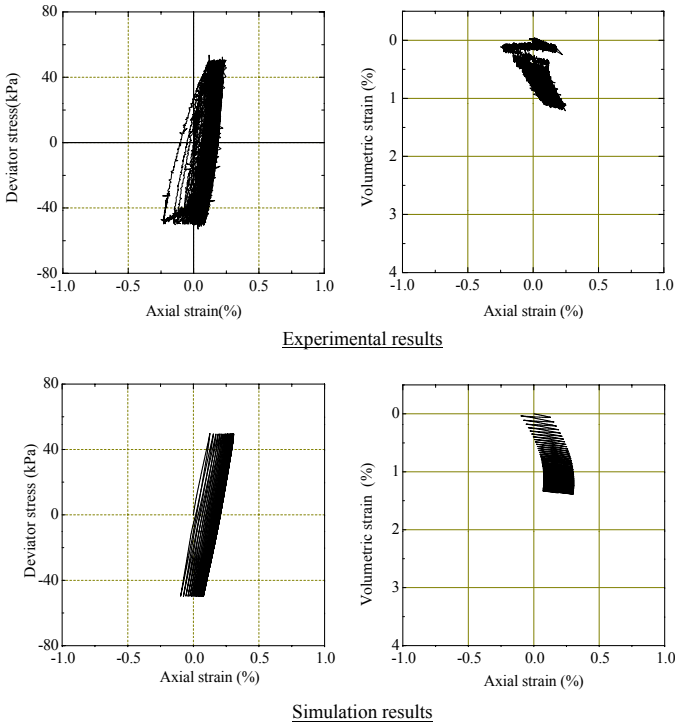

Figure 2.6 Experimental and simulated results for the unsaturated sandy soil under cyclic suction-controlled triaxial conditions (strain rate = $0.01\%/min$, $P^C = 50$kPa)

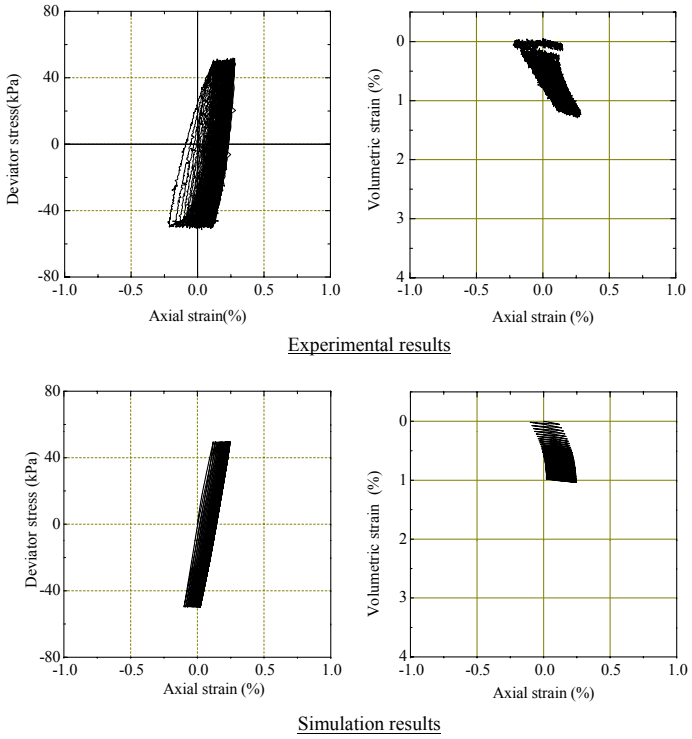

Figure 2.7 Experimental and simulated results for the unsaturated sandy soil under cyclic suction-controlled triaxial conditions (strain rate = $0.1\%/min$, $P^C = 50$kPa)

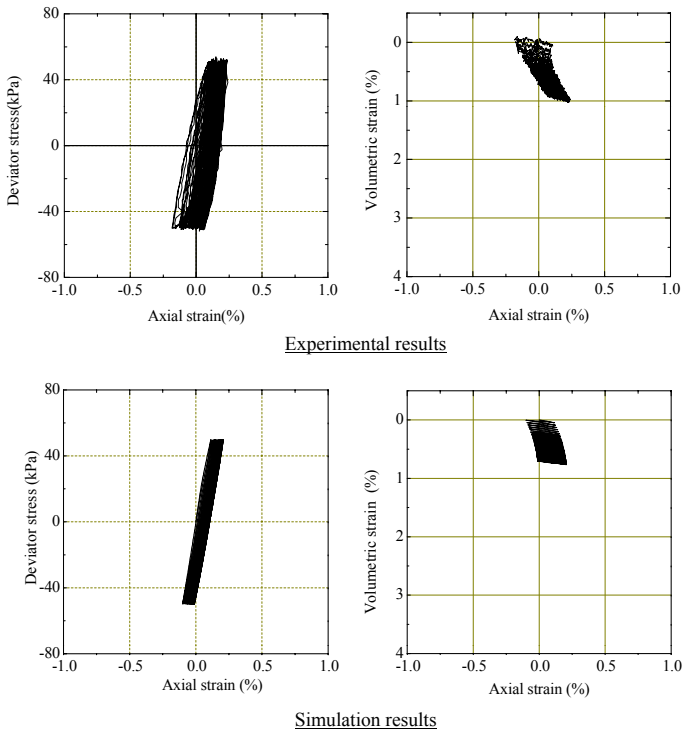

Figure 2.8 Experimental and simulated results for the unsaturated sandy soil under cyclic suction-controlled triaxial conditions (strain rate = $0.75\%/min$, $P^C = 50$kPa)

Chapter 3

Finite Element Formulation for Large Deformation Dynamic Analysis of Multiphase Porous Media

3.1 Introduction

It has been recognized that the behavior of partially saturated soils plays an important role in Geomechanics. Many geotechnical problems, i.e., natural slopes, embankments, artificial structures, expansive soils, soil containing methane hydrates, etc., are related to partially saturated soils.

Partially saturated soils fall into the field of multi-phase materials, which are defined as materials with an internal structure. They are composed of soil particles, water and air. The behavior of multi-phase materials can be described by the macroscopic continuum mechanical approach through the use of the theory of porous media (e.g., Atkin and Craine, 1976; Bowen, 1976; Coussy, 2004; Schrefler and Gawin, 1996; de Boer, 1998; Ehlers, 2003). The theory is considered to be a generalization of Biot's two-phase mixture theory for saturated soils (Biot, 1941; 1962).

A finite element model based on two-phase mixture theory was presented by Oka et al. (2001) for the analysis of fully saturated earth structures in the regime of finite deformation with an updated Lagrangian description. In this research, the finite element formulation is extended for partially saturated soils based on the conservations laws gov-

erning multiphase porous media. In this study,

1. The formulation is based on the finite deformation theory.
2. The derivation of the conservation laws is based on the theory of porous media which is the extension of Biot theory for a multiphase mixture.
3. For the spatial discretization, the finite element method is used.
4. The time discretization is carried out using Newmark's β method.
5. The van Genuchten type of equation is employed as a constitutive equation between the saturation and the suction (van Genuchten, 1980)

3.2 Volume Fraction

The material to be modeled is composed of three phases, namely, solid (S), liquid (W), and gas (G), which are continuously distributed throughout space. Each constituent has a volume V^α.

The total volume V is obtained from the sum of the partial volumes of the constituents, namely,

$$V = \sum_\alpha V^\alpha \qquad (\alpha = S, W, G) \tag{3.1}$$

The volume of void V^V, which is composed of water and gas, is given as follows:

$$V^V = \sum_\beta V^\beta \qquad (\beta = W, G) \tag{3.2}$$

Volume fraction n^α is defined as the local ratio of the volume element with respect to the total volume, namely,

$$n^\alpha = \frac{V^\alpha}{V} \qquad \sum_\alpha n^\alpha = 1 \qquad (\alpha = S, W, G) \tag{3.3}$$

The volume fraction of the void, n, is written as

$$n = \sum_\beta n^\beta = \frac{V^V}{V} = \frac{V - V^S}{V} = 1 - n^S \qquad (\beta = W, G) \tag{3.4}$$

In addition, water saturation is required in the model,

$$s = \frac{V^W}{V^W + V^G} = \frac{V^W}{V^V} \tag{3.5}$$

Accordingly, the volume fraction can be given by

$$n^W = sn \qquad n^G = (1-s)n \tag{3.6}$$

3.3 Partial Mass Density

The partial mass density ρ^α and material (realistic or effective) density ρ_α are defined , respectively, as

$$\rho^\alpha = \frac{M^\alpha}{V} \quad \text{and} \quad \rho_\alpha = \frac{M^\alpha}{V^\alpha} \qquad (\alpha = S, W, G) \tag{3.7}$$

where M^α is the mass of each constituent. The density of the mixture can be expressed as

$$\rho = \sum_\alpha \rho^\alpha = \sum_\alpha \rho_\alpha n^\alpha \tag{3.8}$$

3.4 Skeleton Stress and Partial Stress Tensors

In the theory of porous media, the concept of the effective stress tensor is related to the deformation of the soil skeleton and plays and important role. The effective stress tensor has been defined for water-saturated soil (Terzaghi, 1943). In the case of unsaturated soils, however, the concept needs to be redefined in order to consider compressible materials. In the present study, skeleton stress tensor T'_{ij} is defined and then used for the stress variable in the constitutive relation for the soil skeleton (Jommi, 2000; Kimoto et al. 2007; Laloui and Nuth, 2009). Jommi calls it the average skeleton stress. Laloui and Nuth calls it generalised effective stress. The skeleton stress tensor is equivalent to the Bishop's stress tensor when degree of saturation s is taken as χ. Total stress tensor T_{ij} is obtained from the sum of the partial stress values, T^α_{ij}, namely,

$$\sum_\alpha T^\alpha_{ij} = T_{ij} \qquad (\alpha = S, W, G) \tag{3.9}$$

in which T^α_{ij} represents the stress acting on each phase. It is assumed as the Cauchy stress tensor.

The partial stresses for the fluid phases can be expressed as:

$$T_{ij}^{W} = -n^{W} P^{W} \delta_{ij} \tag{3.10}$$

$$T_{ij}^{G} = -n^{G} P^{G} \delta_{ij} \tag{3.11}$$

where P^W and P^G are the pore water pressure, and the pore gas pressure, respectively. Note that the sign convention used in this thesis conforms to the continuum mechanics convention: Tension stress is considered positive. For pore pressures, P^α ($\alpha = W, G$) is positive when the fluid α is in compression ($P^\alpha = -u_\alpha$).

The partial stress tensor for the solid phase can be expressed by the analogy with the water-saturated one as:

$$T_{ij}^{S} = T_{ij}^{'} - n^{S} P^{F} \delta_{ij} \tag{3.12}$$

where P^F is the average pressure of the fluids surrounding the soil skeleton obtained by the well-known Dalton's law via

$$P^{F} = sP^{W} + (1 - s)P^{G} \tag{3.13}$$

in which s is the degree of saturation.

These partial stress values make up the total stress tensor of the mixture, T_{ij}, as

$$T_{ij} = \sum_{\alpha} T_{ij}^{\alpha} = T_{ij}^{'} - n^{S} P^{F} \delta_{ij} - n^{W} P^{W} \delta_{ij} - n^{G} P^{G} \delta_{ij} = T_{ij}^{'} - P^{F} \delta_{ij} \tag{3.14}$$

$T_{ij}^{'}$ is called the skeleton stress in the present study. It is used as the stress variable in the constitutive relation for the soil skeleton:

$$T_{ij}^{'} = T_{ij} + P^{F} \delta_{ij} \tag{3.15}$$

3.5 Hydraulic Properties of Unsaturated Soils

3.5.1 Soil-Water Characteristic Curve

The soil-water characteristic curve (SWCC) for soil is defined as the relationship between the volumetric water content or degree of saturation and suction of the soil. The SWCC can be described as a measure of the water-holding capacity (i.e., the storage capacity)

of the soil as the water content changes when it is subjected to various levels of suction. In the model, the following type of equation for the SWCC is adopted (van Genuchten, 1980):

$$s_{re} = \left\{1 + (\alpha P^C)^{n'}\right\}^{-m} \tag{3.16}$$

where α, m, and n' are material parameters and the relation $m = 1 - 1/n'$ is assumed. $P^C (= P^G - P^W)$ is the suction and s_{re} is the effective degree of saturation, namely,

$$s_{re} = \frac{(s - s_{min})}{(s_{max} - s_{min})} \tag{3.17}$$

where s_{min} and s_{max} are the minimum and maximum saturation values, respectively.

3.5.2 Permeability of Unsaturated Soils

The coefficient of permeability for an unsaturated soil is a function of any two of three possible volume-mass properties, namely, degree of saturation, void ratio, and water content (Lambe and Whitman, 1969; Lloret and Alonso, 1980). In the present analysis, the permeability is assumed to be affected by the degree of saturation and void ratio. Using the van Genuchten type of permeability functions, the effect of degree of saturation on permeability for water and air are assumed as

$$k^W = k_s^W s_{re}^a \left\{1 - (1 - s_{re}^{\frac{1}{m}})^m\right\}^2, \qquad k^G = k_s^G (1 - s_{re})^b \left\{1 - (s_{re}^{\frac{1}{m}})\right\}^{2m} \tag{3.18}$$

where k^W and k^G are the coefficients of permeability for water and for gas respectively, a and b are the material parameters, and m and n' are the parameters in the van Genuchten equation (van Genuchten 1980). k_s^W is the coefficient of permeability for water under saturated conditions at a given void ratio, and k_s^G is the permeability of gas under fully dry conditions.

During the simulation process, Equations (3.18) lead to some numerical instability due to the large gradient presented when the saturation approaches to 1.0. To overcome this problem, Garcia et al. (2010) suggested the following equations

$$k^W = k_s^W s_{re}^a \left\{1 - (1 - s_{re}^{\frac{1}{m}})^{n'}\right\}, \qquad k^G = k_s^G (1 - s_{re})^b \left\{1 - (s_{re}^{\frac{1}{m}})^{n'}\right\} \tag{3.19}$$

k_s^W and k_s^G depend on void ratio, e, in the following form:

$$k_s^W = k_{s0}^W \exp\left[(e - e_0)/C_k\right], \qquad k_s^G = k_{s0}^G \exp\left[(e - e_0)/C_k\right] \tag{3.20}$$

in which k_{s0}^W and k_{s0}^G are the initial value for k_s^W and k_s^G at $e = e_0$, respectively. C_k is the material constant governing the rate of changes in permeability subjected to changes in void ratio.

3.6 Governing Equations

3.6.1 Assumptions

The following assumptions are considered to formulate the governing equations:

1. The relative accelerations of the fluid phases (gas and water phases) to that of the solid phase are much smaller than the acceleration of the solid phase (u-p formulation).
2. The solid grain particles are incompressible.
3. The distribution of solid, water, and gas phases in the porous media is sufficiently smooth.
4. The mass density of the water and the soil skeleton are spatially homogeneous.
5. Different components of the multiphase mixture have the same temperature, and it is assumed to be constant.
6. The body force is smoothly distributed in space.

3.6.2 Conservation of Mass

In the Eulerian framework, by ignoring mass exchanges among the phases, the balance of mass for each phase is expressed by

$$\frac{d^\alpha}{dt} \int_V \rho_\alpha n^\alpha dV = 0 \qquad (\alpha = S, W, G) \tag{3.21}$$

in which V is an arbitrary volume, ρ_α is the mass density, and n^α is the volume fraction for the phase α in the current state.

In Equation (3.21), $\frac{d^\alpha}{dt}$ is the material time derivative with respect to phase α, which is expressed as

$$\frac{d^\alpha()}{dt} = \frac{\partial()}{\partial t} + \mathbf{v}^\alpha.\nabla() \tag{3.22}$$

where $\mathbf{v}^\alpha$ is the velocity vector of phase α.

Transforming the current volume to the reference volume ($dV = JdV_0$), Equation (3.21) can be written as

$$\int_{V_0} \frac{d^\alpha}{dt}(\rho_\alpha n^\alpha J)dV_0 = 0 \qquad (\alpha = S, W, G) \tag{3.23}$$

in which V_0 is the volume in the reference state, and J is the Jacobian of deformation which is defined as

$$\varepsilon_{pqr}J = \varepsilon_{ijk}\frac{\partial x_i}{\partial X_p}\frac{\partial x_j}{\partial X_q}\frac{\partial x_k}{\partial X_r} \tag{3.24}$$

With V_0 being arbitrary, we get

$$\frac{d^\alpha}{dt}(\rho_\alpha n^\alpha J) = 0 \tag{3.25}$$

Or, equivalently:

$$J\frac{d^\alpha}{dt}(\rho_\alpha n^\alpha) + \rho_\alpha n^\alpha \frac{d^\alpha}{dt}(J) = 0 \tag{3.26}$$

The material derivative of each individual term of Equation (3.24) becomes

$$\frac{d^\alpha}{dt}(\frac{\partial x_i}{\partial X_j}) = \frac{\partial}{\partial X_j}\frac{d^\alpha x_i}{dt} = \frac{\partial v_i^\alpha}{\partial X_j} \tag{3.27}$$

Using the above equation, the material time derivative of the Jacobian becomes

$$\frac{d^\alpha}{dt}(J) = (\nabla.\mathbf{v}^\alpha)J \tag{3.28}$$

Substituting Equation (3.28) into Equation (3.26), we obtain

$$\frac{d^\alpha}{dt}(\rho_\alpha n^\alpha) + \rho_\alpha n^\alpha v_{i,i}^\alpha = 0 \tag{3.29}$$

Or, equivalently:

$$\frac{\partial}{\partial t}(n^\alpha \rho_\alpha) + (n^\alpha \rho_\alpha v_i^\alpha)_{,i} = 0 \tag{3.30}$$

In the mixture theory it is assumed that at any arbitrary volume element dV, the particles of the solid phase, water phase, and gas phase exist together (See Figure 3.1). Based

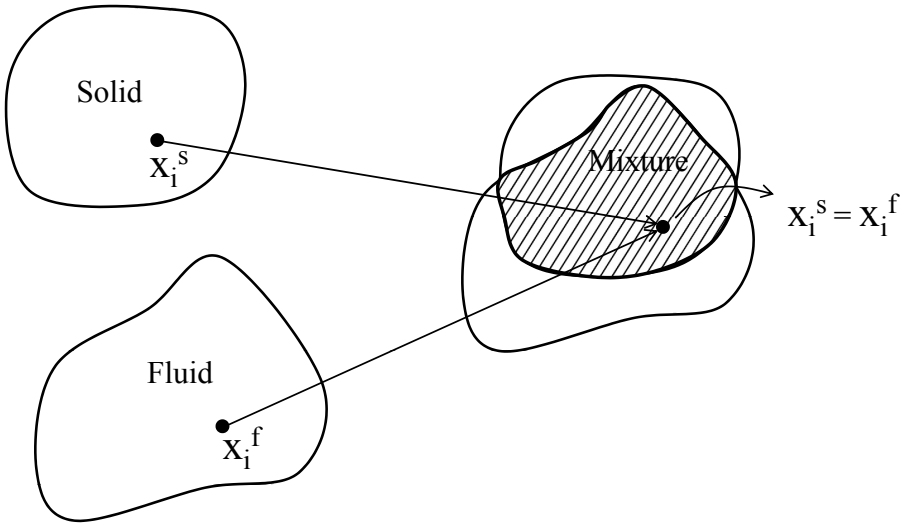

Figure 3.1 Solid and fluid constituents, and the mixture

on this assumtion and by using Equations (3.4), (3.6), and (3.29) the mass conservation law for the solid, the liquid, and the gas phases are expressed as

$$S: \quad -\dot{n}\rho_S + (1-n)\rho_S v^S_{i,i} = 0 \tag{3.31}$$

$$W: \quad \dot{n}s\rho_W + n\dot{s}\rho_W + ns\rho_W v^W_{i,i} = 0 \tag{3.32}$$

$$G: \quad (1-s)\dot{n}\rho_G - n\dot{s}\rho_G + n(1-s)\dot{\rho_G} + n(1-s)\rho_G v^G_{i,i} = 0 \tag{3.33}$$

In these equations a superimposed dot denotes the material time derivative of the mixture. Note that in Equations (3.31) to (3.33) it has been assumed that the soil particles and water are incompressible.

Dividing both sides of Equation (3.31) by $\frac{\rho_S}{s}$, and Equation (3.32) by ρ_W, and adding these equations together yield

$$n\dot{s} + sv^S_{i,i} + ns(v^W_i - v^S_i)_{,i} = 0 \tag{3.34}$$

The relative velocity vector of water and gas with respect to the solid phase is defined as:

$$\dot{w}^\beta_i = n^\beta(v^\beta_i - v^S_i) \qquad \beta = W, G \tag{3.35}$$

Substituting $\dot{w}^W_i$ into Equation (3.34), the mass conservation equation for water can

finally be obtained, that is,

$$sD_{ii} + \dot{s}n = -\dot{w}^W_{i,i} \tag{3.36}$$

where D_{ij} is the stretching tensor, namely,

$$D_{ij} = \frac{1}{2}(L_{ij} + L_{ji}) \tag{3.37}$$

in which L_{ij} is the velocity gradient tensor, namely,

$$L_{ij} = v^S_{i,j} \tag{3.38}$$

The mass conservation law for gas is obtained from Equations (3.31) and (3.33).

Dividing both sides of Equation (3.31) by $\frac{\rho_S}{(1-s)}$, and Equation (3.33) by ρ_G, and adding these equations yield

$$-n\dot{s} + n(1-s)\frac{\dot{\rho}_G}{\rho_G} + (1-s)v^S_{i,i} + n(1-s)(v^G_i - v^S_i)_{,i} = 0 \tag{3.39}$$

Substituting $\dot{w}^G_i$ into Equation (3.39), the mass conservation equation for gas can be obtained, that is,

$$(1-s)D_{ii} - \dot{s}n + (1-s)n\frac{\dot{\rho}_G}{\rho_G} = -\dot{w}^G_{i,i} \tag{3.40}$$

3.6.3 Conservation of Linear Momentum

The conservation of linear momentum states that, for any part of a body and at any time, the change of the linear momentum is equal to the sum of all forces acting on that part.

In the Eulerian framework, the balance of momentum for each phase can be expressed as

$$\int_\Gamma \mathbf{T}^\alpha d\Gamma + \int_V \rho_\alpha \mathbf{b} n^\alpha dV + \int_V \sum_\beta \mathbf{h}^{\alpha\beta} dV = \frac{d^\alpha}{dt}\int_V \rho_\alpha \mathbf{v}^\alpha n^\alpha dV \quad (\alpha, \beta = S, W, G) \tag{3.41}$$

where V and Γ are the volume and the area of any part of the body in the current state, respectively. Also, for phase α, $\mathbf{T}^\alpha$ is the partial Cauchy stress, $\mathbf{b}$ is the body force per unit mass, and $\mathbf{h}^{\alpha\beta}$ is the density of the internal force exerted by phase α on phase β ($\mathbf{h}^{\alpha\beta} = -\mathbf{h}^{\beta\alpha}$).

The right hand side of the Equation (3.41) can be expressed as

$$\frac{d^\alpha}{dt}\int_V \rho_\alpha \mathbf{v}^\alpha n^\alpha dV = \int_V \rho_\alpha n^\alpha \mathbf{a}^\alpha dV + \int_{V_0} \mathbf{v}^\alpha \frac{d^\alpha}{dt}(\rho_\alpha n^\alpha J) dV_0 \tag{3.42}$$

where $\mathbf{a}^\alpha$ is the acceleration vector:

$$\mathbf{a}^\alpha = \frac{d^\alpha \mathbf{v}^\alpha}{dt} = \frac{\partial \mathbf{v}^\alpha}{\partial x} + (\mathbf{v}^\alpha . \triangledown)\mathbf{v}^\alpha \tag{3.43}$$

According to Equation (3.25) from the conservation of mass, the last term in Equation (3.42) becomes zero. Using Cauchy's stress theorem and gauss theorem, Equation (3.41) in index notation becomes

$$\int_V T^\alpha_{ji,j} dV + \int_V \rho_\alpha b_i n^\alpha dV + \int_V \sum_\beta h_i^{\alpha\beta} dV = \int_V \rho_\alpha n^\alpha a_i^\alpha dV \tag{3.44}$$

With V being arbitrary, Equation (3.44)localizes to

$$T^\alpha_{ji,j} + \rho_\alpha n^\alpha b_i + \sum_\beta h_i^{\alpha\beta} = \rho_\alpha n^\alpha a_i^\alpha \qquad (\alpha = S, W, G) \tag{3.45}$$

Using Equation (3.45), the momentum balance equation for solid (S), water (W), and gas (G) phases can, respectively, be written as:

$$S \;:\; T^S_{ji,j} + \rho_S n^S b_i + h_i^{SW} + h_i^{SG} = \rho_S n^S a_i^S \tag{3.46}$$

$$W \;:\; T^W_{ji,j} + \rho_W n^W b_i + h_i^{WS} + h_i^{WG} = \rho_W n^W a_i^W \tag{3.47}$$

$$G \;:\; T^G_{ji,j} + \rho_G n^G b_i + h_i^{GS} + h_i^{GW} = \rho_G n^G a_i^G \tag{3.48}$$

We assume that the interaction between the liquid phase and the gas phase is too small. Thus,

$$h_i^{WG} \simeq 0 \tag{3.49}$$

Moreover, the interaction terms h_i^{SW} and h_i^{SG} can be defined as

$$h_i^{SW} = \frac{n^W \gamma_W}{k^W} \dot{w}_i^W \tag{3.50}$$

$$h_i^{SG} = \frac{n^G \gamma_G}{k^G} \dot{w}_i^G \tag{3.51}$$

where k^W and k^G are the coefficients of permeability for water and for gas, respectively, which were defined in Equation (3.19). Also, $\dot{w}_i^W$ is the average velocity vector of water

with respect to the solid skeleton, and $\dot{w}_i^G$ is the average velocity vector of gas to the solid skeleton, which were defined in Equation (3.35).

Using Equation (3.35), Equations (3.47) and (3.48) become

$$\rho_\beta n^\beta (a_i^S + \frac{1}{n^\beta}\ddot{w}_i^\beta) + h_i^{S\beta} = T_{ji,j}^\beta + \rho_\beta n^\beta b_i \qquad (\beta = W, G) \tag{3.52}$$

Based on assumption (1) ($\ddot{w}_i^\beta = 0$), and using Equations (3.10), (3.11), (3.50), and (3.51), Equation (3.52) becomes

$$\rho_\beta n^\beta a_i^S + \frac{n^\beta \gamma_\beta}{k^\beta}\dot{w}_i^\beta = -n^\beta P_{,i}^\beta + \rho_\beta n^\beta b_i \tag{3.53}$$

After manipulation, the average relative velocity vectors of fluid phases to the solid skeleton can be shown as

$$\dot{w}_i^\beta = \frac{k^\beta}{\gamma_\beta}(-P_{,i}^\beta - \rho_\beta a_i^S + \rho_\beta b_i) \qquad (\beta = W, G) \tag{3.54}$$

3.6.4 Equation of Motion for the Whole Mixture

Based on the conservation laws of linear momentum, we can derive the equation of motion for the whole mixture. The sum of the Equations (3.46)-(3.48) gives

$$T_{ji,j} + \rho b_i = \rho_S n^S a_i^S + \rho_W n^W a_i^W + \rho_G n^G a_i^G \tag{3.55}$$

where

$$\rho = \sum_\alpha \rho_\alpha n^\alpha \qquad (\alpha = S, W, G) \tag{3.56}$$

In Equation (3.55), T_{ij} is the total Cauchy stress tensor which is obtained from the sum of the partial Cauchy stress values, T_{ij}^α, namely,

$$T_{ij} = \sum_\alpha T_{ij}^\alpha \qquad (\alpha = S, W, G) \tag{3.57}$$

Equation (3.55) can be written in an alternative form:

$$T_{ji,j} + \rho b_i = \rho a_i^S + \rho_W n^W (a_i^W - a_i^S) + \rho_G n^G (a_i^G - a_i^S) \tag{3.58}$$

From assumption (1), we can disregard the relative accelerations for the u-p formulation. Therefore, the above equation becomes

$$T_{ji,j} + \rho b_i = \rho a_i^S \tag{3.59}$$

which represents the equation of motion for the whole multiphase mixture.

3.6.5 Continuity Equations for the Fluid Phases

For the fluid phases, the continuity equations are obtained from the incorporation of their conservation of momentum equations into their mass balance equations.

Substituting Equation (3.54) into Equation (3.36), for the liquid phase we get

$$\frac{k^W}{\gamma_W}(-P^W_{,ii} - \rho_W a^S_{i,i} + \rho_W b_{i,i}) + sD_{ii} + \dot{s}n = 0 \tag{3.60}$$

From assumption (6), $b_{i,i} = 0$ holds. Using the relation $a^S_{i,i} = \dot{D}_{ii}$, Equation (3.60) can be written as

$$\rho_W \dot{D}_{ii} + P^W_{,ii} - \frac{\gamma_W}{k^W}(sD_{ii} + \dot{s}n) = 0 \tag{3.61}$$

This equation is called "continuity equation of the liquid phase".

Similarly, we can derive the continuity equation for the gas phase. Substituting Equation (3.54) into Equation (3.40), we obtain

$$\rho_G \dot{D}_{ii} + P^G_{,ii} - \frac{\gamma_G}{k^G}\left\{(1-s)D_{ii} - \dot{s}n + (1-s)n\frac{\dot{\rho_G}}{\rho_G}\right\} = 0 \tag{3.62}$$

To describe the changes in gas density, the equation for ideal gases is used as

$$\rho_G = \frac{MP^G}{R\theta} \tag{3.63}$$

$$\dot{\rho}_G = \frac{M}{R}\left(\frac{\dot{P}^G}{\theta} - \frac{P^G\dot{\theta}}{\theta^2}\right) \tag{3.64}$$

in which M is the molecular weight of gas, R is the gas constant, and θ is the temperature.

Dividing Equation (3.64) by Equation (3.63) yields

$$\frac{\dot{\rho_G}}{\rho_G} = \frac{\dot{P}^G}{P^G} - \frac{\dot{\theta}}{\theta} \tag{3.65}$$

Based on assumption (5), the temperature is assumed to be constant, namely, $\dot{\theta}$ =0. Equation (3.65) becomes

$$\frac{\dot{\rho_G}}{\rho_G} = \frac{\dot{P}^G}{P^G} \tag{3.66}$$

Therefore, Equation (3.62) becomes

$$\rho_G \dot{D}_{ii} + P^G_{,ii} - \frac{\gamma_G}{k^G}\left\{(1-s)D_{ii} - \dot{s}n + (1-s)n\frac{\dot{P^G}}{P^G}\right\} = 0 \tag{3.67}$$

This equation is called "continuity equation of the gas phase".

3.7 Lagrangian Description of the Equation of Motion

In large deformation problems that involve time-dependent constitutive models, material points must be followed. This is not convenient to implement in Eulerian framework, while it can be expressed more naturally in lagrangian scheme. In this section, the equation of motion obtained in the Eulerian framework is expressed in Lagrangian form. For this purpose, the nominal stress (the first Piola-Kirchhoff stress) tensor is defined as an alternative definition of stress in the reference state.

In Eulerian framework, the equation of motion derived in section 3.6.4 can be rewritten as

$$\int T_{ji,j} dV = \int \rho(a_i - b_i) dV \tag{3.68}$$

in which $a_i \equiv a_i^S$.

The relation between the Cauchy stress tensor and the nominal stress tensor (Π_{ij}) is expressed as

$$\int T_{ji} n_j d\Gamma = \int \Pi_{ji} N_j d\Gamma_0 \tag{3.69}$$

in which $d\Gamma_0$ and N_j are, respectively, defined as the area of the element and its unit normal vector in the reference state. $d\Gamma$ and n_j are, also, the area of the element and its unit normal vector in the current state, respectively.

Using Gauss theorem, Equation (3.69) becomes

$$\int T_{ji,j} dV = \int \Pi_{ji,j} dV_0 \tag{3.70}$$

The nominal mass density ρ_0 can be defined by

$$\rho_0(\mathbf{X}) = \frac{M \text{ in current state}}{V \text{ in reference state}} \tag{3.71}$$

Based on this definition, we have

$$\rho_0 dV_0 = \rho dV \tag{3.72}$$

Using Equations (3.70) and (3.72), Equation (3.68) becomes

$$\int_{V0} \Pi_{ji,j} dV_0 = \int_{V0} \rho_0 (a_i - b_i) dV_0 \tag{3.73}$$

With the volume V_0 being arbitrary, we get

$$\Pi_{ji,j} = \rho_0 (a_i - b_i) \tag{3.74}$$

It is worth noting that in contrast with Cauchy stress tensor, the nominal stress tensor is not a symmetric tensor. Also, note that in Equation (3.74) the body force (b_i) and the acceleration (a_i) are still kept in the current state, and not in the reference state.

3.8 Spatial Discretization of the Governing Equations Using Finite Element Method

3.8.1 Discretization of the Equations of Motion

In this study, the updated Lagrangian method is employed, for which the configuration at time t, i.e., the latest known configuration, is considered as the reference configuration and the configuration at time $t + \Delta t$ is unknown.

The no rate type of the equation of motion for multiphase porous media, Equation (3.74), at time $t + \Delta t$ is expressed as

$$\rho_0 (a_i - b_i) - \Pi_{ji,j} = 0 \tag{3.75}$$

in which Π_{ij} is called the total nominal stress tensor.

As shown in Figure 3.2, the boundary conditions for the whole multiphase porous media are considered as:

$$\Pi_{ji} N_j = \bar{t}_i \qquad \text{on } \Gamma_t \tag{3.76}$$

$$v_i = \bar{v}_i \qquad \text{on } \Gamma_u \tag{3.77}$$

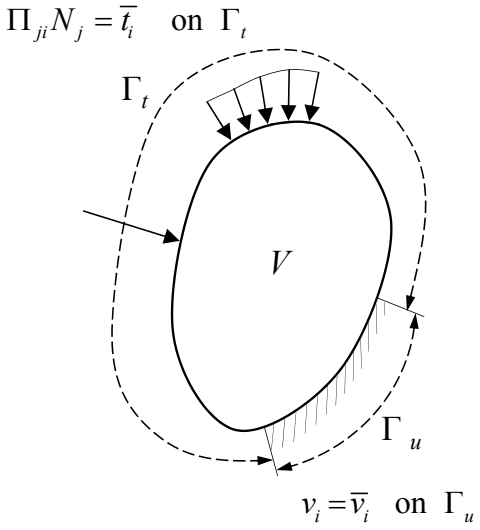

Figure 3.2 Boundary conditions for the whole multiphase mixture

where Γ_t is the traction boundary surface, Γ_u is the displacement boundary surface, N_j is an outward unit normal vector of the surface Γ_t in the reference state, t_i is the traction vector at time $t + \Delta t$, and v_i is the velocity vector of the solid phase. Also, the specified values are designated by a superimposed bar. This decomposition of the boundary satisfies

$$\Gamma_t \cup \Gamma_u = \Gamma \quad \text{and} \quad \Gamma_t \cap \Gamma_u = \emptyset \tag{3.78}$$

From the virtual work theorem, the weak form of the equation of motion is given by

$$\int_V \left\{\rho_0 \left(a_i - b_i\right) - \Pi_{ji,j}\right\} \delta v_i dV + \lambda \int_{\Gamma_t} \left(\Pi_{ji}N_j - \bar{t}_i\right) \delta v_i d\Gamma = 0 \tag{3.79}$$

where $v_i \equiv v_i^S$, and λ is an arbitrary scalar.

Considering λ equal to 1, and using integration by parts and Gauss theorem, Equation (3.79) becomes

$$\int_V \rho_0 a_i \delta v_i dV + \int_V \Pi_{ji} \delta L_{ij} dV = \int_{\Gamma_t} \bar{t}_i \delta v_i d\Gamma + \int_V \rho_0 b_i \delta v_i dV \tag{3.80}$$

The total nominal stress Π_{ij} at time $t + \Delta t$ can be approximated by

$$\Pi_{ij} \mid_{t+\Delta t} \cong \Pi_{ij} \mid_t + (\Delta t)\dot{\Pi}_{ij} \tag{3.81}$$

Based on Nanson's theorem, we have

$$n_i d\Gamma = JF_{ji}^{-1} N_j d\Gamma_0 \tag{3.82}$$

where $F_{ij}(= \frac{\partial x_i}{\partial X_j})$ is the deformation gradient tensor, and J is its Jacobian determinant defined as $J = det(F_{ij})$.

Using Equation (3.82), the relation between the Cauchy stress tensor and the total nominal stress tensor (Equation (3.69)) becomes

$$\Pi_{ji} = JF_{jp}^{-1} T_{pi} \tag{3.83}$$

The nominal stress rate tensor is obtained by differentiating the above equation with respect to time:

$$\dot{\Pi}_{ji} = JF_{jp}^{-1} \dot{\hat{S}}_{pi} \tag{3.84}$$

$$\dot{\hat{S}}_{pi} = \dot{T}_{pi} + L_{kk} T_{pi} - L_{pk} T_{ki} \tag{3.85}$$

As mentioned before, in updated-Lagrangian formulation we choose the current configuration (at time t) as the reference. Therefore,

$$\text{at time } t \ : \quad \begin{cases} JF_{ij}^{-1} = \delta_{ij} \\ \Pi_{ij} \mid_t = T_{ij} \mid_t \\ \dot{\Pi}_{ij} = \dot{\hat{S}}_{ij} \end{cases} \tag{3.86}$$

in which $\dot{\hat{S}}_{ij}$ is the nominal stress rate with respect to the current configuration at time t, and δ_{ij} is Kronecker's delta.

Using Equations (3.81) and (3.86), Equation (3.80) becomes

$$\int_V \rho a_i \delta v_i dV + \int_V T_{ij|t} \delta L_{ij} dV + (\Delta t) \int_V \dot{S}_{ji} \delta L_{ij} dV = \int_{\Gamma_t} \bar{t}_i \delta v_i d\Gamma + \int_V \rho b_i \delta v_i dV \tag{3.87}$$

where ρ is the density at current time t.

Using Equation (3.15), the relations among nominal stress rate $\dot{\hat{S}}_{ij}$, nominal skeleton stress rate $\dot{\hat{S}}'_{ij}$, and Cauchy's skeleton stress T'_{ij} are

$$\dot{\hat{S}}_{ij} = \dot{\hat{S}}'_{ij} - \dot{P}^F \delta_{ij} - L_{kk} P^F \delta_{ij} + P^F L_{ji} \tag{3.88}$$

where

$$\dot{\hat{S}}'_{ij} = \dot{T'}_{ij} + L_{kk}T'_{ij} - L_{ik}T'_{kj} \tag{3.89}$$

The term $\dot{T'}_{ij}\delta L_{ij}$ can be written as

$$\dot{T'}_{ij}\delta L_{ij} = \dot{T'}_{ij}\delta D_{ij} \tag{3.90}$$

where

$$\delta L_{ij} = \delta D_{ij} + \delta W_{ij} \tag{3.91}$$

$$\delta D_{ij} = \frac{1}{2}(\delta L_{ij} + \delta L_{ji}) \tag{3.92}$$

$$\delta W_{ij} = \frac{1}{2}(\delta L_{ij} - \delta L_{ji}) \tag{3.93}$$

From the above relations, Equation (3.87) becomes

$$\begin{aligned}\int_V \rho a_i \delta v_i dV + (\Delta t)\int_V \dot{T'}_{ij}\delta D_{ij}dV - (\Delta t)\int_V T'_{ik}L_{jk}\delta L_{ij}dV + (\Delta t)\int_V T'_{ij}L_{kk}\delta L_{ij}dV \\ - (\Delta t)\int_V \dot{P}^F \delta D_{kk}dV - (\Delta t)\int_V (L_{kk}P^F\delta_{ij} - P^F L_{ji})\delta L_{ij}dV \\ = \int_\Gamma \bar{t}_i \delta v_i d\Gamma + \int_V \rho b_i \delta v_i dV - \int_V T_{ij} \mid_t \delta L_{ij}dV\end{aligned} \tag{3.94}$$

Taking acceleration vector $\{a_N\}$, velocity vector $\{v_N\}$, and the average pressure of the fluids $\{P_N^F\}$, at time $t + \Delta t$ as unknown variables at nodal points, Equation (3.94) can be written in matrix form as:

$$\begin{aligned}\int_V \rho\{\delta v\}^T\{a\}dV + (\Delta t)\int_V \{\delta D\}^T\{\dot{T'}\}dV + (\Delta t)\int_V \{\delta L\}^T[D_s]\{L\}dV \\ + (\Delta t)\int_V \{\delta L\}^T\{T'\}(trL)dV - (\Delta t)\int_V (tr\delta D)^T\dot{p}^F dV \\ - (\Delta t)\int_V \{\delta L\}^T[U]\{L\}dV = \int_\Gamma \{\delta v\}^T\{\bar{t}\}d\Gamma \\ + \int_V \rho\{\delta v\}^T\{b\}dV - \int_V \{\delta L\}^T\{T\}_t dV\end{aligned} \tag{3.95}$$

where

$$-T'_{ik}L_{jk} = [D_s]\{L\} \tag{3.96}$$

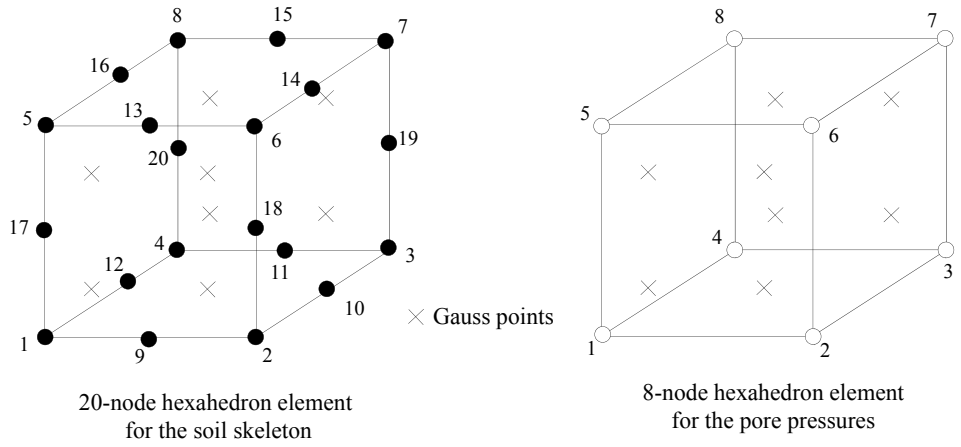

Figure 3.3 Isoparametric elements for the soil skeleton and the pore pressures

$$(L_{kk}p^F\delta_{ij} - p^F L_{ji}) = [U]\{L\} \tag{3.97}$$

Now we set the following definitions as:

$$\{v\} = [N]\{v_N\} \tag{3.98}$$

$$\{a\} = [N]\{a_N\} \tag{3.99}$$

$$\{D\} = [B]\{v_N\} \tag{3.100}$$

$$trD = \{B_v\}^T\{v_N\} \tag{3.101}$$

$$\{L\} = [N_L]\{v_N\} \tag{3.102}$$

$$\dot{P}^F = \{N_h\}^T\{\dot{P}_N^F\} \tag{3.103}$$

In the present study, we use isoparametric elements, namely, 20-node element for the displacement, the velocity, and the acceleration of the solid skeleton and 8-node element for the pore pressures (Figure 3.3) .

In the updated-Lagrangian formulation, since the reference configuration is updated at each iterative procedure, it is necessary to use objective stress and strain rates which are frame-invariant rates. The Jaumann rate of Cauchy's skeleton stress tensor, $\hat{T}_{ij}$, is objective and defined as

$$\hat{T}'_{ij} = \dot{T}'_{ij} + T'_{ik}W_{kj} - W_{ik}T'_{kj} \tag{3.104}$$

where W_{ij} is the spin tensor.

For large deformations, the stretching tensor D_{ij}, which is objective, is assumed to be a composition of elastic stretching tensor D^e_{ij} and viscoplastic stretching tensor D^{vp}_{ij}, that is,

$$D_{ij} = D^e_{ij} + D^{vp}_{ij} \tag{3.105}$$

For large deformations the constitutive relation between elastic stretching tensor D^e_{ij} and the Jaumann rate of Cauchy stress tensor $\hat{T'}_{ij}$ is expressed as

$$\hat{T'}_{ij} = C^e_{ijkl} D^e_{kl} \tag{3.106}$$

where C^e_{ijkl} is the elastic stiffness matrix.

From the flow rule, viscoplastic stretching tensor D^{vp}_{ij} is given by

$$D^{vp}_{ij} = \gamma < \Phi(f_y) > \frac{\partial f_p}{\partial T'_{ij}} \tag{3.107}$$

where $<>$ are Macaulay's brackets; $< \Phi(f_y) > = \phi(f_y)$, if $f_y > 0$ and $< \Phi(f_y) > = 0$, if $f_y \leq 0$.

Herein, the tangent modulus method as will be shown in section (3.10) is adopted in order to evaluate viscoplastic stretching tensor D^{vp}_{ij}

$$\{\hat{T'}\} = [C]\{D\} - \{Q\} \tag{3.108}$$

where $[C]$ is the tangential stiffness matrix, and $\{Q\}$ is the relaxation stress vector. Substituting Equation (3.104) into Equation (3.108) yields

$$\{\dot{T'}\} = [C]\{D\} - \{Q\} + \{W^*\} \tag{3.109}$$

where,

$$\{W^*\} = W_{ik} T'_{kj} - T'_{ik} W_{kj} \tag{3.110}$$

Since Equation (3.95) is valid for each arbitrary virtual velocity δv_N, this equation

becomes

$$\begin{aligned}\int_V \rho[N]^T[N]dV\{a_N\} + (\Delta t)\int_V [B]^T[C][B]dV\{v_N\} + (\Delta t)\int_V [B]^T\{W^*\}dV \\ - (\Delta t)\int_V [B]^T\{Q\}dV + (\Delta t)\int_V [N_L]^T[D_s][N_L]dV\{v_N\} \\ + (\Delta t)\int_V [N_L]^T\{T'\}\{B_v\}^T dV\{v_N\} - (\Delta t)\int_V \{B_v\}\{N_h\}^T dV\{\dot{P}_N^F\} \\ - (\Delta t)\int_V [N_L]^T[U][N_L]dV\{v_N\} = \int_\Gamma [N]^T\{\bar{t}\}d\Gamma \\ + \int_V \rho[N]^T\{b\}dV - \int_V [N_L]^T\{T\}_t dV\end{aligned} \tag{3.111}$$

The terms of Equation (3.111) are defined as

$$[M] = \rho\int_V [N]^T[N]dV \tag{3.112}$$

$$[K] = \int_V [B]^T[C][B]dV \tag{3.113}$$

$$\{T_W\} = \int_V [B]^T\{W^*\}dV - \int_V [B]^T\{Q\}dV \tag{3.114}$$

$$[K_L] = \int_V [N_L]^T[D_s][N_L]dV - \int_V [N_L]^T[U][N_L]dV + \int_V [N_L]^T\{T'\}\{B_v\}^T dV \tag{3.115}$$

$$[K_v] = \int_V \{B_v\}\{N_h\}^T dV \tag{3.116}$$

$$\{F\} = \int_\Gamma [N]^T\{\bar{t}\}d\Gamma + \rho\int_V [N]^T\{b\}dV \tag{3.117}$$

$$\{T^*\}_t = \int_V [N_L]^T\{T\}_t dV \tag{3.118}$$

From the above relations, Equation (3.111) can be expressed by

$$[M]\{a_N\} + (\Delta t)([K] + [K_L])\{v_N\} - (\Delta t)[K_v]\{\dot{P}_N^F\} + (\Delta t)\{T_W\} = \{F\} - \{T^*\}_t \tag{3.119}$$

According to Equation (3.13), the time derivative of P^F can be expressed as

$$\begin{aligned}\dot{P}^F &= \frac{\partial}{\partial t}\left\{sP^W + (1-s)P^G\right\} \\ &= \left\{\frac{\partial s}{\partial P^C}(P^W - P^G) + (1-s)\right\}\dot{P}^G + \left\{-\frac{\partial s}{\partial P^C}(P^W - P^G) + s\right\}\dot{P}^W \\ &= \left\{A_s + (1-s)\right\}\dot{P}^G + \left\{-A_s + s\right\}\dot{P}^W\end{aligned} \tag{3.120}$$

where

$$A_s = \frac{\partial s}{\partial P^C}(P^W - P^G) \tag{3.121}$$

From the soil water characteristic curve defined in Equations (3.16) and (3.17), we have,

$$\frac{\partial s}{\partial P^C} = -\alpha m n'(s_{max} - s_{min})(\alpha P^C)^{n'-1}\left\{1 + (\alpha P^C)^{n'}\right\}^{-m-1} \tag{3.122}$$

We, then, add the Rayleigh damping $[R]$ which is proportional to the nodal velocity vector $\{v_N\}$. The Rayleigh damping can be described by the linear combination of mass matrix $[M]$ and stiffness matrix $[K]$:

$$[R] = \alpha_0[M] + \alpha_1[K] \tag{3.123}$$

where α_0 and α_1 are constants.

In the present study, we use the Rayleigh damping proportional to the initial stiffness matrix $[K]$. Finally, we obtain the spatial discretized equation of motion as

$$\begin{aligned}[M]\{a_N\} + \{(\Delta t)([K] + [K_L]) + [R]\}\{v_N\} - (-A_s + s)(\Delta t)[K_v]\{\dot{P}_N^W\} \\ - (A_s + (1 - s))(\Delta t)[K_v]\{\dot{P}_N^G\} + (\Delta t)\{T_W\} = \{F\} - \{T^*\}_t\end{aligned} \tag{3.124}$$

3.8.2 Discretization of the Continuity Equation for the Liquid Phase

For the liquid phase, the whole boundary surface Γ can be decomposed into Γ_P^W, boundary where the pore water pressure is prescribed, and Γ_Q^W, boundary where the gradient of the pore water pressure is prescribed.

As Figure 3.4 shows, the boundary conditions for the discretization of the continuity equation of the liquid phase are expressed as

$$P^W = \bar{P}^W \qquad \text{on } \Gamma_P^W \tag{3.125}$$

$$\frac{\partial P^W}{\partial x_i} = \bar{q}_i^W \qquad \text{on } \Gamma_Q^W \tag{3.126}$$

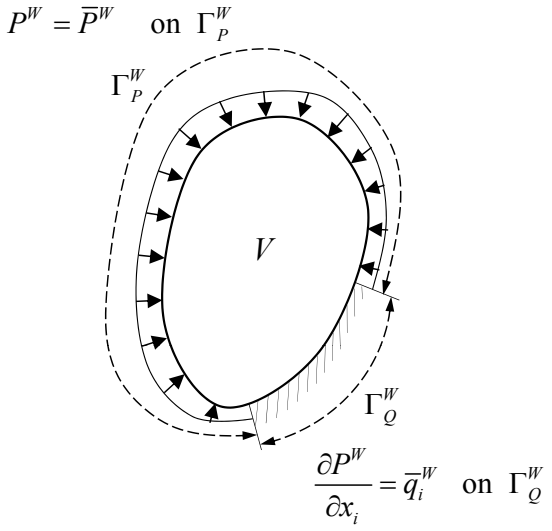

Figure 3.4 Boundary conditions for the liquid phase

where $\bar{P}^W$ is the water pressure applied on the boundary Γ_P^W, and $\bar{q}_i^W$ is the gradient of the water pressure on the boundary Γ_Q^W. Γ_P^W and Γ_Q^W satisfy the following relations:

$$\Gamma_P^W \cup \Gamma_Q^W = \Gamma \quad \text{and} \quad \Gamma_P^W \cap \Gamma_Q^W = \emptyset \tag{3.127}$$

From Equation (3.61), the weak form of the continuity equation for water is given as

$$\int_V \left\{ \rho_W \dot{D}_{ii} + P_{,ii}^W - \frac{\gamma_W}{k^W}(sD_{ii} + \dot{s}n) \right\} \delta P^W dV + \lambda \int_{\Gamma_Q^W} (P_{,i}^W - \bar{q}_i^W) \delta P^W n_i d\Gamma = 0 \tag{3.128}$$

where δP^W is the test function for the pore water pressure, and λ is an arbitrary scalar.

By integrating by parts and using Gauss's divergence theorem, we have

$$\int_V P_{,ii}^W \delta P^W dV = \int_\Gamma P_{,i}^W \delta P^W n_i d\Gamma - \int_V P_{,i}^W \delta P_{,i}^W dV \tag{3.129}$$

Considering λ equal to -1, and using Equations (3.125), (3.126), and (3.129), Equation (3.128) becomes

$$\rho_W \int_V \dot{D}_{ii} \delta P^W dV - \int_V P_{,i}^W \delta P_{,i}^W dV - \frac{\gamma_W}{k^W} \int_V (sD_{ii} + \dot{s}n) \delta P^W dV = - \int_{\Gamma_Q^W} \bar{q}_i^W \delta P^W n_i d\Gamma \tag{3.130}$$

Considering the fact that the degree of saturation, s, is the single-variation function of suction P^C, $\dot{s}$ can be given as

$$\dot{s} = \frac{\partial s}{\partial P^C} \frac{\partial P^C}{\partial t} = \frac{\partial s}{\partial P^C} (\dot{P}^G - \dot{P}^W) \tag{3.131}$$

Taking acceleration vector $\{a_N\}$, velocity vector $\{v_N\}$, the pore water pressure $\{P_N^W\}$, and the pore gas pressure $\{P_N^G\}$ as four unknown variables at nodal points, Equation (3.130) can be expressed in matrix form as

$$\begin{aligned}\rho_W \int_V \delta P^{W^T} \dot{D}_{ii} dV - \int_V \{\delta P_{,i}^W\}^T \{P_{,i}^W\} dV - \frac{\gamma_W}{k^W} \int_V \delta P^{W^T} s D_{ii} dV \\ - \frac{\gamma_W}{k^W} \int_V \delta P^{W^T} n \frac{\partial s}{\partial P^C} (\dot{P}^G - \dot{P}^W) dV = - \int_{\Gamma_Q^W} \delta P^{W^T} \{n\}^T \{\bar{q}^W\} d\Gamma\end{aligned} \tag{3.132}$$

Definitions include the following:

$$P^\beta = \{N_h\}^T \{P_N^\beta\} \qquad (\beta = W, G) \tag{3.133}$$

$$\dot{P}^\beta = \{N_h\}^T \{\dot{P}_N^\beta\} \qquad (\beta = W, G) \tag{3.134}$$

$$\{P_{,i}^\beta\} = [N_{h,i}] \{P_N^\beta\} \qquad (\beta = W, G) \tag{3.135}$$

$$D_{ii} = \{B_v\}^T \{v_N\} \tag{3.136}$$

$$\dot{D}_{ii} = \{B_v\}^T \{a_N\} \tag{3.137}$$

Since the test function $\{\delta P_N^W\}^T$ is arbitrary, by using Equations (3.133)-(3.137), Equation (3.132) becomes

$$\begin{aligned}\rho_W \int_V \{N_h\}\{B_v\}^T dV \{a_N\} - \int_V [N_{h,i}]^T [N_{h,i}] dV \{P_N^W\} - \frac{\gamma_W}{k^W} \int_V s \{N_h\}\{B_v\}^T dV \{v_N\} \\ - \frac{\gamma_W}{k^W} \int_V \{N_h\} n \frac{\partial s}{\partial P^C} \{N_h\}^T dV \left(\{\dot{P}_N^G\} - \{\dot{P}_N^W\}\right) = - \int_{\Gamma_Q^W} \{N_h\}\{n\}^T \{\bar{q}^W\} d\Gamma\end{aligned} \tag{3.138}$$

The terms in Equation (3.138) are defined as

$$[K_v]^T = \int_V \{N_h\}\{B_v\}^T dV \tag{3.139}$$

$$[K_h] = \int_V [N_{h,i}]^T [N_{h,i}] dV \tag{3.140}$$

$$[K_n] = \int_V \{N_h\}\{N_h\}^T dV \tag{3.141}$$

$$\{q^W\} = \int_{\Gamma_Q^W} \{N_h\}\{n\}^T \{\bar{q}^W\} d\Gamma \tag{3.142}$$

Finally, the spatial discretized form of the continuity equation for the liquid phase is given by

$$\begin{aligned}\rho_W [K_v]^T \{a_N\} - (\frac{\gamma_W}{k^W}) s [K_v]^T \{v_N\} - [K_h]\{P_N^W\} \\ + (\frac{\gamma_W}{k^W}) n \frac{\partial s}{\partial P^C} [K_n] \{\dot{P}_N^W\} - (\frac{\gamma_W}{k^W}) n \frac{\partial s}{\partial P^C} [K_n] \{\dot{P}_N^G\} = -\{q^W\}\end{aligned} \tag{3.143}$$

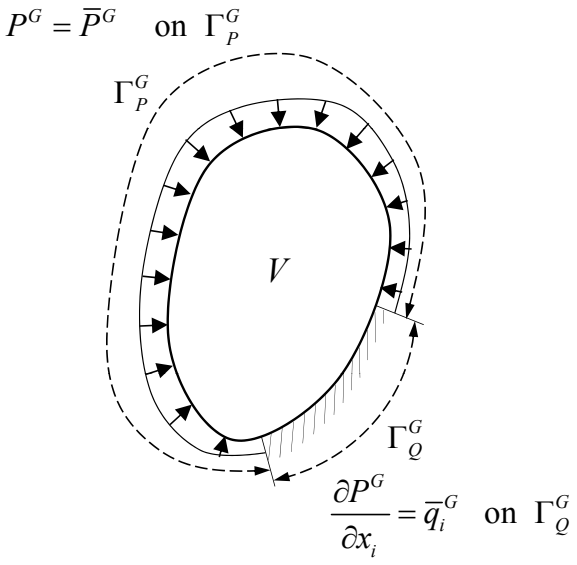

Figure 3.5 Boundary conditions for the gas phase

3.8.3 Discretization of the Continuity Equation for the Gas Phase

For the gas phase, the whole boundary surface Γ can be decomposed into Γ_P^G, boundary where the pore gas pressure is prescribed, and Γ_Q^G, boundary where the gradient of the pore gas pressure is prescribed.

As Figure 3.5 shows, the boundary conditions for the discretization of the continuity equation of the gas phase are expressed as

$$P^G = \bar{P}^G \qquad \text{on } \Gamma_P^G \tag{3.144}$$

$$\frac{\partial P^G}{\partial x_i} = \bar{q}_i^G \qquad \text{on } \Gamma_Q^G \tag{3.145}$$

where $\bar{P}^G$ is the gas pressure applied on the boundary Γ_P^G, and $\bar{q}_i^G$ is the gradient of the gas pressure on the boundary Γ_Q^G. Γ_P^G and Γ_Q^G satisfy the following relations:

$$\Gamma_P^G \cup \Gamma_Q^G = \Gamma \quad \text{and} \quad \Gamma_P^G \cap \Gamma_Q^G = \emptyset \tag{3.146}$$

From Equation (3.67), the weak form of the continuity equation for gas is given as

$$\int_V \left\{ \rho_G \dot{D}_{ii} + P^G_{,ii} - \frac{\gamma_G}{k^G} \left((1-s) D_{ii} - \dot{s} n + (1-s) n \frac{\dot{P}^G}{P^G} \right) \right\} \delta P^G dV + \lambda \int_{\Gamma_Q^G} (P^G_{,i} - \bar{q}_i^G) \delta P^G n_i d\Gamma = 0 \tag{3.147}$$

where δP^G is the test function for the pore gas pressure, and λ is an arbitrary scalar.

By integrating by parts and using Gauss's divergence theorem, we have

$$\int_V P^G_{,ii}\delta P^G dV = \int_\Gamma P^G_{,i}\delta P^G n_i d\Gamma - \int_V P^G_{,i}\delta P^G_{,i} dV \tag{3.148}$$

Considering λ equal to -1, and using Equations (3.144), (3.145), and (3.148), Equation (3.147) becomes

$$\begin{aligned}&\rho_G \int_V \dot{D}_{ii}\delta P^G dV - \int_V P^G_{,i}\delta P^G_{,i} dV \\ &- \frac{\gamma_G}{k^G}\int_V \left((1-s)D_{ii} - \dot{s}n + (1-s)n\frac{\dot{P}^G}{P^G}\right)\delta P^G dV = -\int_{\Gamma^G_Q} \bar{q}^G_i \delta P^G n_i d\Gamma\end{aligned} \tag{3.149}$$

Using Equation (3.131) , and taking acceleration vector $\{a_N\}$, velocity vector $\{v_N\}$, the pore water pressure $\{P^W_N\}$, and the pore gas pressure $\{P^G_N\}$ as four unknown variables at nodal points, Equation (3.149) can be expressed in matrix form as

$$\begin{aligned}&\rho_G \int_V \delta P^{G^T}\dot{D}_{ii} dV - \int_V \{\delta P^G_{,i}\}^T\{P^G_{,i}\}dV - \frac{\gamma_G}{k^G}\int_V \delta P^{G^T}(1-s)D_{ii}dV \\ &+ \frac{\gamma_G}{k^G}\int_V \delta P^{G^T} n\frac{\partial s}{\partial P^C}(\dot{P}^G - \dot{P}^W)dV - \frac{\gamma_G}{k^G}\int_V (1-s)n\delta P^{G^T}\frac{\dot{P}^G}{P^G}dV \\ &= -\int_{\Gamma^G_Q} \delta P^{G^T}\{n\}^T\{\bar{q}^G\}d\Gamma\end{aligned} \tag{3.150}$$

Since the test function $\{\delta P^G_N\}^T$ is arbitrary, by using Equations (3.133)-(3.137), Equation (3.150) becomes

$$\begin{aligned}&\rho_G \int_V \{N_h\}\{B_v\}^T dV\{a_N\} - \int_V [N_{h,i}]^T[N_{h,i}]dV\{P^G_N\} - \frac{\gamma_G}{k^G}\int_V (1-s)\{N_h\}\{B_v\}^T dV\{v_N\} \\ &+ \frac{\gamma_G}{k^G}\int_V \{N_h\}n\frac{\partial s}{\partial P^C}\{N_h\}^T dV\left(\{\dot{P}^G_N\} - \{\dot{P}^W_N\}\right) - \frac{\gamma_G}{k^G}\int_V (1-s)n\frac{\{N_h\}\{N_h\}^T}{P^G_t}dV\{\dot{P}^G_N\} \\ &= -\int_{\Gamma^G_Q}\{N_h\}\{n\}^T\{\bar{q}^G\}d\Gamma\end{aligned} \tag{3.151}$$

where P^G_t is the pore gas pressure at time t.

The terms in Equation (3.151) are defined as

$$[K_v]^T = \int_V \{N_h\}\{B_v\}^T dV \tag{3.152}$$

$$[K_h] = \int_V [N_{h,i}]^T[N_{h,i}]dV \tag{3.153}$$

$$[K_n] = \int_V \{N_h\}\{N_h\}^T dV \tag{3.154}$$

$$[K_c^P] = \int_V \frac{\{N_h\}\{N_h\}^T}{P_t^G} dV \tag{3.155}$$

$$\{q^G\} = \int_{\Gamma_Q^G} \{N_h\}\{n\}^T \{\bar{q}^G\} d\Gamma \tag{3.156}$$

Finally, the spatial discretized form of the continuity equation for the gas phase is given by

$$\begin{aligned} &\rho_G [K_v]^T \{a_N\} - (\frac{\gamma_G}{k^G})(1-s)[K_v]^T \{v_N\} - [K_h]\{P_N^G\} \\ &- (\frac{\gamma_G}{k^G}) n \frac{\partial s}{\partial P^C} [K_n]\{\dot{P}_N^W\} + (\frac{\gamma_G}{k^G}) n \frac{\partial s}{\partial P^C} [K_n]\{\dot{P}_N^G\} \\ &- \frac{\gamma_G}{k^G}(1-s) n [K_c^P]\{\dot{P}_N^G\} = -\{q^G\} \end{aligned} \tag{3.157}$$

3.9 Time Discretization of the Governing Equations

Using Newmark β method, the displacement and the velocity of the soil skeleton can be approximated as

$$\{u_N\}_{t+\Delta t} = \{u_N\}_t + (\Delta t)\{v_N\}_t + \frac{(\Delta t)^2}{2}\{a_N\}_t + \beta(\Delta t)^2(\{a_N\}_{t+\Delta t} - \{a_N\}_t) \tag{3.158}$$

$$\{v_N\}_{t+\Delta t} = \{v_N\}_t + (\Delta t)\{a_N\}_t + \gamma(\Delta t)(\{a_N\}_{t+\Delta t} - \{a_N\}_t) \tag{3.159}$$

where Δt is the time increment, and γ and β are the Newmark's parameters.

For the rate of pore pressures, a backward finite difference method is used as

$$\{\dot{P}_N^\beta\}_{t+\Delta t} = \frac{\{P_N^\beta\}_{t+\Delta t} - \{P_N^\beta\}_t}{\Delta t} \qquad (\beta = W, G) \tag{3.160}$$

Considering that the equation of motion holds at time $t + \Delta t$, and applying Equations

(3.159) and (3.160) to Equation (3.124), the final discretized equation of motion becomes

$$\begin{aligned}
&[M]_{t+\Delta t}\{a_N\}_{t+\Delta t} + \gamma(\Delta t)\left\{([K]_{t+\Delta t} + [K_L]_{t+\Delta t})\Delta t + [R]_{t+\Delta t}\right\}\{a_N\}_{t+\Delta t} \\
&\qquad - (-A_s + s)[K_v]_{t+\Delta t}\{P_N^W\}_{t+\Delta t} \\
&\qquad - (A_s + (1-s))[K_v]_{t+\Delta t}\{P_N^G\}_{t+\Delta t} \\
&\qquad = \{F\}_{t+\Delta t} - \{T^*\}_t - (\Delta t)\{T_W\}_t \\
&\qquad - \left\{([K]_{t+\Delta t} + [K_L]_{t+\Delta t})\Delta t + [R]_{t+\Delta t}\right\}\left[(\Delta t)(1-\gamma)\{a_N\}_t + \{v_N\}_t\right] \\
&\qquad - (-A_s + s)[K_v]_{t+\Delta t}\{P_N^W\}_t \\
&\qquad - (A_s + (1-s))[K_v]_{t+\Delta t}\{P_N^G\}_t
\end{aligned} \tag{3.161}$$

Substituting Equations (3.159) and (3.160) into Equation (3.143), the final discretized continuity equation for the liquid phase is obtained as

$$\begin{aligned}
&\Delta t\left(\rho_W - \frac{\gamma_W(\Delta t)\gamma}{k^W}s\right)[K_v]_{t+\Delta t}^T\{a_N\}_{t+\Delta t} \\
&\quad + \left(-(\Delta t)[K_h]_{t+\Delta t} + (\frac{\gamma_W}{k^W})n\frac{\partial s}{\partial P^C}[K_n]_{t+\Delta t}\right)\{P_N^W\}_{t+\Delta t} \\
&\quad - (\frac{\gamma_W}{k^W})n\frac{\partial s}{\partial P^C}[K_n]_{t+\Delta t}\{P_N^G\}_{t+\Delta t} \\
&\quad = -(\Delta t)\{q^W\}_{t+\Delta t} + (\Delta t)(\frac{\gamma_W}{k^W})s[K_v]_{t+\Delta t}^T\left(\Delta t(1-\gamma)\{a_N\}_t + \{v_N\}_t\right) \\
&\quad + (\frac{\gamma_W}{k^W})n\frac{\partial s}{\partial P^C}[K_n]_{t+\Delta t}\left(\{P_N^W\}_t - \{P_N^G\}_t\right)
\end{aligned} \tag{3.162}$$

For the gas phase, the final discretized continuity equation is obtained by substituting Equations (3.159) and (3.160) into Equation (3.157):

$$\begin{aligned}
&\Delta t\left(\rho_G - \frac{\gamma_G(\Delta t)\gamma}{k^G}(1-s)\right)[K_v]_{t+\Delta t}^T\{a_N\}_{t+\Delta t} \\
&\quad + \left\{-\Delta t[K_h]_{t+\Delta t} + \frac{\gamma_G}{k^G}n\left(\frac{\partial s}{\partial P^C}[K_n]_{t+\Delta t} - (1-s)[K_c^P]_{t+\Delta t}\right)\right\}\{P_N^G\}_{t+\Delta t} \\
&\quad - \frac{\gamma_G}{k^G}n\frac{\partial s}{\partial P^C}[K_n]_{t+\Delta t}\{P_N^W\}_{t+\Delta t} \\
&\quad = -\Delta t\{q^G\}_{t+\Delta t} + \Delta t\frac{\gamma_G}{k^G}(1-s)[K_v]_{t+\Delta t}^T\left(\Delta t(1-\gamma)\{a_N\}_t + \{v_N\}_t\right) \\
&\quad + \frac{\gamma_G}{k^G}n\frac{\partial s}{\partial P^C}[K_n]_{t+\Delta t}\left(\{P_N^G\}_t - \{P_N^W\}_t\right) \\
&\quad - \frac{\gamma_G}{k^G}n(1-s)[K_c^P]_{t+\Delta t}\{P_N^G\}_t
\end{aligned} \tag{3.163}$$

3.10 Tangent Stiffness Method

In this section, the nonlinear relation between the Jaumann rate of Cauchy's stress and the stretching tensor for elasto-viscoplastic materials is derived using the tangent stiffness method proposed by Peirce et al. (1984). The tangent stiffness method was developed for rate dependent materials based on a one-step forward gradient time integration scheme. This method results in more stability and accuracy for step sizes much larger than that can be employed with the Euler method. A parameter, termed θ, has been introduced in this method, which can range from 0 to 1, with $\theta = 0$ corresponding to a simple Euler time integration scheme. Through the numerical examples on materials ranging from elastic-nonlinearly viscous behavior to nearly rate independent behavior, Peirce et al. (1984) found that the method is stable and accurate for the values of θ between 0.5 and 1.0.

As shown earlier, the total stretching tensor is divided to the elastic stretching tensor D^e_{ij} and the viscoplastic stretching tensor D^{vp}_{ij}, in which the viscoplastic stretching tensor is given by

$$D^{vp}_{ij} = C_{ijkl} \left\langle \Phi \left(f_y \right) \right\rangle \frac{\partial f_p}{\partial T'_{kl}} \tag{3.164}$$

Material function $\Phi \left(f_y \right)$ is assumed to dependent on the effective Cauchy stress tensor T'_{ij}, and the kinematic hardening parameters y^*_{m1} and χ^*_{ij}. Therefore, the time derivative of material function is written as

$$\dot{\Phi} \left(f_y \right) = \frac{\partial \Phi}{\partial T'_{ij}} \dot{T}'_{ij} + \frac{\partial \Phi}{\partial y^*_{m1}} \dot{y}^*_{m1} + \frac{\partial \Phi}{\partial \chi^*_{ij}} \dot{\chi}^*_{ij} \tag{3.165}$$

The rate of effective Cauchy stress is related to the Jaumann rate of Cauchy stress as

$$\hat{T}'_{ij} = \dot{T}'_{ij} + T'_{ik} W_{kj} - W_{ik} T'_{kj} \tag{3.166}$$

where $W_{ij}$is the spin vector.

Using two arbitrary scalars, A and B, and a symmetric tensor U_{ij}, we can write

$$\begin{aligned} \frac{\partial \Phi}{\partial T'_{ij}} \hat{T}_{ij} &= \frac{\partial \Phi}{\partial T'_{ij}} \left(\dot{T}'_{ij} + T'_{ik} W_{kj} - W_{ik} T'_{kj} \right) \\ &= \frac{\partial \Phi}{\partial T'_{ij}} \dot{T}'_{ij} + \frac{\partial \Phi}{\partial T'_{ij}} \left(T'_{ik} W_{kj} - W_{ik} T'_{kj} \right) \\ &= \frac{\partial \Phi}{\partial T'_{ij}} \dot{T}'_{ij} + \left(A U_{ij} + B \delta_{ij} \right) \left(T'_{ik} W_{kj} - W_{ik} T'_{kj} \right) \end{aligned} \tag{3.167}$$

in which $AU_{ij}\left(-W_{ik}T'_{kj}+T'_{ik}W_{kj}\right)=0$ and $B\delta_{ij}\left(-W_{ik}T'_{kj}+T'_{ik}W_{kj}\right)=0$, therefore

$$\frac{\partial\Phi}{\partial T'_{ij}}\hat{T}_{ij}=\frac{\partial\Phi}{\partial T'_{ij}}\dot{T}'_{ij} \tag{3.168}$$

Finally, by substituting Equation (3.168) into Equation (3.165), we have

$$\dot{\Phi}\left(f_y\right)=\frac{\partial\Phi}{\partial T'_{ij}}\hat{T}'_{ij}+\frac{\partial\Phi}{\partial y^*_{m1}}\dot{y}^*_{m1}+\frac{\partial\Phi}{\partial\chi^*_{ij}}\dot{\chi}^*_{ij} \tag{3.169}$$

Using the tangent stiffness parameter θ yields

$$\Phi=\left(1-\theta\right)\Phi_t+\theta\Phi_{t+\Delta t} \tag{3.170}$$

in which

$$\Phi_{t+\Delta t}=\Phi_t+\Delta\Phi=\Phi_t+\Delta t\dot{\Phi}_t \tag{3.171}$$

Applying Equations (3.169), (3.170), and (3.171), we obtain

$$\Phi=\left(1-\theta\right)\Phi_t+\theta\left\{\Phi_t+\frac{\partial\Phi}{\partial T'_{ij}}\hat{T}'_{ij}\Delta t+\frac{\partial\Phi}{\partial y^*_{m1}}\dot{y}^*_{m1}\Delta t+\frac{\partial\Phi}{\partial\chi^*_{ij}}\dot{\chi}^*_{ij}\Delta t\right\} \tag{3.172}$$

The constitutive equation is described using the Jaumann rate of Cauchy stress tensor $\hat{T}'_{ij}$ and stretching tensor D_{ij} as

$$\begin{aligned}\hat{T}'_{ij}&=C^e_{ijkl}\left(D_{kl}-D^{vp}_{kl}\right)\\&=C^e_{ijkl}\left(D_{kl}-C_{klmn}\Phi\frac{\partial f_p}{\partial T'_{mn}}\right)\end{aligned} \tag{3.173}$$

And, the kinematic hardening parameters, y^*_{m1} and χ^*_{ij}, are given by

$$\dot{y}^*_{m1}=B^*_2\left(A^*_2D^{vp}_{kk}-y^*_{m1}\left|D^{vp}_{kk}\right|\right) \tag{3.174}$$

$$\dot{\chi}^*_{ij}=B^*\left\{A^*D^{'vp}_{ij}-\chi^*_{ij}\left(D^{'vp}_{mn}D^{'vp}_{mn}\right)^{\frac{1}{2}}\right\} \tag{3.175}$$

where $D^{'vp}_{ij}$ is the viscoplastic deviatoric stretching tensor, and D^{vp}_{kk} is the viscoplastic volumetric stretching tensor. According to the cyclic elasto-viscoplastic constitutive equations and if we assume C_{ijkl} is a fourth order isotropic tensor, the viscoplastic volumetric and deviatoric stretching tensor are obtained as

$$D^{vp}_{kk}=C_{kkij}\Phi\frac{\partial f_p}{\partial T'_{ij}} \tag{3.176}$$

$$D_{ij}^{'vp} = D_{ij}^{vp} - \frac{1}{3} D_{kk}^{vp} \delta_{ij} = C_{ijkl} \Phi \frac{\partial f_p}{\partial S_{kl}} \tag{3.177}$$

Substituting the above equations into Equation (3.172) results in

$$\begin{aligned} \Phi = (1-\theta)\,\Phi_t + \theta \left\{ \Phi_t + \frac{\partial \Phi}{\partial T_{ij}^{'}} C_{ijkl}^{e} \left(D_{kl} - D_{kl}^{vp}\right) \Delta t + \frac{\partial \Phi}{\partial y_{m1}^{*}} B_2^{*} \left(A_2^{*} D_{kk}^{vp} - y_{m1}^{*} \left|D_{kk}^{vp}\right|\right) \Delta t \right. \\ \left. + \frac{\partial \Phi}{\partial \chi_{ij}^{*}} B^{*} \left\{ A^{*} D_{ij}^{'vp} - \chi_{ij}^{*} \left(D_{mn}^{'vp} D_{mn}^{'vp} \right)^{\frac{1}{2}} \right\} \Delta t \right\} \end{aligned} \tag{3.178}$$

$$\begin{aligned} \Phi = \Phi_t &+ \theta \frac{\partial \Phi}{\partial T_{ij}^{'}} C_{ijkl}^{e} D_{kl} \Delta t - \theta\, \Delta t \Phi \frac{\partial \Phi}{\partial T_{ij}^{'}} C_{ijkl}^{e} C_{klmn} \frac{\partial f_p}{\partial T_{mn}^{'}} \\ &+ \theta\, \Delta t \Phi \frac{\partial \Phi}{\partial y_{m1}^{*}} B_2^{*} \left(A_2^{*} C_{kkij} \frac{\partial f_p}{\partial T_{ij}^{'}} - y_{m1}^{*} \left| C_{kkij} \frac{\partial f_p}{\partial T_{ij}^{'}} \right| \right) \\ &+ \theta\, \Delta t \Phi \frac{\partial \Phi}{\partial \chi_{ij}^{*}} B^{*} \left\{ A^{*} C_{ijkl} \frac{\partial f_p}{\partial S_{kl}} - \chi_{ij}^{*} \left(C_{mnpq} \frac{\partial f_p}{\partial S_{pq}} C_{mnrs} \frac{\partial f_p}{\partial S_{rs}} \right)^{\frac{1}{2}} \right\} \end{aligned} \tag{3.179}$$

and finally

$$\Phi = \frac{1}{1+\xi'} \left\{ \Phi_t + (\theta\, \Delta t) \frac{\partial \Phi}{\partial T_{ij}^{'}} C_{ijkl}^{e} D_{kl} \right\} \tag{3.180}$$

in which,

$$\begin{aligned} \xi' = (\theta\, \Delta t) \left\{ \frac{\partial \Phi}{\partial T'_{ij}} C_{ijkl}^{e} C_{klmn} \frac{\partial f_p}{\partial T'_{mn}} - \frac{\partial \Phi}{\partial y_{m1}^{*}} B_2^{*} \left(A_2^{*} C_{kkij} \frac{\partial f_p}{\partial T'_{ij}} - y_{m1}^{*} \left| C_{kkij} \frac{\partial f_p}{\partial T'_{ij}} \right| \right) \right. \\ \left. - \frac{\partial \Phi}{\partial \chi_{ij}^{*}} B^{*} \left(A^{*} C_{ijkl} \frac{\partial f_p}{\partial S_{kl}} - \chi_{ij}^{*} \left(C_{mnpq} \frac{\partial f_p}{\partial S_{pq}} C_{mnrs} \frac{\partial f_p}{\partial S_{rs}} \right)^{\frac{1}{2}} \right) \right\} \end{aligned} \tag{3.181}$$

Thus, substituting Equation (3.180) into Equation (3.164) results in

$$D_{ij}^{vp} = C_{ijkl} \frac{1}{1+\xi'} \left\{ \Phi_t + (\theta\, \Delta t) \frac{\partial \Phi}{\partial T'_{pq}} C_{pqrs}^{e} D_{rs} \right\} \frac{\partial f_p}{\partial T_{kl}^{'}} \tag{3.182}$$

Combining Equations (3.173) and (3.182), we obtain

$$\begin{aligned} \hat{T}_{ij}^{'} &= C_{ijkl}^{e} \left(D_{kl} - C_{klmn} \frac{1}{1+\xi'} \left\{ \Phi_t + (\theta\, \Delta t) \frac{\partial \Phi}{\partial T_{pq}^{'}} C_{pqrs}^{e} D_{rs} \right\} \frac{\partial f_p}{\partial T_{mn}^{'}} \right) \\ &= \left[C_{ijkl}^{e} - C_{ijrs}^{e} C_{rsmn} \frac{\partial f_p}{\partial T_{mn}^{'}} \frac{1}{1+\xi'} (\theta\, \Delta t) \frac{\partial \Phi}{\partial T_{pq}^{'}} C_{pqkl}^{e} \right] D_{kl} - C_{ijkl}^{e} C_{klmn} \frac{\partial f_p}{\partial T_{mn}^{'}} \frac{1}{1+\xi'} \Phi_t \end{aligned} \tag{3.183}$$

Thereby, tangential stiffness matrix $C^{\tan}_{ijkl}$ and relaxation stress Q_{ij} are defined as

$$C^{\tan}_{ijkl} = C^{e}_{ijkl} - C^{e}_{ijrs} C_{rsmn} \frac{\partial f_p}{\partial T'_{mn}} \frac{1}{1+\xi'} (\theta \, \Delta t) \frac{\partial \Phi}{\partial T'_{pq}} C^{e}_{pqkl} \tag{3.184}$$

$$Q_{ij} = C^{e}_{ijkl} C_{klmn} \frac{\partial f_p}{\partial T'_{mn}} \frac{1}{1+\xi'} \Phi_t \tag{3.185}$$

Then, the Equation (3.183) can be rewritten as

$$\hat{T}'_{ij} = C^{\tan}_{ijkl} D_{kl} - Q_{ij} \tag{3.186}$$

3.10.1 Differential Components

The differential components of material function derivation are calculated according to the material function definition and chain rule. As explained earlier, material function is determined as

$$\Phi\left(f_y\right) = \sigma'_m \exp\left\{m'\left(f_y\right)\right\} \tag{3.187}$$

$$\Phi\left(f_y\right) = \sigma'_m \exp\left\{m'\left(\bar{\eta}^*_{\chi} + \tilde{M}^*\left(\ln \frac{\sigma'_{mk}}{\sigma'_{ma}} + \left|\ln \frac{\sigma'_m}{\sigma'_{mk}} - y^*_{m1}\right|\right)\right)\right\} \tag{3.188}$$

Hence,

$$\frac{\partial \Phi}{\partial \sigma'_{ij}} = \frac{\partial \Phi}{\partial \sigma'_m} \frac{\partial \sigma'_m}{\partial \sigma'_{ij}} + \frac{\partial \Phi}{\partial f_y} \frac{\partial f_y}{\partial \sigma'_{ij}} \tag{3.189}$$

$$\frac{\partial \Phi}{\partial y^*_{m1}} = \frac{\partial \Phi}{\partial f_y} \frac{\partial f_y}{\partial y^*_{m1}} \tag{3.190}$$

$$\frac{\partial \Phi}{\partial \chi^*_{ij}} = \frac{\partial \Phi}{\partial f_y} \frac{\partial f_y}{\partial \chi^*_{ij}} \tag{3.191}$$

where

$$\frac{\partial \Phi}{\partial \sigma'_m} = \exp\left\{m'\left(f_y\right)\right\} + m'\sigma'_m \exp\left\{m'\left(f_y\right)\right\} \frac{\partial f_y}{\partial \sigma'_m} \tag{3.192}$$

$$\frac{\partial \sigma'_m}{\partial \sigma'_{ij}} = \frac{1}{3}\delta_{ij} \tag{3.193}$$

$$\frac{\partial \Phi}{\partial f_y} = m' \sigma'_m \exp\left\{m'\left(f_y\right)\right\} \tag{3.194}$$

$$\frac{\partial f_y}{\partial \sigma'_{ij}} = \frac{\partial f_y}{\partial \sigma'_m}\frac{\partial \sigma'_m}{\partial \sigma'_{ij}} + \frac{\partial f_y}{\partial S_{kl}}\frac{\partial S_{kl}}{\partial \sigma'_{ij}} \tag{3.195}$$

$$\frac{\partial f_y}{\partial y^*_{m1}} = -\tilde{M}^* \frac{\ln \frac{\sigma'_m}{\sigma'_{mk}} - y^*_{m1}}{\left|\ln \frac{\sigma'_m}{\sigma'_{mk}} - y^*_{m1}\right|} \tag{3.196}$$

$$\frac{\partial f_y}{\partial \chi^*_{ij}} = -\frac{\eta^*_{ij} - \chi^*_{ij}}{\bar{\eta}^*_\chi} \tag{3.197}$$

Considering $\dfrac{\partial \eta^*_{ij}}{\partial S_{kl}} = \dfrac{1}{\sigma'_m}\delta_{ik}\delta_{jl}$ and $\dfrac{\partial \eta^*_{ij}}{\partial \sigma'_m} = -\dfrac{S_{ij}}{\left(\sigma'_m\right)^2}$, the components of Equation (3.195) are given by

$$\frac{\partial f_y}{\partial \sigma'_m} = \frac{\eta^*_{ij} - \chi^*_{ij}}{\bar{\eta}^*_\chi}\left\{-\frac{S_{mn}}{\left(\sigma'_m\right)^2}\right\} + \frac{\tilde{M}^*}{\sigma'_m}\left(\frac{\ln \frac{\sigma'_m}{\sigma'_{mk}} - y^*_{m1}}{\left|\ln \frac{\sigma'_m}{\sigma'_{mk}} - y^*_{m1}\right|}\right) = \frac{1}{\sigma'_m}\left\{\tilde{M}^* \frac{\ln \frac{\sigma'_m}{\sigma'_{mk}} - y^*_{m1}}{\left|\ln \frac{\sigma'_m}{\sigma'_{mk}} - y^*_{m1}\right|} - \frac{\eta^*_{st}\left(\eta^*_{st} - \chi^*_{st}\right)}{\bar{\eta}^*_\chi}\right\} \tag{3.198}$$

$$\frac{\partial f_y}{\partial S_{ij}} = \frac{1}{\sigma'_m}\frac{\eta^*_{ij} - \chi^*_{ij}}{\bar{\eta}^*_\chi} \tag{3.199}$$

$$\frac{\partial S_{kl}}{\partial \sigma'_{ij}} = \frac{\partial\left(\sigma'_{kl} - \sigma'_m \delta_{kl}\right)}{\partial \sigma'_{ij}} = \delta_{ki}\delta_{lj} - \frac{1}{3}\delta_{ij}\delta_{kl} \tag{3.200}$$

Substituting Equation (3.193) and Equations (3.198) to (3.200) into Equation (3.195)

$$\frac{\partial f_y}{\partial \sigma'_{ij}} = \frac{\delta_{ij}}{3\sigma'_m}\left\{\tilde{M}^* \frac{\ln \frac{\sigma'_m}{\sigma'_{mk}} - y^*_{m1}}{\left|\ln \frac{\sigma'_m}{\sigma'_{mk}} - y^*_{m1}\right|} - \frac{\eta^*_{st}\left(\eta^*_{st} - \chi^*_{st}\right)}{\bar{\eta}^*_\chi}\right\} + \frac{\delta_{ik}\delta_{jl} - \frac{1}{3}\delta_{ij}\delta_{kl}}{\sigma'_m}\frac{\eta^*_{kl} - \chi^*_{kl}}{\bar{\eta}^*_\chi} \tag{3.201}$$

in which the second term of right-hand side equation can be rewritten as

$$\frac{\left(\delta_{ik}\delta_{jl} - \frac{1}{3}\delta_{ij}\delta_{kl}\right)}{\sigma'_m}\frac{\left(\eta^*_{kl} - \chi^*_{kl}\right)}{\bar{\eta}^*_\chi} = \frac{1}{\sigma'_m}\frac{\eta^*_{ij} - \chi^*_{ij} + \frac{\delta_{ij}\left(\chi^*_{pp} - \eta^*_{pp}\right)}{3}}{\bar{\eta}^*_\chi} \tag{3.202}$$

Since $\eta^*_{kk} = \dfrac{S_{kk}}{\sigma'_m} = 0$ and from the definition of the kinematic hardening parameter, we have

$$\dot{\chi}^*_{ij} = B^*\left\{A^* D^{'vp}_{ij} - \chi^*_{ij}\left(D^{'vp}_{mn} D^{'vp}_{mn}\right)^{\frac{1}{2}}\right\} \tag{3.203}$$

Considering $D_{kk}^{'vp} = 0$

$$\dot{\chi}_{pp}^{*} = -B^{*}\chi_{pp}^{*}\left(D_{mn}^{'vp}D_{mn}^{'vp}\right)^{\frac{1}{2}} \tag{3.204}$$

When $\chi_{pp}^{*} = 0$ at initial state, χ_{pp}^{*} is constantly zero. Therefore, Equation (3.201) becomes

$$\frac{\partial f_y}{\partial \sigma'_{ij}} = \frac{\delta_{ij}}{3\sigma'_{m}}\left\{\tilde{M}^{*}\frac{\ln\frac{\sigma'_{m}}{\sigma'_{mk}} - y_{m1}^{*}}{\left|\ln\frac{\sigma'_{m}}{\sigma'_{mk}} - y_{m1}^{*}\right|} - \frac{\eta_{st}^{*}\left(\eta_{st}^{*} - \chi_{st}^{*}\right)}{\bar{\eta}_{\chi}^{*}}\right\} + \frac{1}{\sigma'_{m}}\frac{\eta_{ij}^{*} - \chi_{ij}^{*}}{\bar{\eta}_{\chi}^{*}} \tag{3.205}$$

Since the static yield function f_y and the viscoplastic potential function f_p have the same shape, we have

$$\frac{\partial f_y}{\partial \sigma'_{ij}} = \frac{\partial f_p}{\partial \sigma'_{ij}} \tag{3.206}$$

$$\frac{\partial f_y}{\partial \sigma'_{m}} = \frac{\partial f_p}{\partial \sigma'_{m}} \tag{3.207}$$

$$\frac{\partial f_y}{\partial S_{ij}} = \frac{\partial f_p}{\partial S_{ij}} \tag{3.208}$$

3.11 Final Form of the Governing Equations

Combining Equations (3.161), (3.162), and (3.163) gives the final system of the governing equations for the finite element analysis as follows:

$$\begin{bmatrix} [M]_{t+\Delta t} \\ +\gamma(\Delta t)\left\{([K]_{t+\Delta t}+[K_L]_{t+\Delta t})\Delta t+[R]_{t+\Delta t}\right\} & -(-A_s+s)[K_v]_{t+\Delta t} & -(A_s+(1-s))[K_v]_{t+\Delta t} \\ \\ \Delta t\left(\rho_W-\frac{\gamma_W(\Delta t)\gamma}{k^W}s\right)[K_v]^T_{t+\Delta t} & -(\Delta t)[K_h]_{t+\Delta t}+(\frac{\gamma_W}{k^W})n\frac{\partial s}{\partial P^C}[K_n]_{t+\Delta t} & -(\frac{\gamma_W}{k^W})n\frac{\partial s}{\partial P^C}[K_n]_{t+\Delta t} \\ \\ \Delta t\left(\rho_G-\frac{\gamma_G(\Delta t)\gamma}{k^G}(1-s)\right)[K_v]^T_{t+\Delta t} & -\frac{\gamma_G}{k^G}n\frac{\partial s}{\partial P^C}[K_n]_{t+\Delta t} & -\Delta t[K_h]_{t+\Delta t} \\ & & +\frac{\gamma_G}{k^G}n\left(\frac{\partial s}{\partial P^C}[K_n]_{t+\Delta t}-(1-s)[K^P_c]_{t+\Delta t}\right) \end{bmatrix} \begin{Bmatrix} \{a_N\}_{t+\Delta t} \\ \{P^W_N\}_{t+\Delta t} \\ \{P^G_N\}_{t+\Delta t} \end{Bmatrix}$$

$$= \begin{Bmatrix} \{F\}_{t+\Delta t}-\{T^*\}_t-(\Delta t)\{T_W\}_t-\{([K]_{t+\Delta t}+[K_L]_{t+\Delta t})\Delta t+[R]_{t+\Delta t}\}\left[(\Delta t)(1-\gamma)\{a_N\}_t+\{v_N\}_t\right] \\ -(-A_s+s)[K_v]_{t+\Delta t}\{P^W_N\}_t-(A_s+(1-s))[K_v]_{t+\Delta t}\{P^G_N\}_t \\ \\ -(\Delta t)\{q^W\}_{t+\Delta t}+(\Delta t)(\frac{\gamma_W}{k^W})s[K_v]^T_{t+\Delta t}\left(\Delta t(1-\gamma)\{a_N\}_t+\{v_N\}_t\right) \\ +(\frac{\gamma_W}{k^W})n\frac{\partial s}{\partial P^C}[K_n]_{t+\Delta t}\left(\{P^W_N\}_t-\{P^G_N\}_t\right) \\ \\ -(\Delta t)\{q^G\}_{t+\Delta t}+\Delta t\frac{\gamma_G}{k^G}(1-s)[K_v]^T_{t+\Delta t}\left(\Delta t(1-\gamma)\{a_N\}_t+\{v_N\}_t\right) \\ +\frac{\gamma_G}{k^G}n\frac{\partial s}{\partial P^C}[K_n]_{t+\Delta t}\left(\{P^G_N\}_t-\{P^W_N\}_t\right)-\frac{\gamma_G}{k^G}n(1-s)[K^P_c]_{t+\Delta t}\{P^G_N\}_t \end{Bmatrix} \tag{3.209}$$

3.12 COMVI3D-DY011

During the 1990s, intensive efforts were put into understanding the mechanism of liquefaction and to develop methods to predict this phenomenon. Oka et al. (1994b) proposed a two-dimensional effective stress based liquefaction analysis method using the infinitesimal strain theory, and based on that method they developed the computer program "LIQCA2D" for the purpose of the dynamic analysis of grounds. In the 1995 Kobe earthquake it was, however, observed that very large deformation occurred in liquefied grounds near the structures; this made it necessary to develop the formulations based on the finite deformation theory. In 2001, Oka et al. presented the finite element formulation for large deformation dynamic analysis of fully saturated soils using elasto-plastic constitutive model, and then "LIQCA" code was extended to "LIQCA3D-FD".

Since many geotechnical problems have been encountered involving unsaturated soils, it is necessary "LIQCA3D-FD" is, also, extended for partially saturated soils. Due to the significant influences of suction force and degree of saturation on the soil behavior, the behavior of the soil in unsaturated condition is completely different from that in fully saturated state. This suggests that the assumption of fully saturated condition will not provide us with the real behavior of the soil in many geotechnical problems related to unsaturated soils. Hence, the major part of the present research was devoted to create a new computer program "COMVI3D-DY011" based on the new formulation presented in this chapter. By using "COMVI3D-DY011", it is possible to study the large deformation dynamic behavior of partially saturated elasto-viscoplastic soils. In the following the main principles of "COMVI3D-DY011" code are summarized:

COMVI3D-DY

- Elasto-plastic & Elasto-viscoplastic models
- Partially saturated case (3 phase)
  (Pore gas pressure considered as variable)
- 3 Dimensional
- Dynamic loads
- Based on finite deformation theory

3.13 Summary

In this chapter, the finite element formulation suitable for large deformation dynamic analysis was extended to the case of multiphase materials. Detailed derivations of the governing equations and the conservation laws of multiphase porous media were presented. Newmark's β method was adopted as a time integration algorithm to discretize the governing equations in time. The van Genuchten type of equation was, also, employed as a constitutive equation between the saturation and the suction. In addition, a new computer program entitled "COMVI3D-DY011" was introduced for the large deformation dynamic analysis of partially saturated elasto-viscoplastic soils.

Chapter 4

Dynamic Strain Localization in Partially Saturated Elasto-Viscoplastic Soil

4.1 Introduction

Strain localization is the phenomenon by which plastic deformations localize into narrow bands of intense straining. It is well known that strain localization, and in general plastic instability phenomena play important roles as precursors of the failure of geomaterials. In geomechanics, it has been recognized that brittle geomaterials are progressively strained and reach failure with shear banding and that a strain-softening phenomenon is observed in the stress-strain relation. The proper modeling of strain localization can be very significant in precautions against failure in such engineering problems as slope stability, borehole stability, liquefaction, and the stability of foundations, excavations, embankments, retaining walls, and faulting.

The problem of strain localization has been studied within the context of experimental, theoretical, and numerical approaches over the last three decades. Experimental studies on strain localization have been done with some visualization methods for measurements of local strain. Yoshida et al. (1994) studied the shear band generation of sand specimens under plane strain conditions by calculating the displacements of lattice points printed on a membrane. Similar observations using a printed membrane have been done by Liang et al. (1997), Hayano et al. (1999), and Kodaka et al. (2001). In order to observe strain localization inside specimens, X-Rays or X-Ray CTs have been used by many researchers, e.g., Han and Vardoulakis (1991), Oda and Kazama (1998), Otani et al. (2000), and

Alshibli et al. (2000). Michalowski and Shi (2003) calculated the displacements of grains of sand using an image analysis of sequential photographs by which the development of strain localization has been investigated. The stereophotogrammetric method is an efficient method for analyzing the development of shear bands used by Harris et al. (1995), Mokni and Desrues (1998), Rechenmacher and Medina-Cetina (2003), etc.

Some researchers have tried to observe strain localization under triaxial conditions (Burland 1990, Rampello 1991, etc.). Higo et al. (2006), and Kodaka et al. (2007) experimentally and numerically investigated the three-dimensional deformation behavior of rectangular clay specimens to obtain the distributions of shear strain during deformation. Oka et al. (2010) conducted drained and fully undrained triaxial compression tests for unsaturated compacted silt. They showed that the behavior of the soil can be described well through the use of the skeleton stress concept.

In recent experimental studies of strain localization, microfocus X-ray CT and X-ray micro CT provided a very high spatial resolution, which makes it possible to study microstructural changes of shear bands in the fine-grained sands (Oda et al. 2004; Matsushima et al. 2006; Hall et al. 2010; Higo et al. 2011).

The theoretical solution of strain localization had been previously conducted as material instability in rate-independent solids (Hadamard 1903, Rice 1976). In this case, the instability and ensuing ill-posedness of initial and boundary value problems were found to preclude meaningful analyses in rate-independent materials. In other words, under quasi-static loading conditions, the instability appears as an ellipticity loss in the rate equilibrium equations, while under dynamic loading conditions wave speeds become imaginary. Also, in the numerical solutions the instability exhibits inherent mesh dependence and spurious length scale effects (Needleman 1988, Loret and Prévost 1991).

In order to overcome this type of difficulty, various methods have been proposed which can be summarized into three approaches as described by Oka et al. (2002). The first approach is the introduction of viscoplastic effects in the numerical analysis. The viscoplasticity can be expressed by either assuming a viscoplastic constitutive model for material behavior, or a viscoplasticity regularization procedure within the numerical analysis, which is applied for inviscid constitutive model (e.g., Cormeau 1975, Needleman 1989, and Prévost and Loret 1990). The second method is applying higher order strain gradients into the constitutive model (e.g., Aifantis 1984, Muhlhaus and Aifantis 1991, de Borst and Sluys 1991, Aifantis et al. 1999, and Hutchinson 2001). In localization of multiphase materials, shear band development is mostly affected by the interaction between solid and fluid, in terms of time sequence of band formation and the way of their appearance.

Hence, the third method is to incorporate a Darcy type of soil-fluid interaction, which can alleviate the instability problem in multiphase materials by delaying the onset of material instability (e.g., Rice 1975, Loret and Prévost 1991, Oka et al. 1995, and Schrefler et al. 1996).

The present study deals with the behavior of clay in which the aspect of rate dependency comes naturally into the modeling to eliminate significantly the instability and subsequent influences in the analysis of strain localization problems under both quasi-static and dynamic loading conditions. When material rate dependence or viscosity is accounted for, there is no loss of ellipticity in the incremental equilibrium equations, wave speeds remain real, and consequently, the pathological mesh size effects do not occur (Needleman 1988). Furthermore, the inelastic response of geomaterials, such as clays, is inevitably rate dependent; therefore, the viscoplasticity can be effectively employed in the analysis, providing a satisfactory framework to capture localized shear banding.

From the numerical point of view, the strain localization of geomaterials has been widely studied using the soil-water coupled theory under quasi-static and dynamic loading conditions. Loret and Prévost (1991), Schrefler et al. (1995, 1996), and Ehlers and Volk (1998) numerically studied the localization problem of water-saturated geomaterials with the rate independent constitutive model. Under quasi-static deformations, Oka et al. (1994, 1995, 2000, and 2005) have studied the shear band development of water-saturated clays by using an elasto-viscoplastic constitutive model. They used the Biots type two-phase mixture theory in the formulation to reduce the material instability problems. They found that strain localization is closely linked to material instability, and it can be effectively simulated through the finite element analysis using the elasto-viscoplastic model, for both normally consolidated and over consolidated water-saturated clays. Oka et al. (2002) numerically examined the effects of dilatancy and permeability on strain localization using the model with the kinematic hardening theory. They showed that four shear bands were clearly formed through the fixed corner of the specimen in the cases of lower permeability levels, and the distance between the shear bands is shorter in the case of higher permeability. Loret and Rizzi (1999) numerically investigated the onset of strain localization in fluid-saturated anisotorpic porous media. Further, Zhang et al. (2000, 2001) simulated shear band dominated process in fully and partially saturated sand samples by means of dynamic strain localization analysis. Zhang and Schrefler (2001) discussed uniqueness and strain localization of elastoplastic saturated porous media.

It has been recognized that the behavior of unsaturated soils plays an important role in geomechanics. Many geotechnical problems such as landslide, the stability of embank-

ments, retaining walls, excavations, and soil containing methane hydrate can be related to partially saturated soils. On the other hand, the role of strain localization in deformation and progressive of failure in these engineering problems can be very significant. However, strain localization in partially saturated porous media has received less attention than fully saturated soils and single phase materials. In this chapter, the dynamic strain localization in saturated and partially saturated soils is numerically studied using finite element method and the cyclic elasto-viscoplastic constitutive model. In addition, mesh-size dependency is analyzed to provide stable and convergent solutions. Finally, the effects of the initial suction, acceleration, and confining pressure on shear band development are studied and discussed.

4.2 Problem Description

In this study, the strain localization of a homogeneous elasto-viscoplastic specimen in both saturated and unsaturated cases under the dynamic compressive loading is simulated. The finite element mesh and the boundary conditions for this problem are shown in Figure 4.1. The simulation is performed using a three-dimensional mesh system under plane strain conditions, for which the deformation in Y direction is constrained. The size of the specimen is assumed as 10 m in width and 20 m in height. The mesh pattern of 10×20 (200 elements) is considered as the default mesh configuration in the analysis. As mentioned in previous chapter, for the finite element analysis a 20-node hexahedron element with a reduced Gaussian integration is used to eliminate the shear locking and to reduce the appearance of a spurious hourglass mode.

In this analysis, the displacement boundary conditions are adjusted so as the symmetric conditions can be provided. The horizontal displacement at the corners of the specimen is fixed as a trigger for strain localization. All the boundaries are assumed to be impermeable to both water and gas, while the pore fluid is allowed to flow within the specimen. The specimen is subjected to an axial compressive acceleration distributed uniformly on the upper surface. The applied acceleration rises from zero to a maximum value of 3.5 gal within 0.1 sec, and remains constant afterward until 15.0 sec, as illustrated in Figure 4.1. The applied acceleration results in an overall axial strain of about 20 % within 15 sec.

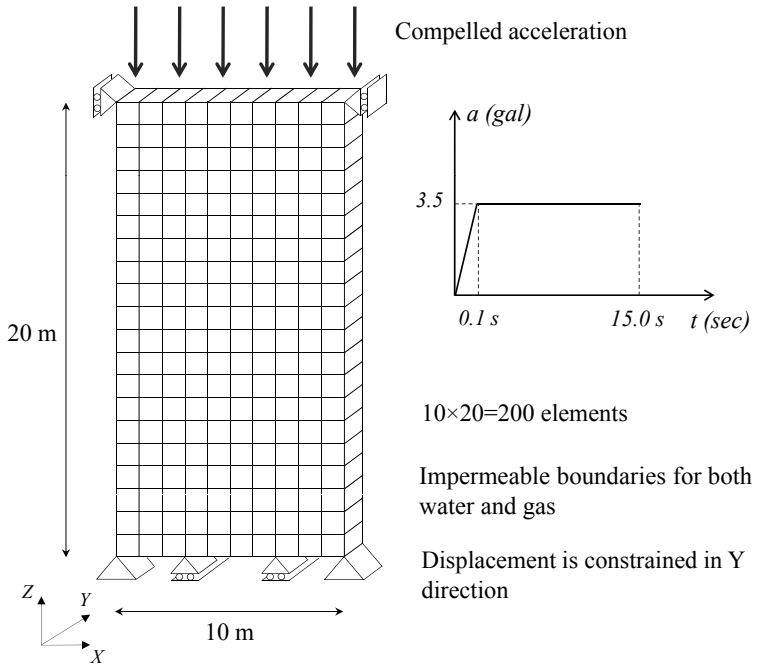

Figure 4.1 Boundary conditions, and applied acceleration profile

4.3 Material Parameters

In this study the material parameters of a clay sample from Torishima, Osaka, Japan are used, and they are listed in Table 4.1. Some of these parameters such as density, swelling index, initial void ratio, and compression index were determined by mechanical laboratory tests. For other parameters, as described in chapter 2, one element simulation were carried out to reproduce the results of laboratory triaxial tests under the boundary and the initial conditions of the tests. In one element simulation, the values for the material parameters are selected in order to provide a good description of the stress-strain relations and stress paths.

According to plastic limit of Torishima clay (PL $\simeq$ 30%) the soil water characteristic curve parameters, α and $n^{'}$, for low plasticity clay were chosen based on Lu and Likos (2004). These curve-fitting parameters and the parameters related to the hydraulic properties of the unsaturated soil are listed in Table 4.2. Using these parameters, the soil-water characteristic curve and the relation between the relative permeability and the degree of saturation for both water and gas phases are shown in Figure 4.2.

Table 4.1 Material parameters of Torishima Clay

Initial void ratio	e_0	1.25
Coefficient of earth pressure at rest	K_0	1.0
Density (t/m^3)	ρ	1.66
Compression index	λ	0.341
Swelling index	κ	0.019
Initial elastic shear modulus (kPa)	G_0	15040
Initial mean skeleton stress (kPa)	$\sigma^{'}_{m0}$	200
Stress ratio at failure in compression	M^*_{mc}	1.24
Viscoplastic parameter	$m^{'}$	24.68
Viscoplastic parameter $(1/s)$	C_1	1.00×10^{-5}
Viscoplastic parameter $(1/s)$	C_2	3.83×10^{-6}
Softening parameter (kPa)	$\sigma^{'}_{mai}$	200
Structural parameter (kPa)	$\sigma^{'}_{maf}$	60
Structural parameter	β	3.6
Hardening parameter	B^*_0	100
Hardening parameter	B^*_1	40
Hardening parameter	C_f	10
Reference value of plastic strain (%)	$\gamma^{vp*}_{(n)r}$	1.25
Strain-dependent modulus parameter	$\alpha^{'}$	10
Hardening parameter	A^*_2	5.9
Hardening parameter	B^*_2	1.8
Suction parameter	S_I	0.50
Suction parameter	s_d	0.25

Table 4.2 Soil-water characteristic curve and hydraulic parameters

Water permeability coefficient at saturated condition (m/s)	k_s^W	5.77×10^{-10}
Gas permeability coefficient at dry condition (m/s)	k_s^G	1.00×10^{-3}
Van Genuchten parameter $(1/kPa)$	α	0.033
Van Genuchten parameter	n	1.083
Minimum saturation	s_{min}	0.00
Maximum saturation	s_{max}	0.99
Shape parameter of water permeability	a	3.0
Shape parameter of gas permeability	b	2.3

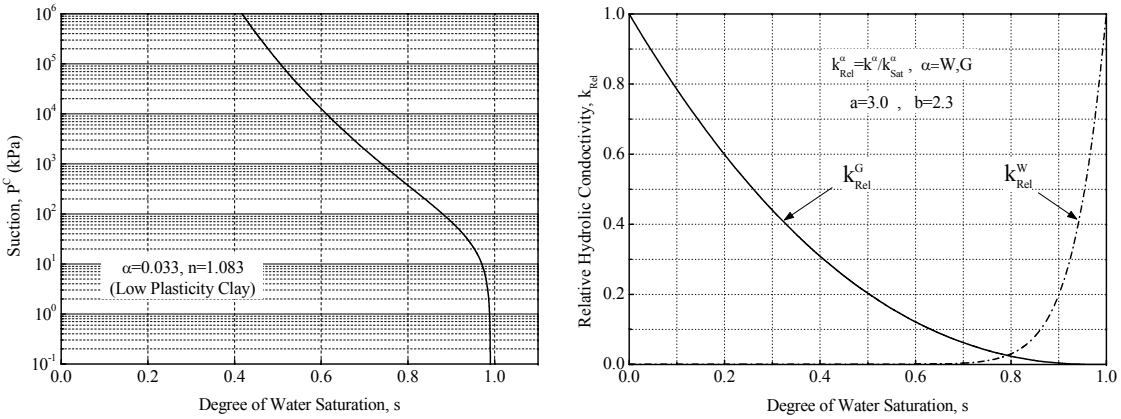

Figure 4.2 Soil-water characteristic curve, and the relative hydraulic conductivity curves used for Torishima clay

4.4 Numerical Parameters

The methods for determining the numerical parameters used in this analysis are described in this section.

4.4.1 Newmark-β Method

The Coefficients of Newmark-β method (γ, β) should be determined so as to make the solution stable. For the linear theory, choosing γ=0.5 and β=0.25 makes the results unconditionally stable regardless of the value of time increment Δt. Therefore, these values generally used in common dynamic analyses. However, in this study we use Newmark-β coefficients derived from the stability analysis of a 1-dimensional u-p formulation. The stability conditions of the analytical scheme in a 1-dimensional u-p formulation are as follows:

$$1 \geq 2\beta \geq \gamma \geq \frac{1}{2} \tag{4.1}$$

$$\Delta t(2\gamma - 1) - \frac{2k}{g} \geq 0 \tag{4.2}$$

$$\gamma \Delta t - \frac{k}{g} \geq 0 \tag{4.3}$$

$$\Delta t(2\beta + 2\gamma^2 - \gamma) + \frac{k}{g}(1 - 2\gamma) \geq 0 \tag{4.4}$$

where Δt is the time increment, k is the permeable coefficient, and g is the gravity acceleration. Using Equations (4.2) to (4.4) the minimum value for γ becomes

$$\gamma \geq \frac{k}{g\Delta t} + \frac{1}{2} \tag{4.5}$$

In this analysis $\beta = 0.3025$ and $\gamma = 0.6$ are used which satisfies both Equarions (4.1) and (4.5).

4.4.2 Rayleigh Damping

The Rayleigh damping expresses the internal damping of soil, which does not include the hysteretic damping through a constitutive model or the radiation damping. This internal damping of soil is not load frequency dependent. Hence factor, the Rayleigh damping coefficients must be chosen in such a way that it provides the minimum variations of

damping over the range of frequencies of input loads. According to this fact, by using modal analysis, these coefficients can be calculated from the following equations, based on the two predominant frequencies in the frequency range of the motion.

$$\alpha_0 = \frac{2\omega_i\omega_j(\omega_i h_j - \omega_j h_i)}{\omega_i^2 - \omega_j^2} \tag{4.6}$$

$$\alpha_1 = \frac{2(\omega_i h_i - \omega_j h_j)}{\omega_i^2 - \omega_j^2} \tag{4.7}$$

where h_i and ω_i are the damping ratio and frequency of the i-th mode, and h_j and ω_j are the damping ratio and frequency of the j-th mode, respectively. Note that the predominant frequencies are the smallest and the largest ones of the eigenvalues in the major frequency range of the motion.

In this numerical analysis, α_0=0 and α_1=0.01 are considered. Also, for controlling the fluctuation in the response acceleration time histories, the Rayleigh damping which depends on the initial stiffness is used.

4.4.3 Time Increment

In this study time integration of the finite element equations is accomplished by tangent stiffness method. This method results in more stability for time steps much larger than that can be employed with the explicit methods like Euler method. When explicit time stepping algorithm is used for the numerical solution, the Courant-Friedrichs-Lewy condition (CFL condition) must be satisfied for convergence. In tangent stiffness method, the CFL number restriction can also be satisfied for more accurate solution, but it will be less strict than that in the explicit case.

Based on CFL condition, if a wave is crossing a mesh, the time increment must be less than the time for the wave to travel adjacent grid points. In other words, wave should not move through more than one element (the distance between two adjacent nodes) in each step. This leads us to the CFL time step restriction of

$$\Delta t \leq \frac{h_{min}}{c_{max}} \tag{4.8}$$

where c_{max} is the maximum wave speed, and h_{min} is the minimum side length of the element. In the current study, having the 20-node hexahedron element with side length l_1, l_2, l_3, and being the longitudinal wave velocity V_p as the maximum wave speed, the

critical time step becomes

$$\Delta t \leq \frac{1}{V_p} min[\frac{l_1}{2}, \frac{l_2}{2}, \frac{l_3}{2}] \quad , \qquad v_p = \sqrt{\frac{E}{\rho}} \tag{4.9}$$

The next criterion for time increment is from the instability of Newmark-β method. In Equations (4.2) to (4.4), Equation (4.2) gives the lower limit for Δt

$$\Delta t \geq \frac{2k}{g(2\gamma - 1)} \tag{4.10}$$

Using $\gamma = 0.6$ and $g = 9.8m/s^2$, this inequality approximatly becomes $\Delta t \geq k$. Based on these two time step constraints, $\Delta t = 0.001sec$ is selected for the analysis.

4.5 Numerical Results for Fully Saturated and Partially Saturated Clay

In this section, the numerical simulation results are presented to illustrate the progress of shear strain localization in both saturated and partially saturated clay. Also, the results of saturated and unsaturated analyses are compared at various strain levels. Table 4.3 shows the initial pore pressures considered for this analysis. Note that the initial gas (air) pressure is assumed as a small value to make the condition similar to the ones exist in many geotechnical problems.

Figure 4.3 shows the distributions of accumulated viscoplastic shear strain γ^{vp} at overall axial strains of 5%, 10%, 15%, and 20%. γ^{vp} is defined as follows

$$\gamma^{vp} = \int d\gamma^{vp} \quad , \quad d\gamma^{vp} = (de_{ij}^{vp} de_{ij}^{vp})^{\frac{1}{2}} \tag{4.11}$$

where de_{ij}^{vp} is the viscoplastic deviatoric strain-increment tensor. In this Figure it is seen that the shear bands start to develop from the trigger points at the corners of the specimen, then they continue to propagate towards the center of the opposing walls, and

Table 4.3 Initial pore pressures for the strain localization analysis

	$P^W(kPa)$	$P^G(kPa)$	$P^C(kPa)$	$s(\%)$
Unsaturated case	-1240	20	1260	72
Saturated case	100	—	0.0	100

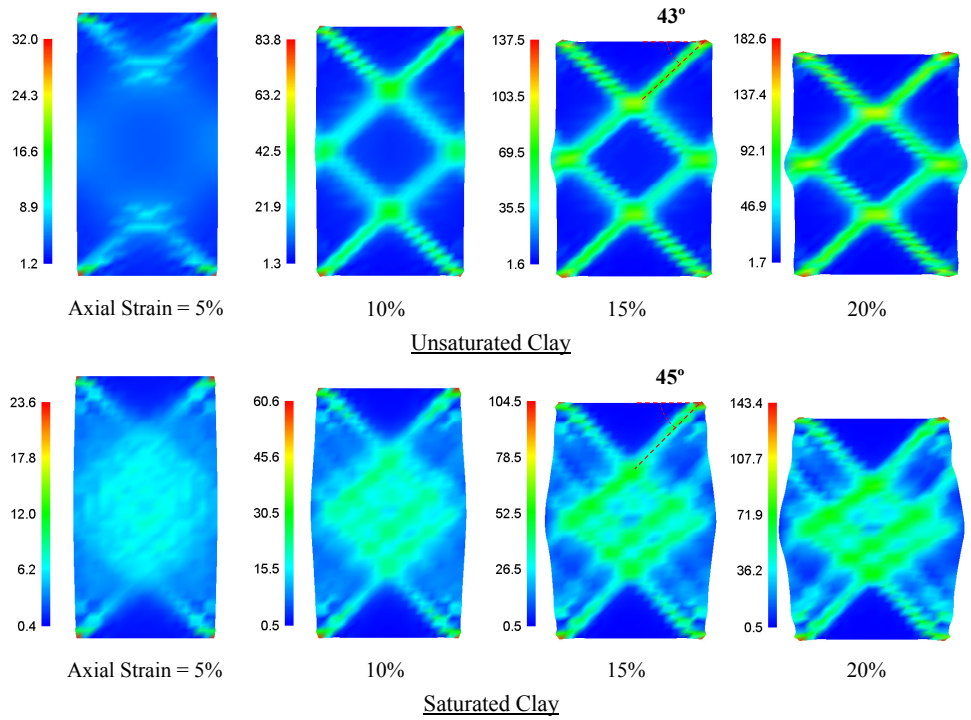

Figure 4.3 Distributions of accumulated viscoplastic shear strain for unsaturated and saturated clays; Unit(%)

eventually they narrow to four symmetric distinct bands by increasing the compelled displacement. The similar patterns of shear bands are observed in both saturated and unsaturated cases. However, the thickness of the zone of the localized shear strain is narrower in unsaturated case than that in saturated case. In addition, in unsaturated case much clearer shear bands are seen, and the difference between the maximum and the minimum values of γ^{vp} is larger. This suggests that the strain localizes prominently when the soil is unsaturated. This pattern is, also, observed in the distribution of the axial strain (see Figure 4.4).

Larger accumulated shear strain in a material can be interpreted as more instability in that material. Following this point of view, the unsaturated clay is more unstable than the saturated one.

For saturated clay, Oka et al. (1995) demonstrated that by using the viscoplastic model, the preferred orientation of shear bands is 45 degrees under plane strain locally undrained condition, i.e., k=0. In the present analysis, the coefficient of permeability is very small, and the load is applied in a very short time duration. This makes the condition very similar to locally undrained condition. That is the reason why the inclination angle

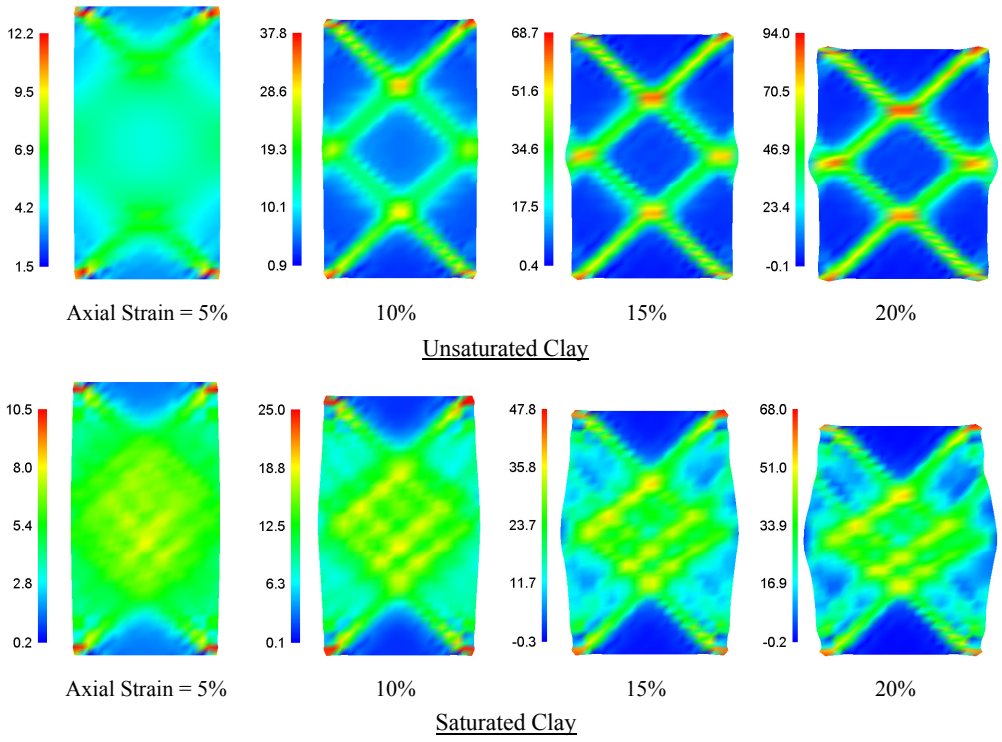

Figure 4.4 Distributions of axial strain ε_z for unsaturated and saturated clay; Unit(%)

of shear bands obtained in this analysis becomes 45 degrees in saturated case. However, this angle is smaller (almost 43 degrees) in unsaturated case.

Figure 4.5 depicts the distributions of total volumetric strain ε_v which is defined as

$$\varepsilon_v = \int D_{kk} dt \tag{4.12}$$

Oka et al. (1994a) observed that in undrained triaxial compression tests for fully saturated normally consolidated clay, water contents along shear bands are lower than those outside the shear bands, namely, contraction occurs inside the shear bands. But, from Figure 4.5 it is seen that the volumetric strain in the saturated clay is almost zero in the whole specimen since water does not have enough time to move through pores due to the very low permeability of the clay, and very short load duration (15 sec). According to assumption of incompressibility of water and soil particles, in saturated case volume changes equal to zero is completely logical.

In case of unsaturated clay, the volume contraction occurs in the whole specimen, which it is more intense inside the shear bands. Note that in this case the gas phase can compress, which lets more volume changes occur in the specimen.

Figure 4.6 shows the deformed meshes at several strain levels. In small levels of overall

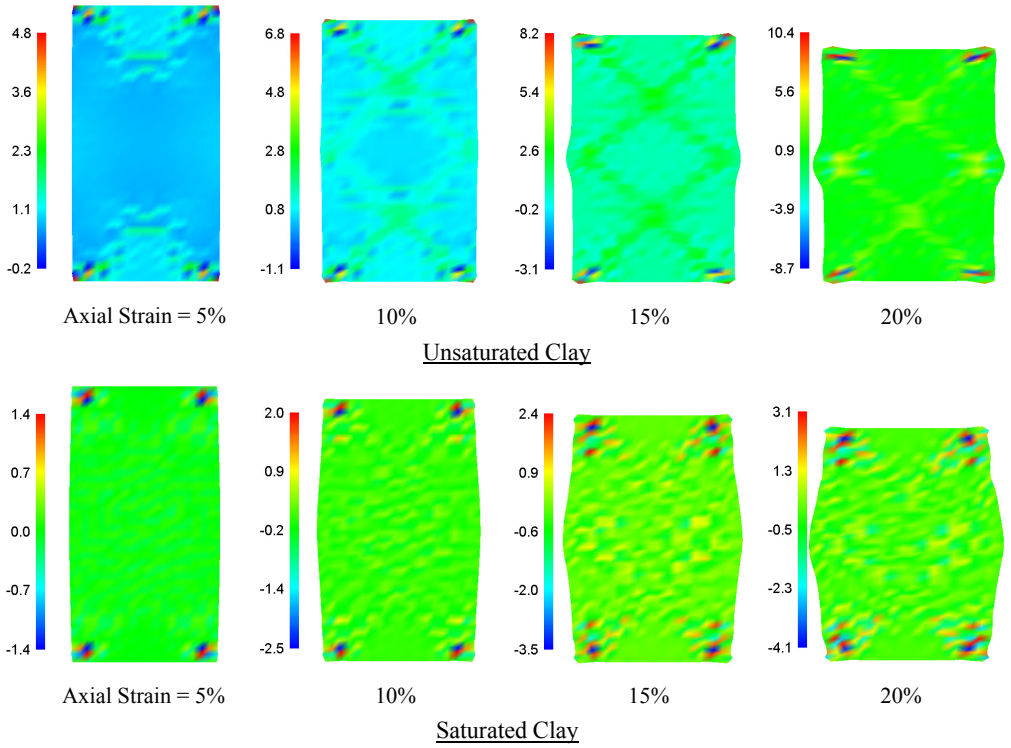

Figure 4.5 Distributions of the volumetric strain for unsaturated and saturated clays; Unit(%)

axial strain (ranging from 0 to 5 %) homogenous deformations are observed. However, at higher axial strains clear shear bands form. This concentrated shearing deformation is more intense in unsaturated case than in saturated case. It is, also, seen that deformation is symmetrical in both cases. In saturated case since the mixture is incompressible, the width of the specimen becomes larger comparing to unsaturated case, and the specimen takes the barrel shape.

The distributions of the mean skeleton stress at different levels of overall strain are displayed in Figure 4.7. It can be seen that in unsaturated case at the lower levels of axial strain (around the axial strain of 5% or less) the mean skeleton stress increases through the whole specimen during compression loading. But, after the appearance of shear bands, the mean skeleton stress starts to decrease along the shear bands by progress of the axial displacement. Outside the shear bands, however, the mean skeleton stress continues to increase.

In saturated clay, the distributions of the mean skeleton stress are, also, affected by the formation of the shear bands. In contrast with unsaturated case, in saturated clay the mean skeleton stress starts to decrease from the initial stages of loading. This decrease is greater inside the shear bands than the other parts of the specimen.

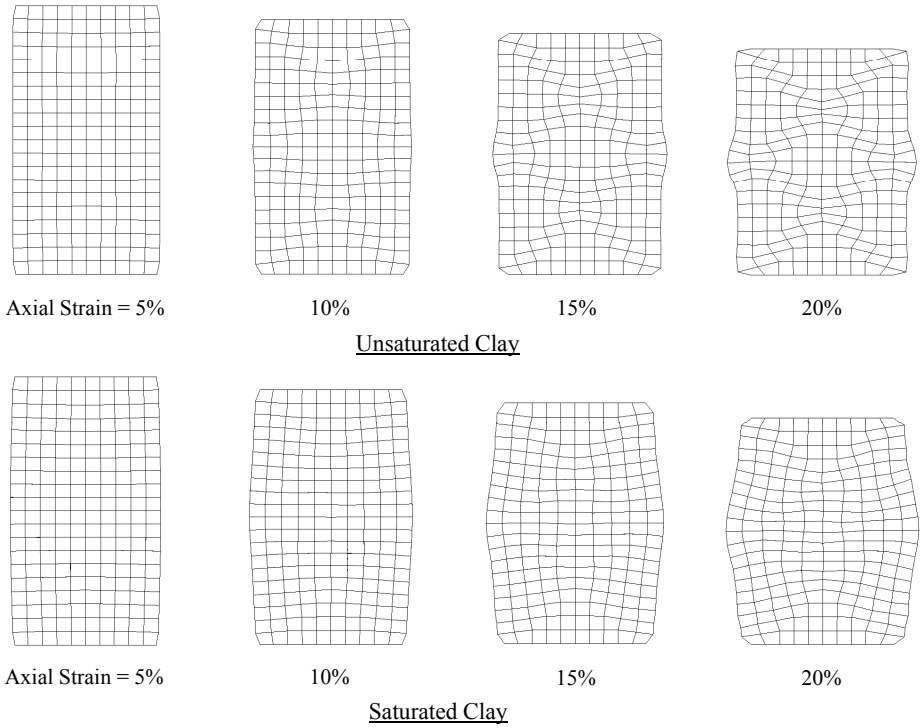

Figure 4.6 Deformed meshes of the specimen at various strain levels for unsaturated and saturated clays

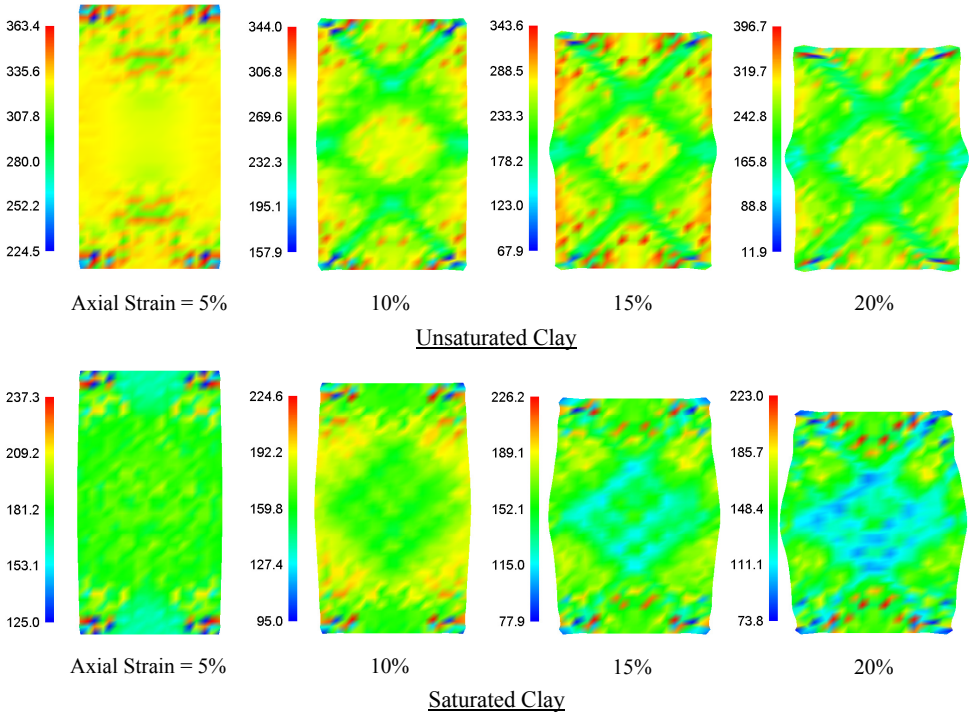

Figure 4.7 Distributions of the mean skeleton stress for unsaturated and saturated clays; Unit(kPa); $\sigma_{m0}^{'} = 200$ kPa

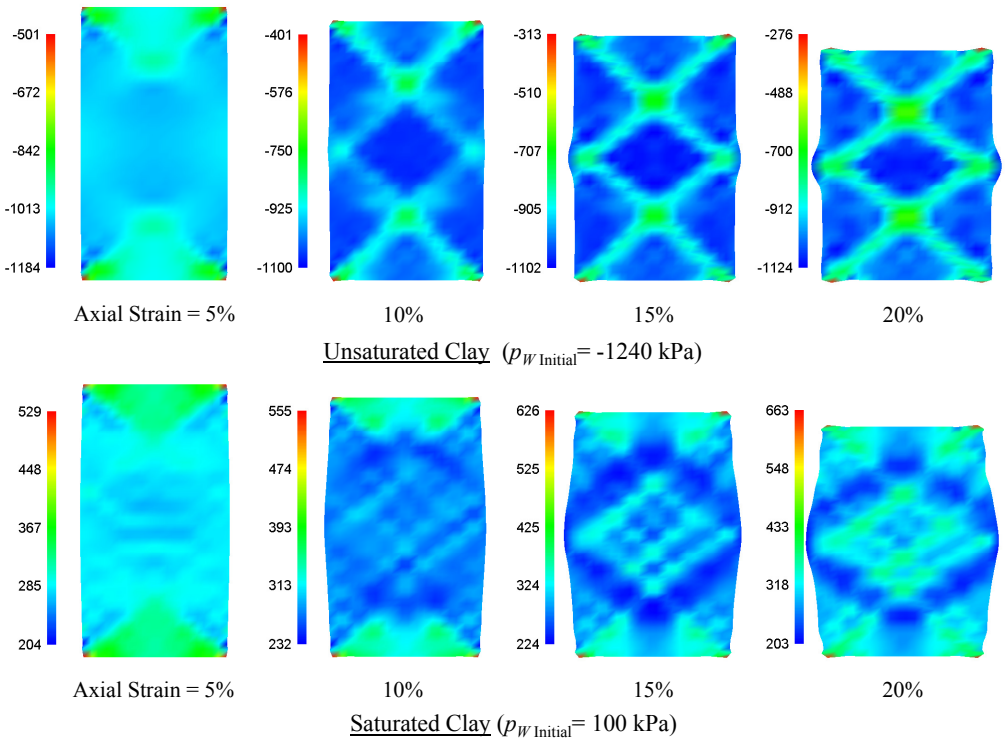

Figure 4.8 Distributions of the pore water pressure for unsaturated and saturated clays; Unit(kPa)

In Figure 4.8 the distributions of pore water pressure are shown. The negative pore water pressure of unsaturated soils indicates a meniscus with a suction force that behaves as a capillary force between the soil particles. In partially saturated case, it is observed that pore water pressure starts to increase in the entire specimen. This development is strongly affected by the formation of the shear bands, which makes the pore water pressure distribution inhomogeneous. It is seen that pore water pressure increases dramatically inside the shear bands which can be interpreted as collapse of the water meniscus which is caused by shearing.

In saturated clay the pore water pressure distributions have the same patterns as those for unsaturated clay. Comparing the two cases, the pore water pressure is more localized in the case of unsaturated clay.

The distributions of pore gas (air) pressure in unsaturated clay, which is shown in Figure 4.9, indicate the same tendency as those of the pore water pressure. It is possible to see that the pore gas pressure increases by progress of axial displacement. This increase is larger along the shear bands than the rest of the specimen. The magnitude of the calculated excess pore gas pressure is relatively small compared to the changes in pore water pressure, but it is reasonably simulated by the analysis method.

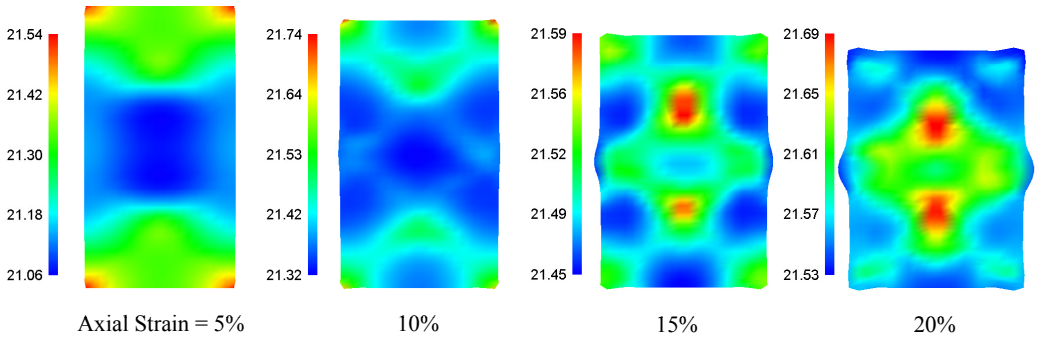

Figure 4.9 Distributions of the pore gas pressure for unsaturated clay; Unit(kPa); $P_i^G = 20$ kPa

As a result of contraction inside the shear bands in normally consolidated or lightly over consolidated clay subjected to triaxial compression loading, the degree of saturation increases and consequently suction drops along the shear bands. This behavior can be observed in Figure 4.10. In this figure the degree of saturation contours and the suction contours are shown at different levels of overall axial strain. The decrease of suction can especially be dangerous in loose soils where the suction force provides the stability of the soil particles. It is important to note that even though suction in general improves the soil mechanical properties, i.e. increasing stiffness and shear strength, the hypothesis of saturated material, which is widly used in the analysis of geotechnical problems, is not at all for safety's sake since the partially saturated soil can experience collapse of suction which causes a drastic loss in strength.

Figure 4.11 displays the relative velocity vectors of soil particles with respect to the center of the specimen in both saturated and unsaturated clay. As seen in this figure, the shear bands separate the specimen into seven distinct block like portions. Each of these block like portions has its own individual velocity direction which does not change by time. These blocks are depicted schematically in Figure 4.12.

The stress strain relations for both fully saturated and partially saturated clay are shown in Figure 4.13. It is observed that the peak deviator stress in partially saturated case is higher than that in saturated case. In general, partially saturated soils can show higher peak strength than air-dried and fully saturated soils due to the suction (capillary) force among the soil particles. Comparing the overall axial strains at the peak strengths in the two cases, it is seen that the unsaturated clay reaches the peak strength in smaller value of overall strain.

After reaching the peak strength, the deviator stress falls abruptly as the overall strain

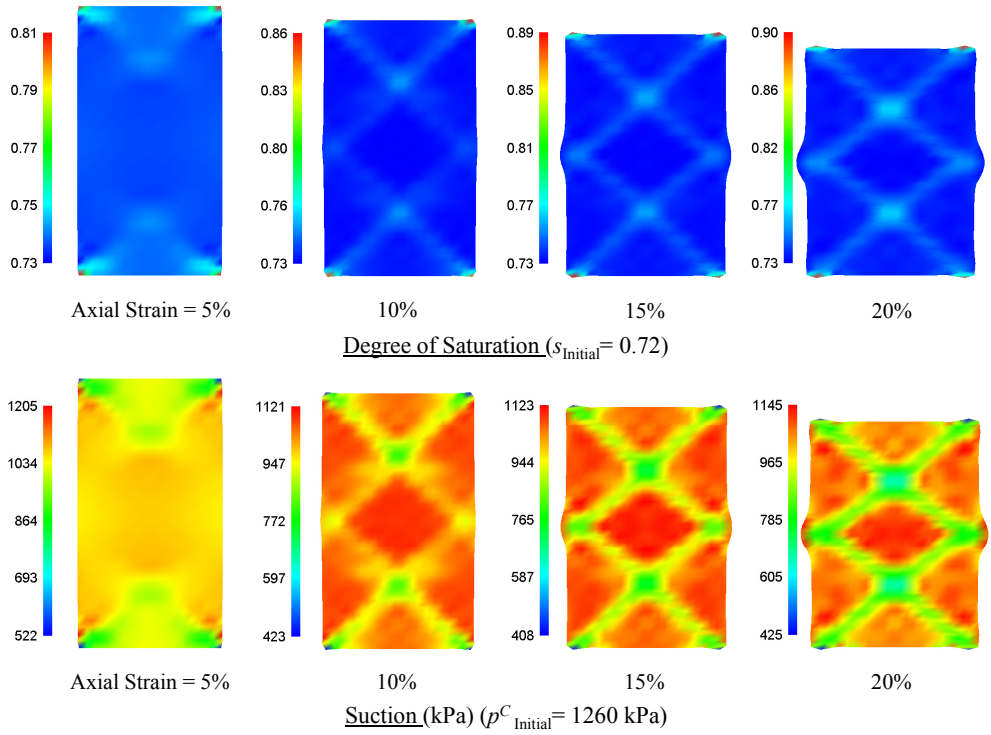

Figure 4.10 Distributions of degree of saturation and suction for unsaturated clay

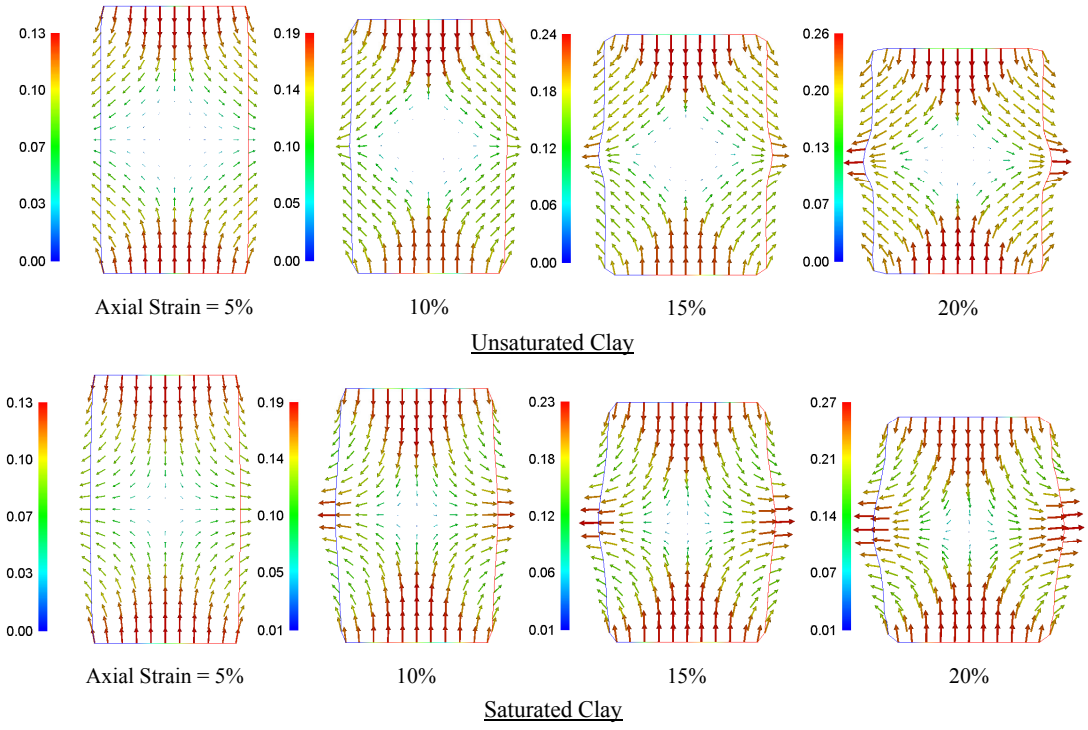

Figure 4.11 Distributions of relative velocity vector for unsaturated and saturated clays; Unit(m/s)

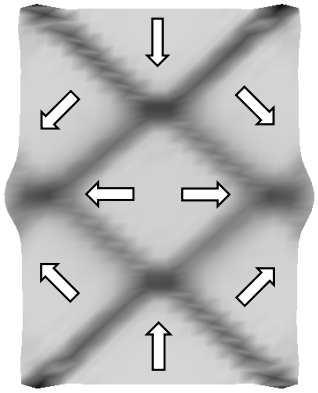

Figure 4.12 Schematic figure of solid velocity field

increases. This strain softening behavior, i.e. brittleness, controls the progressive failure and post-failure phenomena. From Figure 4.13 it is seen that the partially saturated clay exhibits more brittle failure than fully saturated clay. It is due to the drastic loss of the suction force along the shear bands in the partially saturated case.

Passing the peak stress level, the strength of the soil reaches a reasonably stable value after large deformations along the shear bands, i.e. residual strength. Higo et al. (2011) experimentally showed that the residual stress levels are almost the same for partially saturated sand, air-dried sand, and fully saturated sand. Furthermore, Cunningham (2003) observed that in unsaturated silty clay under constant-suction condition the post-rupture failure envelope is independent of the suction applied to the sample. Note that the post-rupture strength which takes place just after the peak must be clearly distinguished from the residual strength which requires much larger relative displacements to develop. However, in the present results it is seen that both the post-rupture strength and the residual strength for the partially saturated clay is higher than those for saturated clay. The reason can be that even though the suction drops dramatically along the shear bands, there is still large value of suction force inside the shear bands due to the high level of the initial suction.

Figures 4.15 and 4.16 show local stress-strain relations and stress paths at different points inside and outside the shear bands for the unsaturated clay. The positions of these points are marked in Figure 4.14. The results indicate that more brittleness occurs inside the shear bands than outside of them.

Burland (1990) demonstrated that in unconsolidated undrained triaxial tests on clay, localization essentially coincides with peak strength. As shown in Figure 4.17, the present

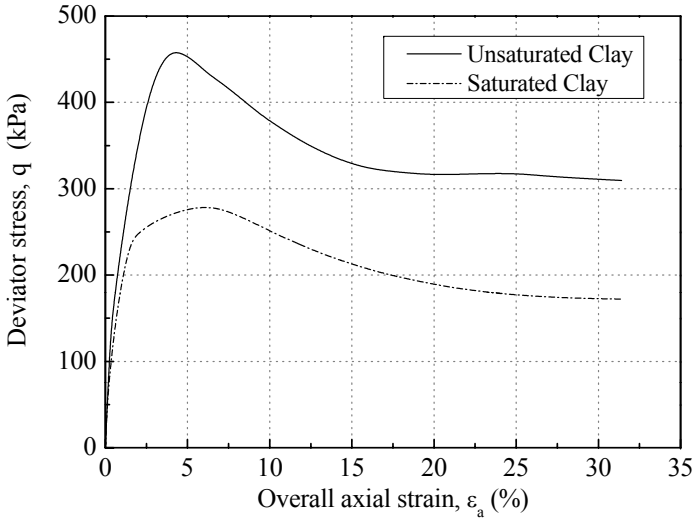

Figure 4.13 Stress-strain relations for unsaturated and saturated clay

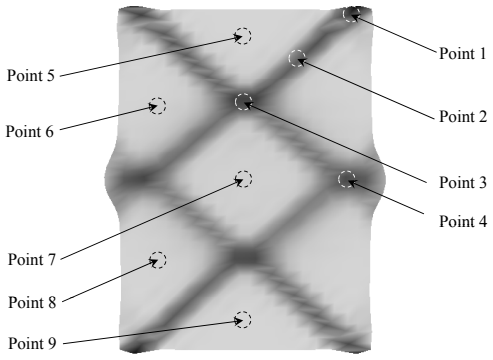

Figure 4.14 Local points inside and outside the shearbands

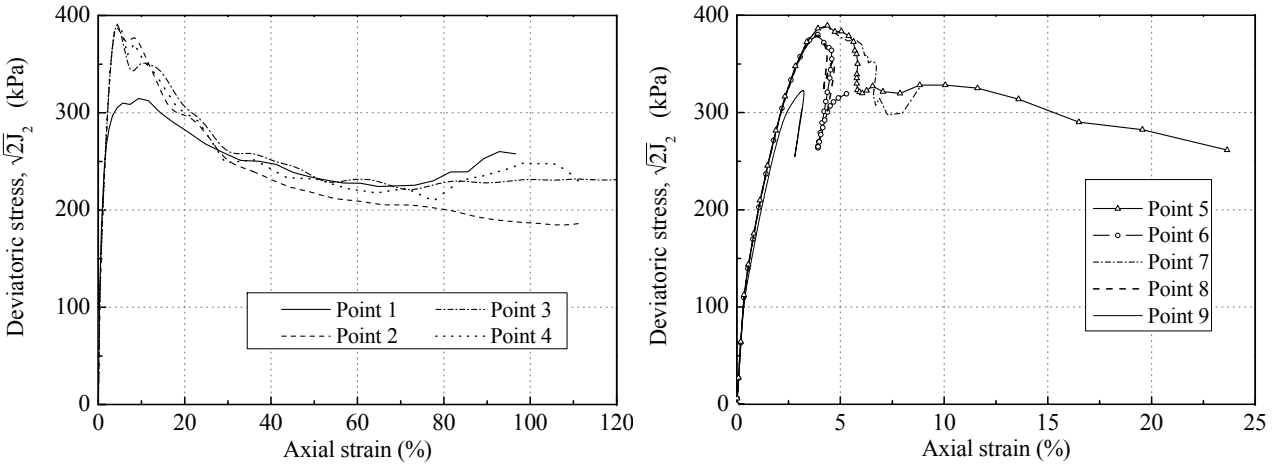

Figure 4.15 Local stress-strain relations inside and outside the shear bands for unsaturated clay

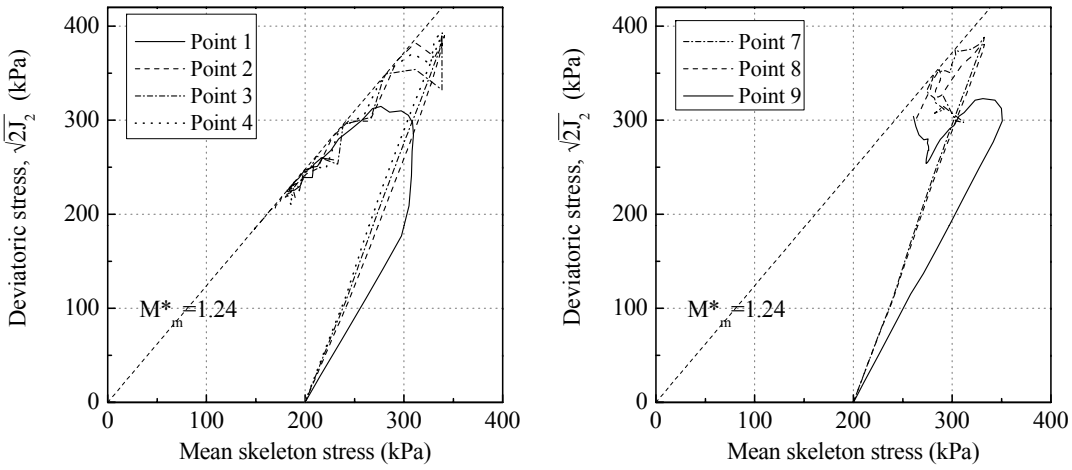

Figure 4.16 Local stress paths inside and outside the shear bands for unsaturated clay

results are consistent with Burland studies. This figure shows the distributions of the accumulated viscoplastic shear strain just before the peak strength ($\varepsilon_a = 3.1\%$), at the peak ($\varepsilon_a = 4.2\%$), and immediately after the peak strength ($\varepsilon_a = 5.5\%$). It is observed that the shear bands start to appear at the same time as the strength reaches its peak value.

Cunningham (2003) observed that during the triaxial test, unsaturated silty clay contracted but that, once peak strength reached, further volume change ceased abruptly. The same behavior is seen in the volumetric strain-overall axial strain relations obtained in the present study. Figure 4.18 shows the changes in volumetric strain of each block like portions. It is seen that the volumetric strain increases until the axial strain reaches the value in that the peak strength takes place ($\varepsilon_a = 4.2\%$), but it almost stays constant afterward. This indicates that after the peak strength, further straining results from rigid block sliding along the shear bands, not the volume change.

4.6 Mesh-Size Dependency

In order to evaluate the mesh-size sensitivity of the numerical results, three extra square mesh patterns are considered besides the defaults mesh pattern for the localization analyses. The pattern of 5×10 (50 elements) is considered as the coarser mesh, and 20×40 (800 elements) and 25×50 (1250 elements) are assumed as the finer meshes, as illustrated in Figure 4.19. The deformed mesh and the distribution of the accumulated viscoplastic shear strain for these four cases are depicted in Figures 4.20 and 4.21 at the overall axial

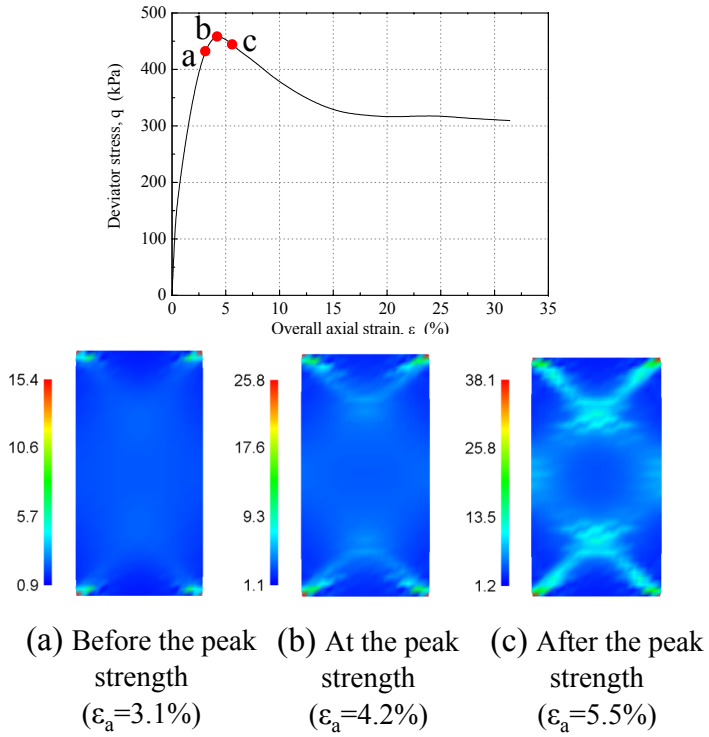

Figure 4.17 Distributions of accumulated viscoplastic shear strain just before the peak strength, at the peak, and immediately after the peak for unsaturated clay; Unit(%)

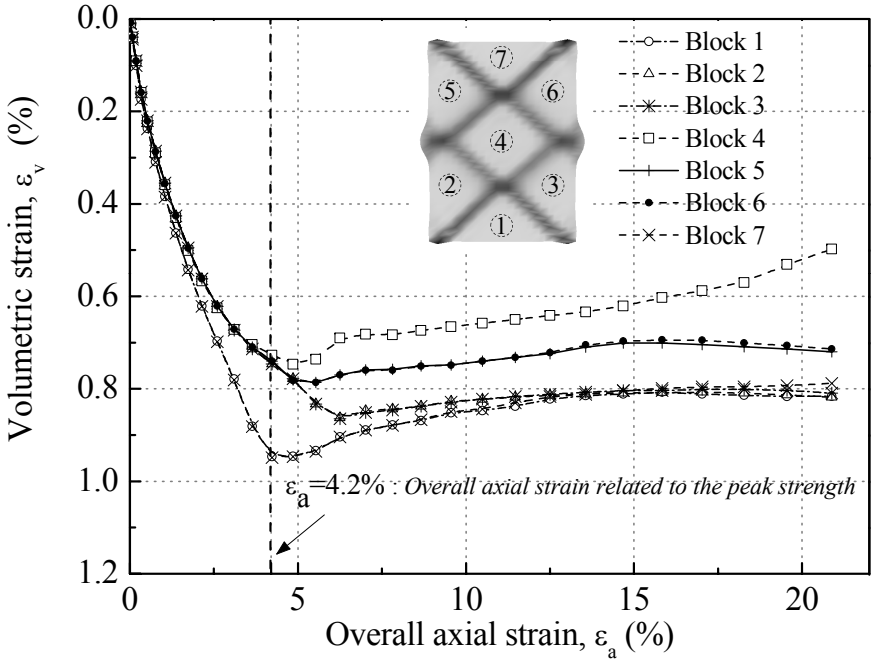

Figure 4.18 Local volumetric strain-overall axial strain relation for unsaturated clay

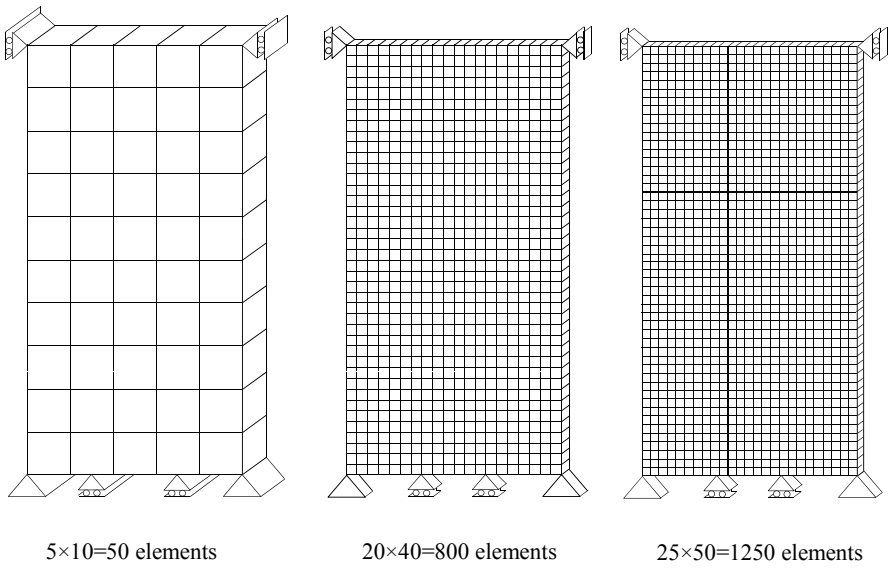

Figure 4.19 Additional mesh patterns to study mesh-size dependency

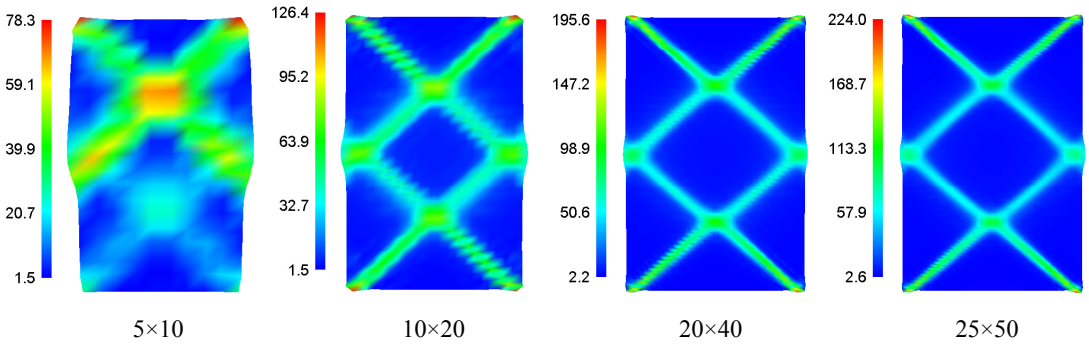

Figure 4.20 Distributions of accumulated viscoplastic shear strain for different mesh patterns; Unit(%); Initial saturation $s_i = 72\%$, at overall axial strain ε_a of 13.5%

strain of 13.5%. Taking the finer mesh size leads to a higher level of strain localization, and narrows the width of the shear band since the shear bands span across the smaller elements. In the finer meshes, i.e., 800 elements and 1250 elements patterns, the shear banding is observed in the same shape and angle as for 200 elements pattern, emanating from the corners of the specimen and finally localizing into four diagonal bands. In the case with 50 elements, however, the strain is localized into two wider bands, of which a high level of localized strain is observed in the center of them.

The stress-strain relations for these four cases are compared in Figure 4.22, where the deviator stress is plotted versus the overall axial strain. All the cases demonstrate rather similar tendency in stress-strain relations, although slight differences are observed

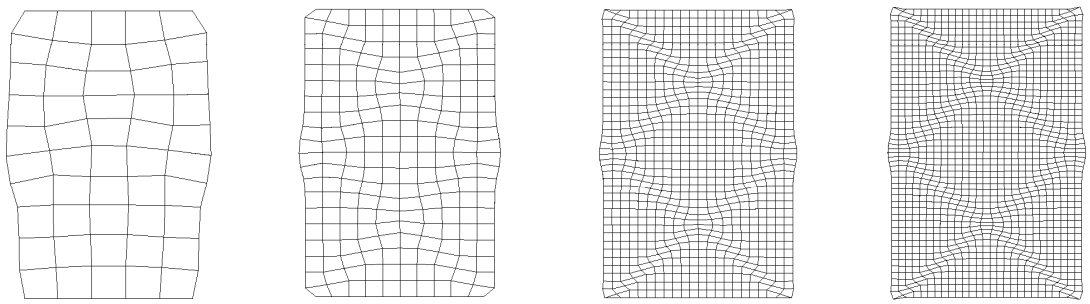

Figure 4.21 Deformed meshes for different mesh patterns; $s_i = 72\%$, $\varepsilon_a = 13.5\%$

among stresses during softening after the peak stress point. In the coarser mesh pattern, the deviator stresses after the peak point tend to decrease more rapidly in comparison with those in the finer meshes. Nonetheless, the results appear to be convergent by mesh refinement after 200 elements, in view of the fact that the differences become smaller between the stresses in 200 elements case and 800 elements case, and also the stresses in 800 elements case and 1250 elements case are nearly the same.

It has been shown by many researchers that the consideration of material rate dependence substantially eliminates the pathological mesh sensitivity under quasi-static and/or dynamic loading conditions (e.g., Needleman 1988, Loret and Prévost 1991, etc.). However, the mesh-size dependency is somewhat observed in simulation results like any other finite element analyses. For the stress-strain relations of clay under quasi-static loading, Oka et al. (1995) have reported a slightly more softening response in a finer mesh configuration. In the latter work by Oka et al. (2002), the mesh size effects were found to be insignificant on the stress-strain relations, whereas all the cases with different mesh configurations have shown identical values. In the present study, however, a slightly more hardening behavior is observed by taking a finer mesh configuration under dynamic loading conditions. Since the constitutive model and loading conditions are different from the preceding works, this behavior might be explained. Moreover, deformation mechanism of the specimen caused by the material parameters under the current state of dynamic loadings, as well as the applied boundary conditions and constrained trigger points at the corners, might account for in this regard. The aspect ratio of the specimen, also, has a significant influence on the stress-strain behaviors in the 3D analysis of dynamic shear banding, as pointed out by Zbib and Jubran (1992). Accordingly, further studies have to be carried out to evaluate the effect of above-mentioned reasons on the dynamic strain

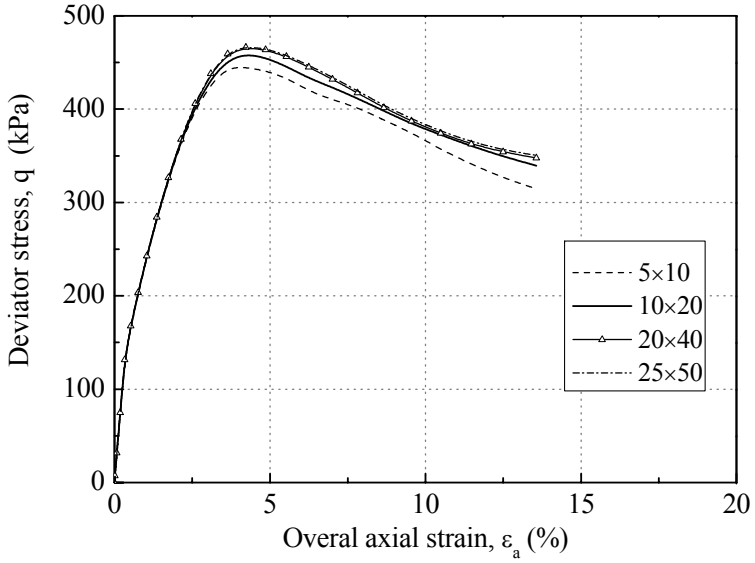

Figure 4.22 Stress-strain relations for different mesh patterns

localization of clays.

Despite the slight differences in stress-strain relations for different mesh configurations, convergency of the results verifies the suitability of current analysis at an acceptable level of mesh-size dependency. In addition, considering the overall shape of the shear bands and the stress-strain relations, the case with 200 elements gives results consistent with the finer meshes in a significantly shorter computation time, which implies adequacy of the 200 elements pattern to resolve the localization phenomenon for clay under dynamic loading conditions.

4.7 Effect of Acceleration

Strain rate sensitivity is an important characteristic of soil in both saturated and unsaturated cases. In particular, it is well known that a unique stress-strain curve exists for each different strain rate in clayey soil. Under dynamic loading, this rate-dependent behavior of the soil is a key factor to the strength of the soil. However, in very high strain rates it is too difficult to study the effects of the rate on strain localization in partially saturated soil, and to determine the peak and residual strengths of the soil, experimentally. Hence, it is necessary to investigate the rate-dependent behavior of unsaturated soils subjected to dynamic loads, numerically.

Figures 4.23, 4.24 respectively show the deformed meshes and the distributions of

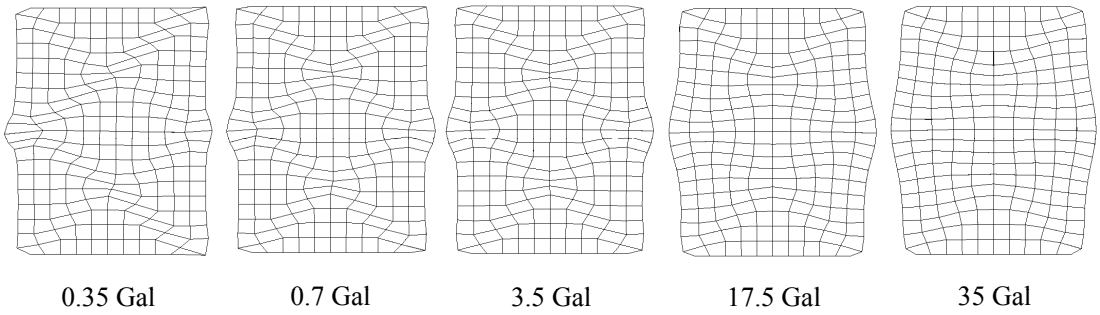

Figure 4.23 Deformed meshes with different accelerations; $s_i = 72\%$, $\varepsilon_a = 20\%$

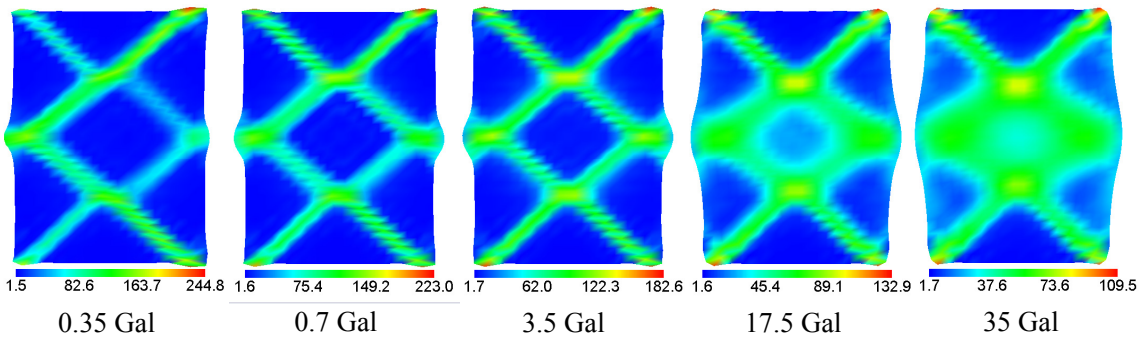

Figure 4.24 Distributions of accumulated viscoplastic shear strain with different accelerations; Unit(%); $s_i = 72\%$, $\varepsilon_a = 20\%$

accumulated viscoplastic shear strain in the specimen subjected to various uniform axial compressive accelerations of 0.35, 0.7, 3.5, 17.5,and 35 gal at the axial strain of 20%. The applied acceleration rises from zero to the maximum value within 0.1 sec, and it remains constant afterward until the end of loading time. It can be seen that the lower acceleration leads to the higher level of shear strain localization; moreover, it is observed that under the lowest acceleration the formation of the shear bands is not symmetric, and two of the shear bands become dominant.

From the distributions of suction shown in Figure 4.25 it can be observed that the reduction in the value of suction is larger when the higher level of acceleration is applied. However, using different accelerations, the differences in the suction results are not significant, which can be assumed that changes in suction are not the function of the applied acceleration.

In Figure 4.27 the distributions of the mean skeleton stress at an overall axial strain

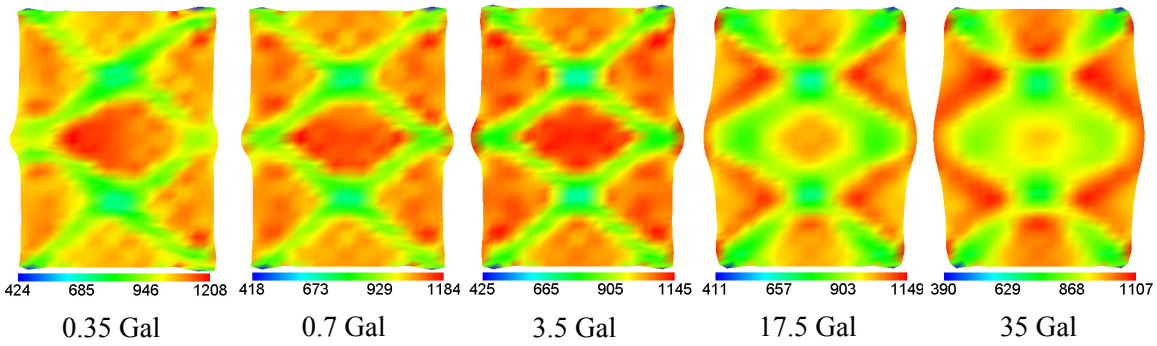

Figure 4.25 Distributions of suction with different accelerations; Unit(kPa); Initial suction $P_i^C = 1260$ kPa, $\varepsilon_a = 20\%$

of 20% are shown. It is possible to see that the higher acceleration, the more reduction of the mean skeleton stress inside the shear bands. The pore pressure contours are displayed in Figure 4.26. When the maximum acceleration increases, higher levels of excess pore pressure in both water and gas phases are generated.

Oka (2003) experimentally studied the effect of strain rate on the stress-strain relations of fully saturated clay by performing undrained triaxial compression tests. Using constant strain rates, they observed that the deviator stress levels obtained from the tests with higher strain rates were larger than those from the tests with a constant lower strain rate. The same tendency was seen by Yong et al. (1969) in the stress-strain response of clay in dynamic compression. They showed that under dynamic loads, increasing strain rates produced greater peak values. The same trend of the rate effect is seen in the results obtained in the present study. Figure 4.28 indicates the stress-strain relations for partially saturated clay subjected to dynamic loads with different acceleration. It is possible to observe that the peak and residual strengths with higher acceleration are larger than those with the lower acceleration. It is, also, seen that with lower accelerations, the soil reaches the residual strength at the smaller values of overall axial strain.

4.8 Effect of Confining Pressure

In this section, simulations are carried out to investigate the behavior of unsaturated clay under three different levels of confining pressure. From the deformed meshes and the accumulated viscoplastic shear strain contours shown in Figures 4.29 and 4.30 respectively, it is possible to see that applying higher confining pressure leads to the higher level of shearing deformation, and consequently the higher level of localization. In the higher

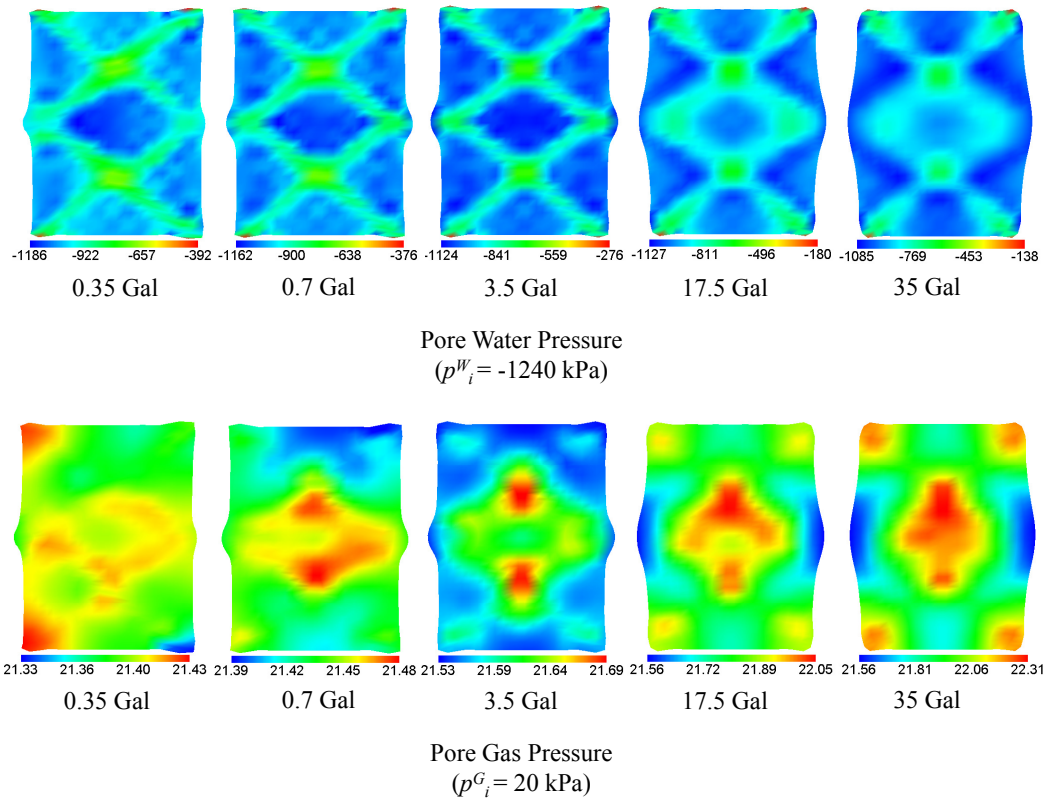

Figure 4.26 Distributions of pore pressures with different accelerations; Unit(kPa); $s_i = 72\%$, $\varepsilon_a = 20\%$

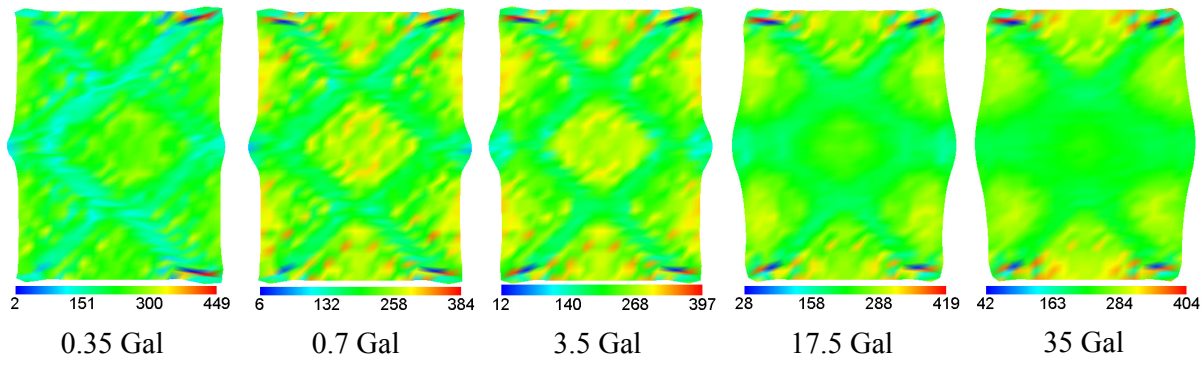

Figure 4.27 Distributions of the mean skeleton stress with different accelerations; Unit(kPa); $s_i = 72\%$, $\varepsilon_a = 20\%$, $\sigma'_{m0} = 200$ kPa

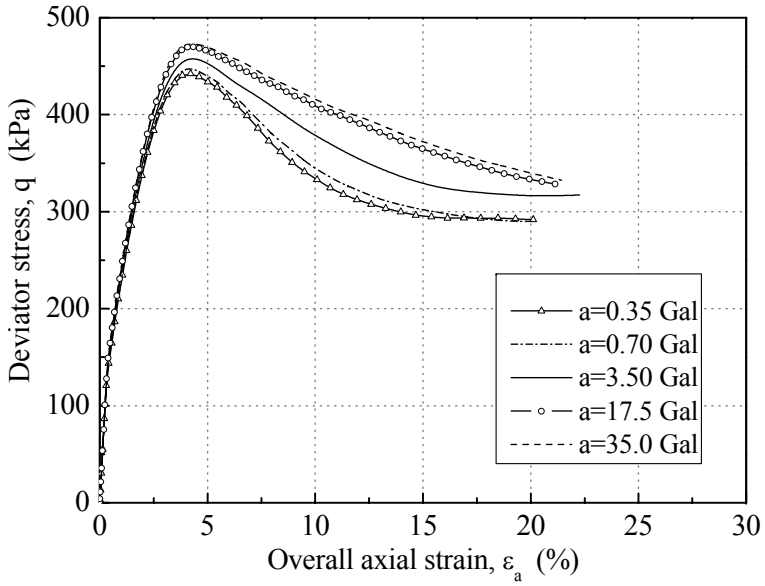

Figure 4.28 Stress-strain relations with different accelerations

confining pressures, i.e. 200kPa and 300kPa, the same pattern of shear banding with the same inclination angle are observed. However, for the case with confining pressure of 100kPa the shear strain is localized into two wider bands across the specimen, of which a high level of localized strain is seen in the center of the specimen.

For the volumetric strain, as shown in Figures 4.31, the larger volumetric contraction is observed for the higher confining pressure at the same axial strain. The similar behavior of volumetric strain was reported by Oka et al. (2010) for unsaturated compacted silt under the same boundary conditions as used in the present study. Higher levels of contraction in the specimen lead to the higher degrees of saturation, and consequently the larger drop

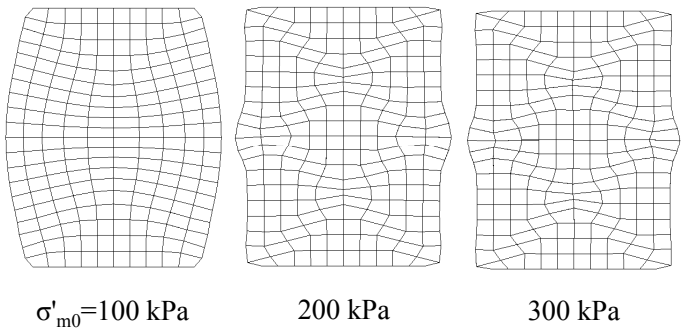

Figure 4.29 Deformed meshes with different initial confining pressures; $s_i = 72\%$, $\varepsilon_a = 20\%$

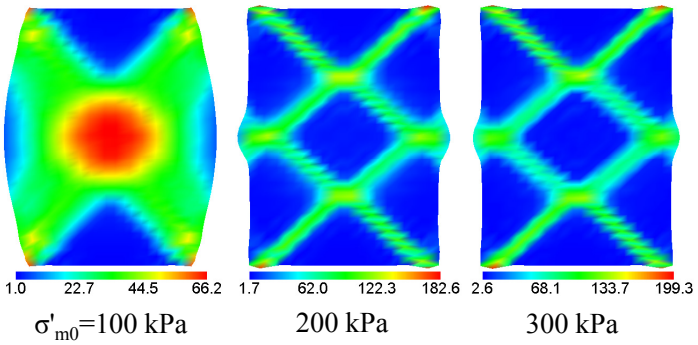

Figure 4.30 Distributions of accumulated viscoplastic shear strain with different initial confining pressures; Unit(%); $s_i = 72\%$, $\varepsilon_a = 20\%$

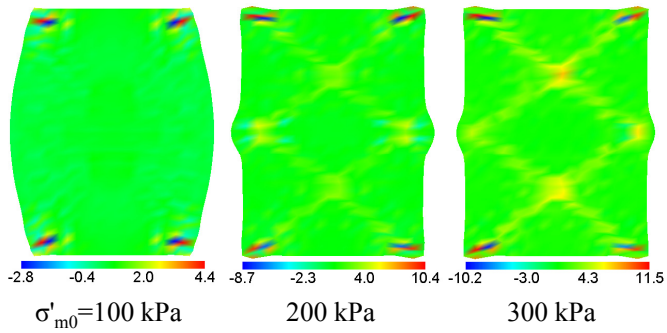

Figure 4.31 Distributions of volumetric strain with different initial confining pressures; Unit(%); $s_i = 72\%$, $\varepsilon_a = 20\%$

in suction. Therefore, as shown in Figures 4.32 and 4.33, the magnitude of increase in saturation and decrease in suction is larger for the higher levels of confining pressure.

Figure 4.34 displays the distributions of the mean skeleton stress. It can be seen that the higher level of confining pressure, the more reduction of the mean skeleton stress inside the shear bands. In Figure 4.35 the pore pressure contours are shown. When the level of confining pressure is higher, the pore pressure is more localized.

The stress-strain relations, shown in Figure 4.36, indicate that the peak and the residual strengths increase with a corresponding increase in confining pressure.

4.9 Effect of Initial Suction

The level of suction has a significant influence on the behavior of unsaturated soils. It has a direct effect on the stress variables, the soil water characteristic curve, the hydraulic

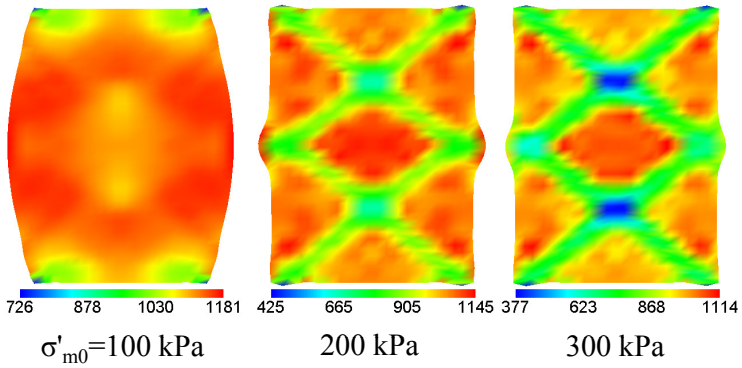

Figure 4.32 Distributions of suction with different initial confining pressures; Unit(kPa); Initial suction $P_i^C = 1260$ kPa, $\varepsilon_a = 20\%$

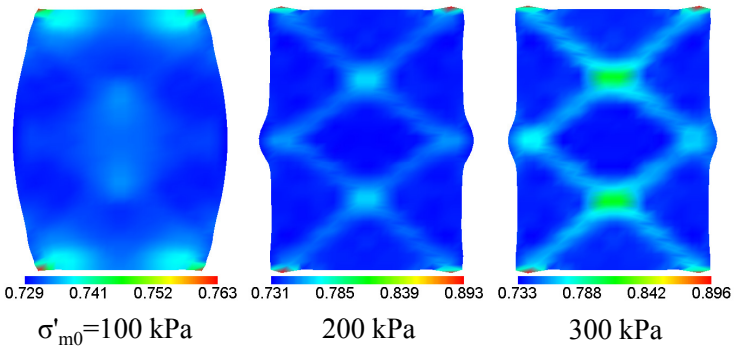

Figure 4.33 Distributions of saturation with different initial confining pressures; Initial saturation $s_i = 72\%$, $\varepsilon_a = 20\%$

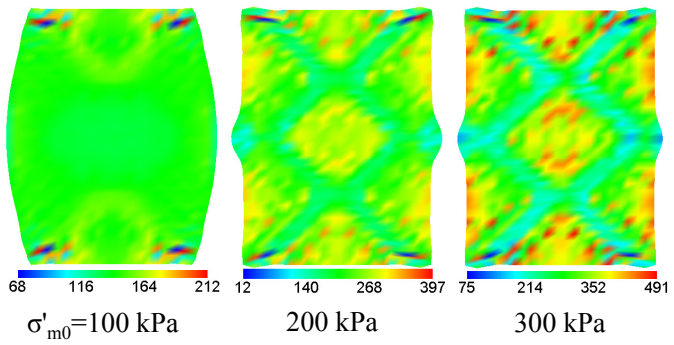

Figure 4.34 Distributions of the mean skeleton stress with different initial confining pressures; Unit(kPa); $s_i = 72\%$, $\varepsilon_a = 20\%$

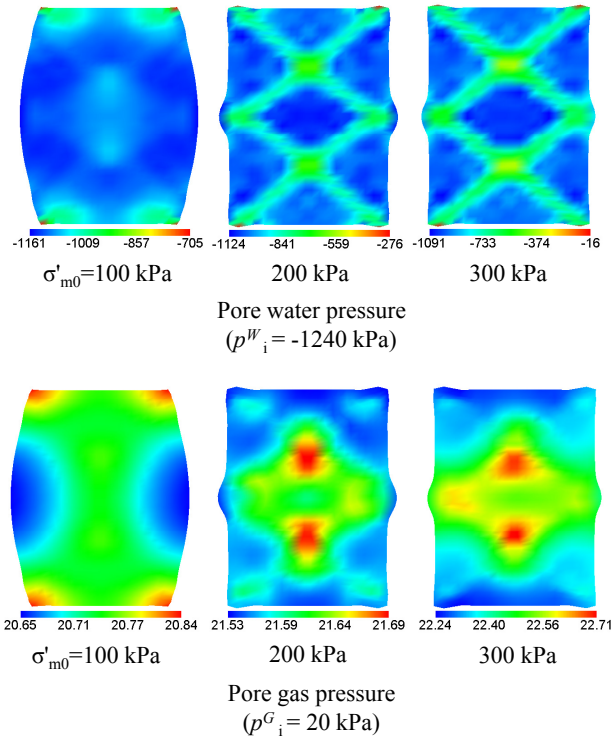

Figure 4.35 Distributions of the pore pressure with different initial confining pressures; Unit(kPa); $s_i = 72\%$, $\varepsilon_a = 20\%$

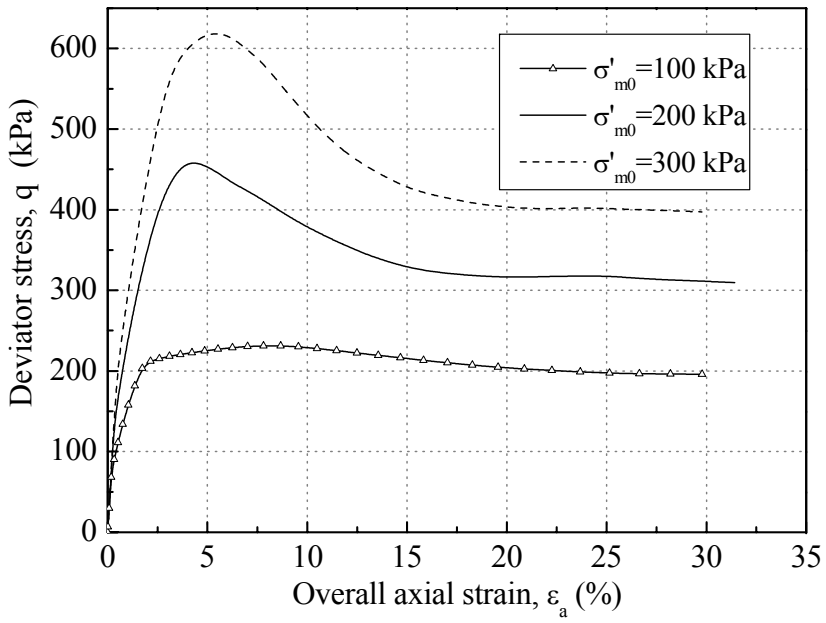

Figure 4.36 Stress-strain relations with different initial confining pressures

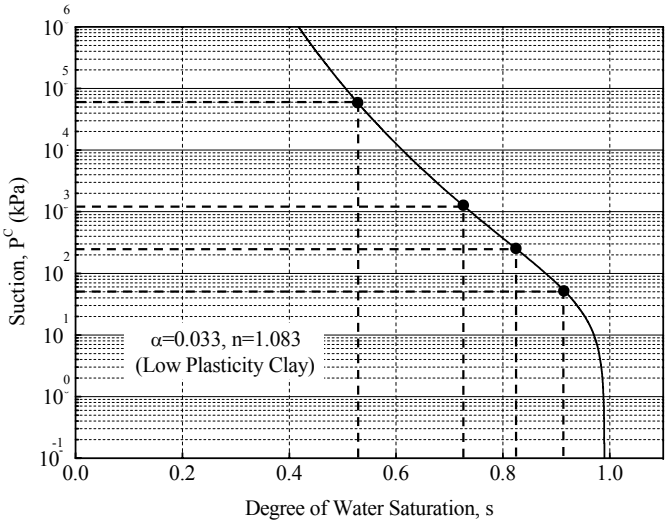

Figure 4.37 Soil-water characteristic curve and initial suctions and saturations for studying the effect of initial suction

conductivity, and the constitutive model. In this section, to study the effect of the initial suction on the strain localization of partially saturated clay, different levels of initial suction, namely, $P_i^C = 63100, 1260, 250$, and 40 kPa which respectively correspond to degrees of saturation of $s_i = 52\%, 72\%, 82\%, 92\%, 100\%$ are considered (See Figure 4.37).

Figures 4.38, 4.39 show the distributions of γ^{vp} and deformed meshes, respectively. It is seen that in a certain value suction, named P_{cr}^C as critical suction, the accumulated shear strain is much more localized than that in other levels of suction. From the figures, it is possible to see that the highest level of localization occurs in the case of $P_i^C = 1260$ kPa,i.e. $P_{cr}^C = 1260$ kPa, which corresponds to $s_i = 72\%$. In case of $s_i = 92\%$, unlike the other cases, the shear banding is not symmetric; also, the failure mode is completely different from the ones in cases with other degrees of saturation. The reason for this behavior might be that this is the only case in which the specimen becomes saturated at some parts during loading (See Figure 4.40).

The stress-strain relations for the various initial suctions are compared in Figure 4.41. It is seen that the shear strength increases with increasing in suction until the suction reaches to the critical value (P_{cr}^C). Then, by increasing suction the strength drops off to a lower value. Such behavior was observed by Bishop and Donald (1961) for tests on sands. Cunningham et al. (2003) was, also, observed the same behavior in the constant-suction triaxial tests on unsaturated silty clay, where the strength decreased with suction increasing above the specific value.

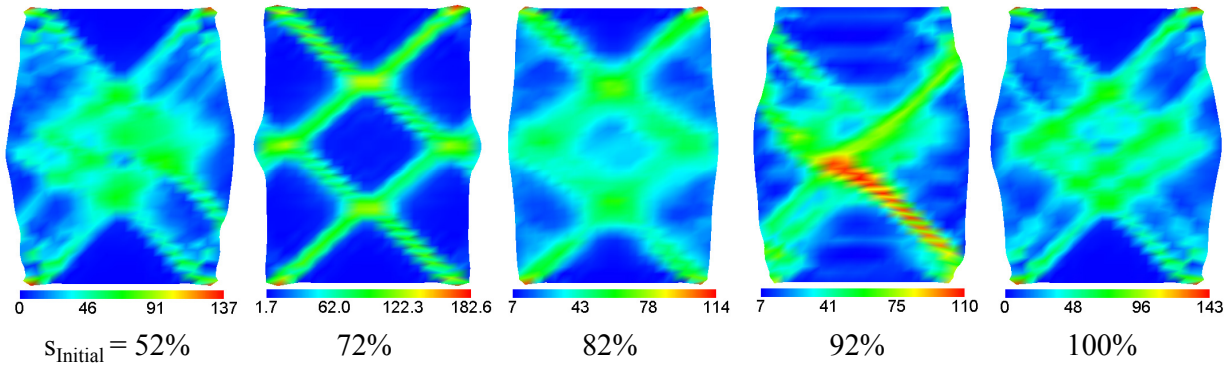

Figure 4.38 Distributions of accumulated viscoplastic shear strain with different initial suctions; Unit(%); $\varepsilon_a = 20\%$

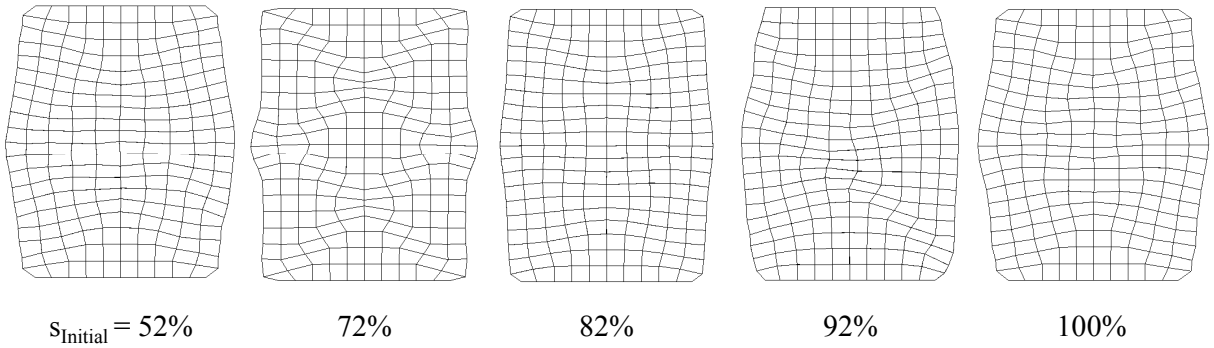

Figure 4.39 Deformed meshes with different initial suctions; $\varepsilon_a = 20\%$

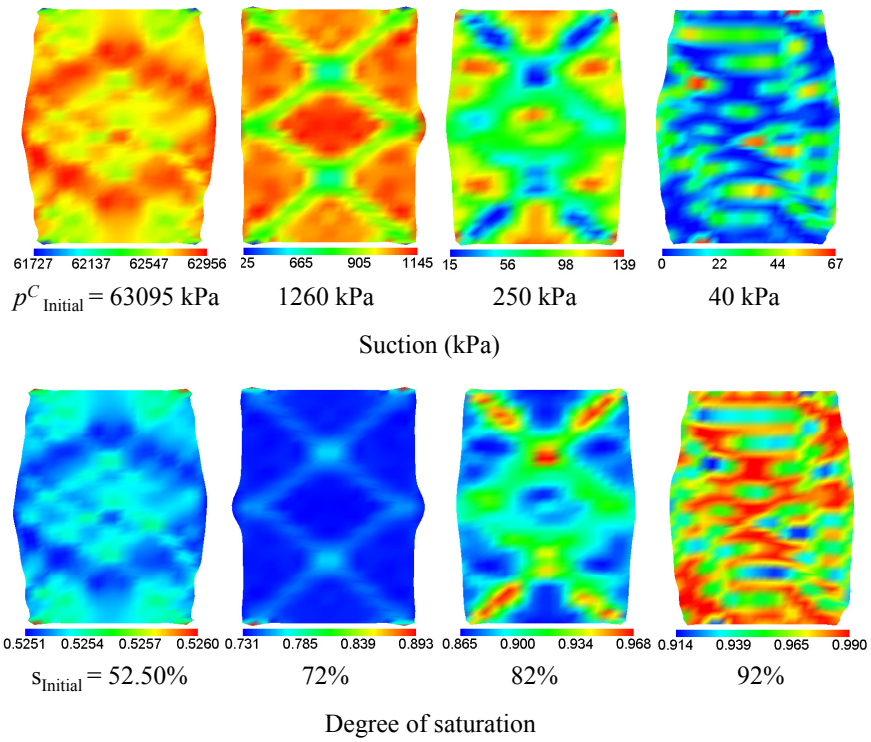

Figure 4.40 Distributions of suctions and saturations with different initial suctions; $\varepsilon_a = 20\%$

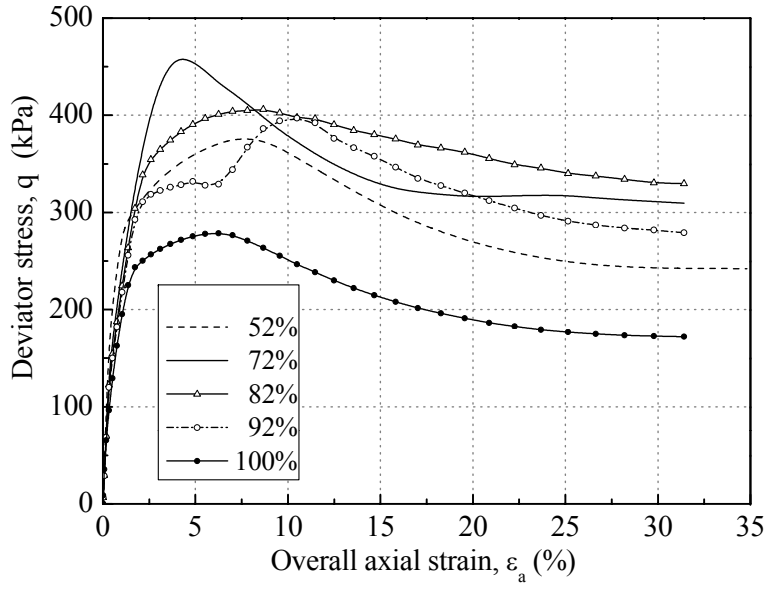

Figure 4.41 Stress-strain relations with different initial suctions

4.10 Summary

the dynamic strain localization phenomenon in saturated and partially saturated clay was studied in the regime of finite deformation by using the multiphase mixture theory and the cyclic elasto-viscoplastic constitutive model. From the results the following concluding remarks can be made:

- In both saturated and unsaturated cases, the similar patterns of shear bands were observed. However, in partially saturated case the strain localized more prominently, and much clearer shear bands were formed.

- By comparing stress-strain relationships, it was found that in unsaturated case the peak strength was higher due to the suction force. Also, it was seen that unsaturated soil reached the peak stress level in smaller axial strain.

- In unsaturated case more brittleness, i.e. strain softening, was observed due to the collapse of suction force caused by shearing. It shows that even though suction improves the soil mechanical properties, i.e. increasing stiffness and shear strength, the hypothesis of saturated material, which is widely used in the analysis of geotechnical problems, is not at all for safety's sake since the partially saturated soil can experience collapse of suction which causes a drastic loss in strength.

- From the local stress-strain relationships, more brittleness was found inside the shear bands than outside of them.

- As the effect of initial suction, it was observed that in a certain value of initial suction, named critical suction (P_{cr}^{C}), shear strain was much more localized than that in other levels of suction. Furthermore, from the stress-strain relations it was seen that the shear strength increased with increasing in suction until the suction reached to the critical value (P_{cr}^{C}). Then, by increasing suction the strength dropped off to a lower value.

- As the effect of strain rate, it was observed that the lower strain rate led to the higher level of shear strain localization; besides, increasing strain rates produced greater peak values.

Chapter 5

Seismic Analysis of Embankments on Non-Liquefiable Soft Soils

5.1 Introduction

Earth embankments have often experienced severe damage during past large earthquakes. Before the Kobe earthquake (1995) few reinforcements against earthquakes were taken into account in the design of the embankments because of the philosophy that it is easy to restore these kinds of earth structures rapidly before any flooding. The 1995 Hyogoken-Nambu earthquake hit many dikes such as 8.1 meter high Torishima dike along the Yodo river which settled 2.7 meters. After this earthquake, the ministry of construction of Japan started a program to improve the seismic provisions for designing earth structures, and to remediate existing vulnerable embankments. However, during the great east Japan earthquake on March 11, 2011 (The 2011 off the Pacific coast of Tohoku Earthquake), which was quickly followed by Tsunami, overflow due to the dike settlement and the failure of embankments caused significant economic damage and loss of life. It proved that it is still necessary to develop the prediction methods of seismic behavior of earth embankments in order to improve the seismic provisions.

Although most of severe damage to embankments was triggered by the occurrence of soil liquefaction beneath the embankments during past earthquakes, some case histories demonstrated that earth embankments resting on non-liquefiable soft soils have also experienced extensive seismic damage. In this study, the different modes of failure affecting embankments as a consequence of earthquake shaking are presented and discussed. Furthermore, the seismic behavior of an embankment on non-liquefiable soft clay is numerically studied. The cyclic elasto-viscoplastic model for partially saturated soils described

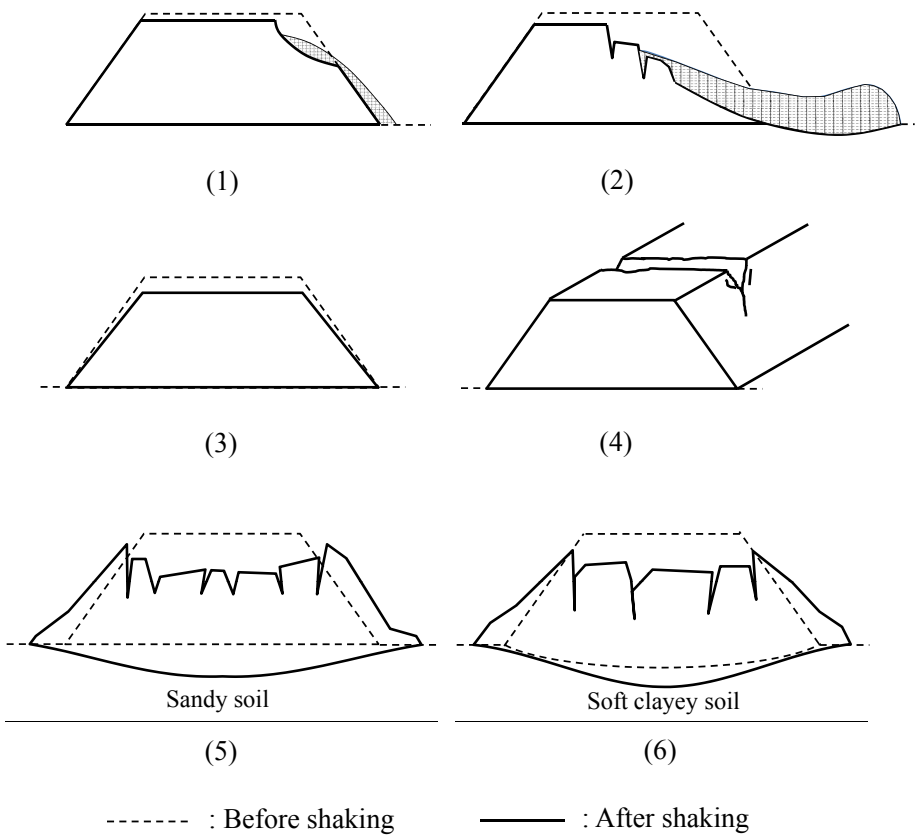

Figure 5.1 Potential failure modes of embankments: (1) Shallow sliding failure, (2) Deep sliding failure, (3) Subsidence without apparent cracks, (4) Transverse fractures, (5) Subsidence of embankment on liquefiable soft soil, (6) Subsidence of embankment on soft clayey soil.

in chapter 2 is applied to the embankment and the stratified ground. The simulation is performed for two cases with different ground water levels, namely,

- The case in which the water level is considered at the surface of the ground; that is, the embankment is partially saturated and the ground is fully saturated.

- The case in which the water level is below the clayey layer; in other words, both the embankment and the clayey layer are in the partially saturated condition.

5.2 Seismic Failure Modes of Embankments

Over the years, several types of earthquake damage have been observed in embankments. In general, seismic failure modes of earth embankments can be classified into six types shown schematically in Figure 5.1.

Figure 5.2 Shallow sliding failure in a road embankment in Chokubetsu, Onbetsu-cho during the 2003 Tokachi-oki Earthquake, Hokkaido, Japan (Yoshimine, 2003)

Type 1) Shallow sliding failure: It is a minor failure at the surface of the slope, which might also affect the small parts of the crest. This type of failure is not significant and can easily be repaired. Figure 5.2 shows the shallow sliding failure to a road embankment damaged during the 2003 Tokachi-oki Earthquake.

Type 2) Deep sliding failure: In this pattern of damage, the sliding plane is deep inside the body of the embankment. Foundation soil liquefaction has mainly caused this type of severe damage to many embankments during past large earthquakes. This type of failure is the most common seismic failure mode observed in embankments. The example of this pattern of failure is illustrated in Figure 5.3 where a road embankment slid several meters downslope in Fukushima prefecture during Tohoku earthquake on March 11, 2011.

Type 3) Subsidence without apparent cracks: Although large settlement occurs, no visible deformation is usually observed on the crest of the embankment in this type of damage. In this case the embankment is compacted; thus, no tension cracks can be seen in the structure.

Type 4) Transverse fractures: Transverse fractures in the crest of embankments are associated with strong longitudinal oscillations or with a transverse asynchronous excitation. The example of this type of failure is shown in Figure 5.4. It is seen that the transverse fracture offset the surface of a river dike about 14 cm during the 2010 Sierra El Mayor - Cucapah earthquake, Mexico.

Figure 5.3 Deep sliding failure in a road embankment in Fukushima prefecture during the 2011 Tohoku Earthquake (Yoshimine, 2011)

Figure 5.4 Transverse fracture offset the crest of the dike at the Westside Main Canal of the Alamo river during the 2010 Sierra El Mayor - Cucapah earthquake, Mexico (the GEER Association website)

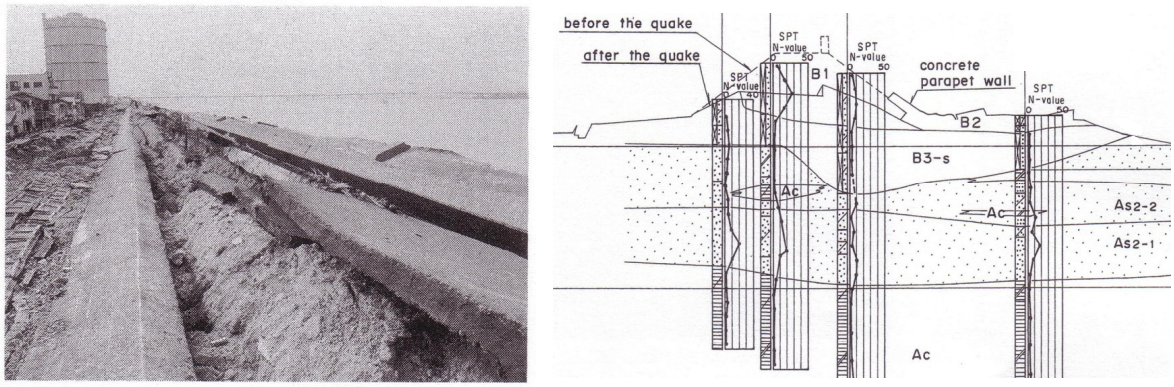

Figure 5.5 Subsidence along Torishima dike, the left levee of the Yodo River, due to the liquefaction of its foundation soil during the 1995 Hyogoken-Nambu earthquake (Matsuo, 1996)

Type 5) Subsidence of embankment on liquefiable soft soil: In this type of failure subsoil liquefies due to ground motions, and large lateral deformation takes place in the foundation of the embankment. Consequently, the embankment subsides and spreads laterally simultaneously, which causes wide longitudinal tension cracks to develop in the crest of the embankment. Figure 5.5 shows an example of this type of failure where Torishima dike, the left levee of the Yodo River, was severely damaged during the 1995 Hyogoken-Nambu earthquake.

Type 6) subsidence of embankment on non-liquefiable soft soil: Although most of the failure of embankments was associated with liquefaction of foundation soils, many embankments resting on non-liquefiable soft soils have also experienced severe damage during past large earthquakes. The damage included the subsidence of the crest, deep longitudinal cracks, and lateral stretching of the embankment. In this type of failure the compressible soft foundation soil deforms unevenly, which cause the embankment settle and experience higher levels of vertical stress at its central part. Due to this uneven deformation of the foundation, lateral tension stress takes place in the body of the embankment which leads to the appearance of deep longitudinal cracks. This type of failure was observed in several embankments during the 2011 Tohoku earthquake (See Figure 5.6 as an example). Another reason for this type of failure can be that prior to the earthquake the bottom part of the embankment settles below the ground water table due to the consolidation of the soft foundation. This saturated zone of the embankment liquefies during the earthquake, which causes the embankment body to sink into the soft foundation layer.

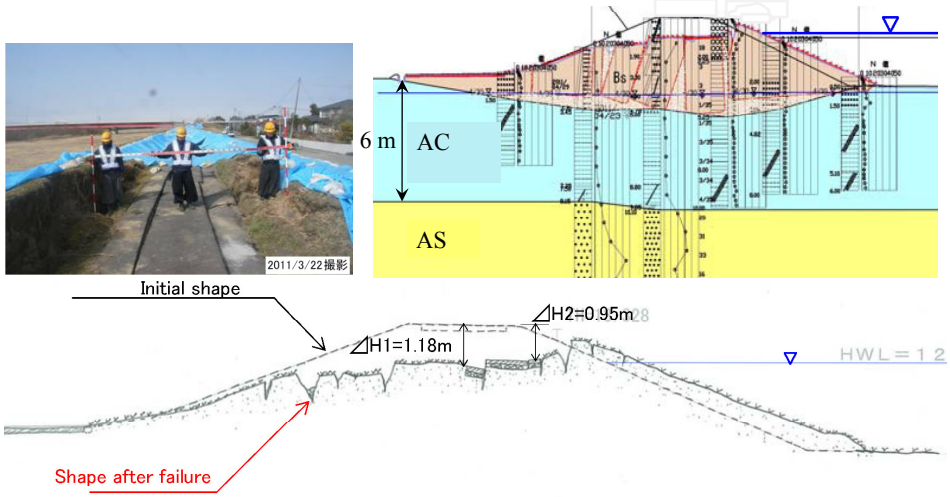

Figure 5.6 Subsidence of the embankment along the Eai river on non-liquefied soft clayey soil during the 2011 Tohoku earthquake (Picture by Kitakamigawa-Karyu river office Tohoku regional bureau, 2011)

5.3 Seismic Analysis of Embankments

In this section, the seismic simulation of a partially saturated embankment resting on non-liquefiable foundation is performed using the finite element method for two cases with different ground water levels, namely,

- The case in which the water level is considered at the surface of the ground; that is, the embankment is partially saturated and the ground is fully saturated.

- The case in which the water level is below the clayey layer; in other words, both the embankment and the clayey layer are in the partially saturated condition.

The geometry of the finite element model and the boundary conditions are depicted in Figure 5.7. The simulations are accomplished using a three-dimensional mesh system under plane strain conditions, for which the unit length is considered in the third dimension, and the deformations in that direction are restricted. The boundaries of the embankment and the top surface of the ground are considered to be drainage if the pore water pressure is positive; however, when the pore water pressure is negative, these boundaries are assumed to be no-water-flow boundaries in order to avoid the fictitious water flow-in. The side boundaries of the ground are impervious and supported horizontally. The bottom surface of the ground is fixed in both horizontal and vertical directions and impervious. In the analysis, the initial pore water pressure below the water level is given by the hydrostatic pressure, while for the unsaturated part of the system the initial suction is assumed

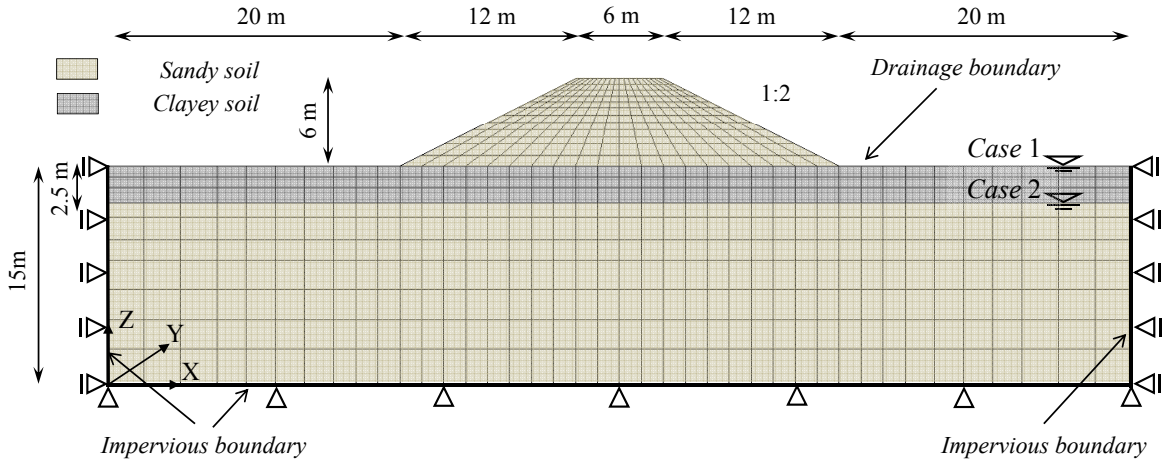

Figure 5.7 Finite element mesh and boundary conditions

to be spatially constant, and it is considered $P_i^C = 6\text{kPa}$. In the transition region between the water level and the constant-suction region, it is assumed that the pore water pressure is linearly interpolated, as shown in Figure 5.8. The initial skeleton stresses is calculated by static finite element analysis of the system using the Elasto-perfectly plastic constitutive model which has the failure boundary surface of the Drucker-Prager model. The distributions of initial mean skeleton stress are shown in Figure 5.9.

The material parameters for the embankment and the multi-layered ground used in the analysis are listed in Tables 5.1 and 5.2. For the input ground motion, as illustrated in Figure 5.10, a wave with a maximum acceleration of 509 gal is assumed based on a NS component of an earthquake record on Port Island, Kobe City during the 1995 Kobe (Hyogoken-Nambu) Earthquake, and applied in the horizontal direction. The major shock occurs in $10sec$ and after that, the simulation is carried on until $25sec$ to evaluate the post-quake responses. In the dynamic analyses, an initial stiffness dependent type of Rayleigh damping is adopted with the attenuation constant equal to 0.01. For the time integration the Newmark's β method is adopted with β and γ being set to be 0.3025 and 0.6, respectively. In addition, the incremental time interval considered for the numerical analysis is set to be $0.0005sec$ for the major shock duration, and $0.005sec$ for the post-quake.

The dynamic analysis results are presented as acceleration responses, and time histories of displacements in both vertical and horizontal directions at several points and sections of the embankment. The location of these reference points and sections are depicted in Figure 5.11. In addition, the distribution contours of the lateral strain, and

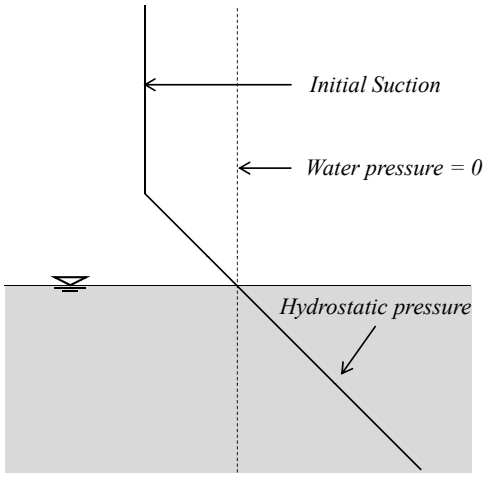

Figure 5.8 Initial Pressure head

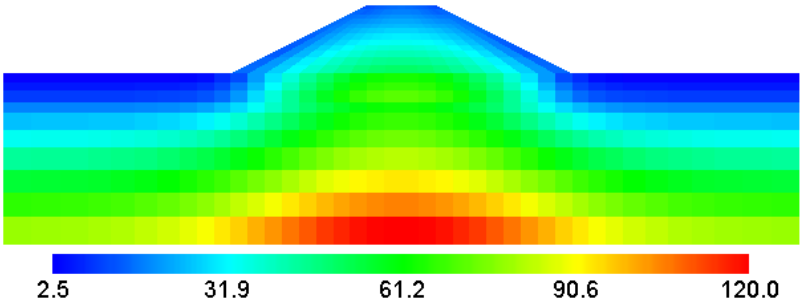

(Case 1)

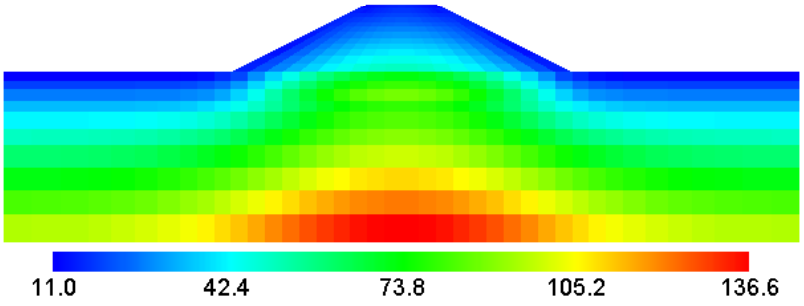

(Case 2)

Figure 5.9 Initial mean skeleton stress contours (Unit: kPa), Case 1: with fully saturated clayey layer, Case 2: with partially saturated clayey layer.

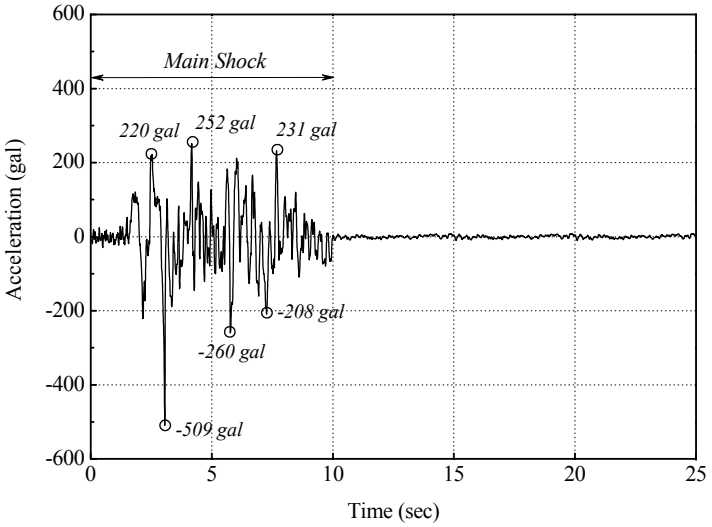

Figure 5.10 Input earthquake wave

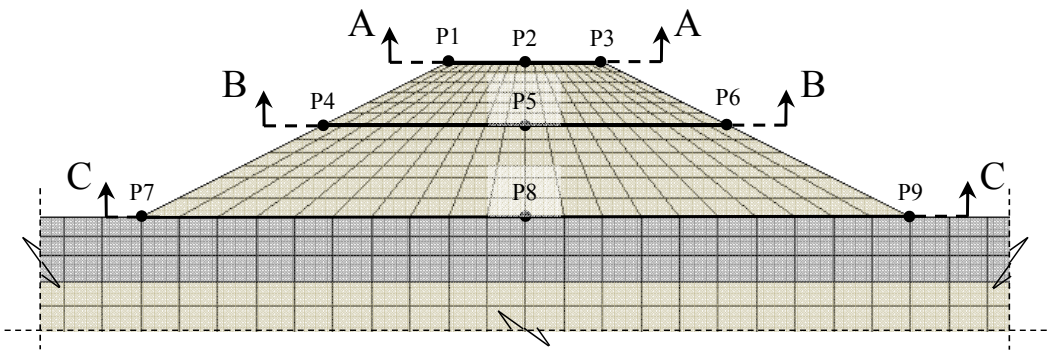

Figure 5.11 Nodes and sections for which the numerical results discussed

accumulated viscoplastic shear strain are exhibited at the end of seismic loading.

5.3.1 Acceleration Responses

Figures 5.12 and 5.13 show the acceleration responses at the selected points along the bottom, mid-height, and crest of the embankment for the case with the saturated clayey layer and the case with the partially saturated clayey layer, respectively. In the whole embankment, amplification in the acceleration responses is observed. By comparing the responses at the different elevations, the highest amplification occurs at the crest. Furthermore, much higher levels of acceleration are seen in the case with partially saturated clayey layer in comparison with the ones in the saturated case. In other words, lower water levels lead to higher amplification in the acceleration responses of the embankment.

Table 5.1 Material parameters for the embankment and the multi-layered ground

		Clayey soil*	Sandy soil**
Initial void ratio	e_0	1.25	0.65
Quasi-overconsolidation ratio	$OCR^* = \frac{\sigma'_{mai}}{\sigma'_{m0}}$	1.0	1.4
Density (t/m^3)	ρ	1.66	1.90
Compression index	λ	0.341	0.061
Swelling index	κ	0.019	0.004
Water permeability s=1 (m/s)	k_s^W	5.77×10^{-10}	1.00×10^{-5}
Normalized initial shear modulus (kPa)	G_0/σ'_{m0}	75.2	157.5
Stress ratio at failure	M_m^*	1.24	1.18
Viscoplastic parameter	m'	24.68	40.0
Viscoplastic parameter ($1/s$)	C_1	1.00×10^{-6}	1.00×10^{-5}
Viscoplastic parameter ($1/s$)	C_2	3.83×10^{-7}	1.00×10^{-5}
Structural parameter	$n = \sigma'_{maf}/\sigma'_{mai}$	0.3	0.53
Structural parameter	β	3.6	5.0
Hardening parameter	B_0^*	100	200
Hardening parameter	B_1^*	40	15
Hardening parameter	C_f	10	5
Strain-dependent modulus parameter	α'	10	1.0
Hardening parameter	A_2^*	5.9	9.0
Hardening parameter	B_2^*	1.8	3.6
Suction parameter	S_I	0.50	0.20
Suction parameter	s_d	0.25	0.60

* Torishima clay

** Sandy soil with 90% degree of compaction used for the construction of the Yodo river embankment

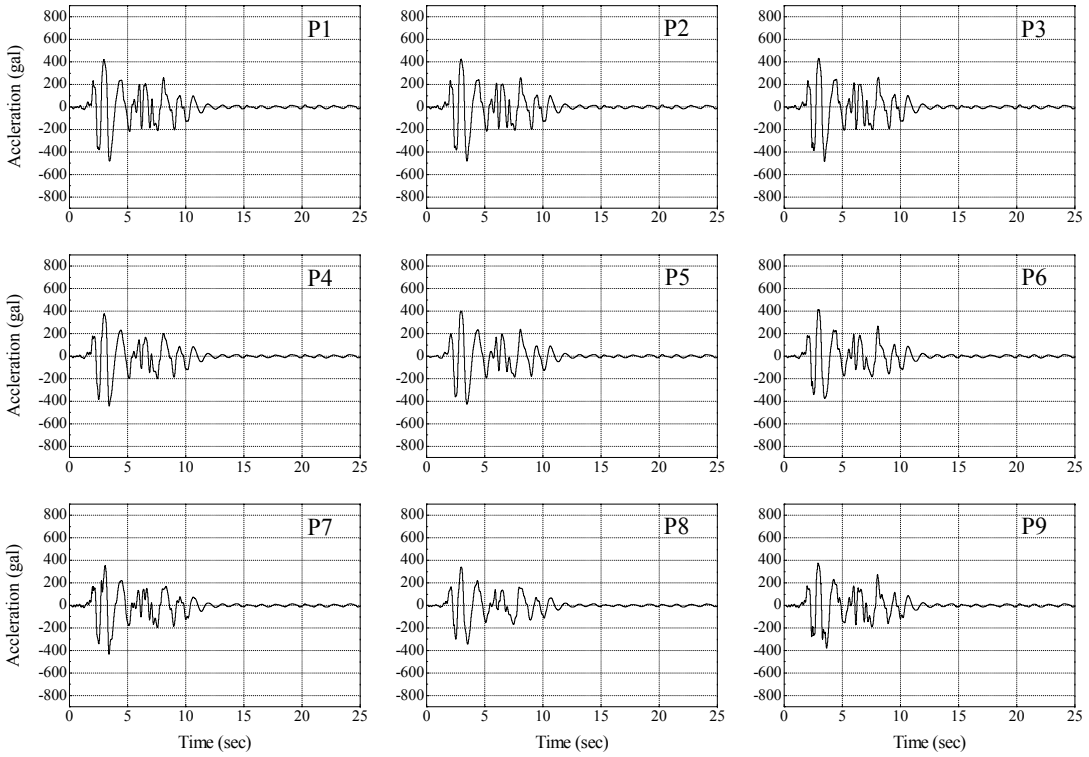

Figure 5.12: Horizontal acceleration responses; Case1 with fully saturated clayey layer

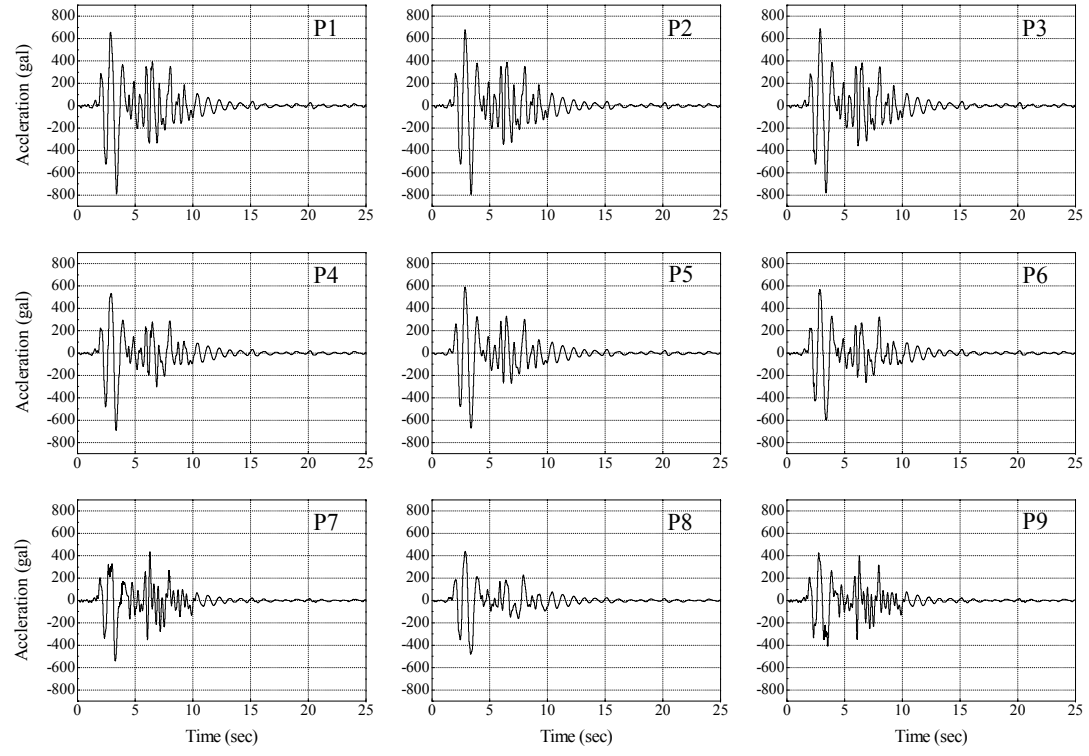

Figure 5.13: Horizontal acceleration responses; Case2 with partially saturated clayey layer

Table 5.2 Soil-water characteristic curve parameters used for the partially saturated materials

		Clayey soil	Sandy soil
Van Genuchten parameter (1/kPa)	α	0.033	10.00
Van Genuchten parameter	n	1.083	1.068
Minimum saturation	s_{min}	0.00	0.00
Maximum saturation	s_{max}	0.99	0.75
Shape parameter of water permeability	a	3.0	3.0
Shape parameter of gas permeability	b	2.3	1.0

5.3.2 Horizontal Displacements and Lateral Strains

The time histories of horizontal displacement at the selected points are illustrated in Figures 5.14,5.15 for the cases with fully saturated and partially saturated clay layer, respectively. In the partially saturated case, the maximum lateral displacement equal to 20 cm takes place at the crest of the embankment during the main shock. On the contrary, in the case with saturated clay layer, the maximum value (equal to 28 cm) occurs at the toe of the embankment at the end of the earthquake. By comparing the responses along section A, almost rigid horizontal displacement is observed at the crest of the embankment in both cases. However, the results show lateral stretching along the mid-height and the base. By comparison between the two cases, the embankment resting on partially saturated foundation soil shows stiffer lateral response.

The distribution contours of lateral strain, ε_x, at the end of loading are shown in Figure 5.16. It is possible to see that lateral extensional strain is developed in the central part of the embankment during the earthquake, which can cause deep longitudinal tension cracks in the body of the embankment.

5.3.3 Vertical Displacements

From the histories of vertical displacement shown in Figures 5.17 and 5.18, it is possible to see that the displacement increases during the main shock within 10 sec, while the embankment almost does not settle or deform after the shock. Figures 5.19 to 5.21 show the settlement of the crest, mid-height, and the bottom of the embankment at several steps of analysis, respectively. It is observed that the crest settles around 15cm in the case where the ground is fully saturated, and around 10cm when the initial water level is below the clayey layer. In both cases, however, no significant deformation occurs at

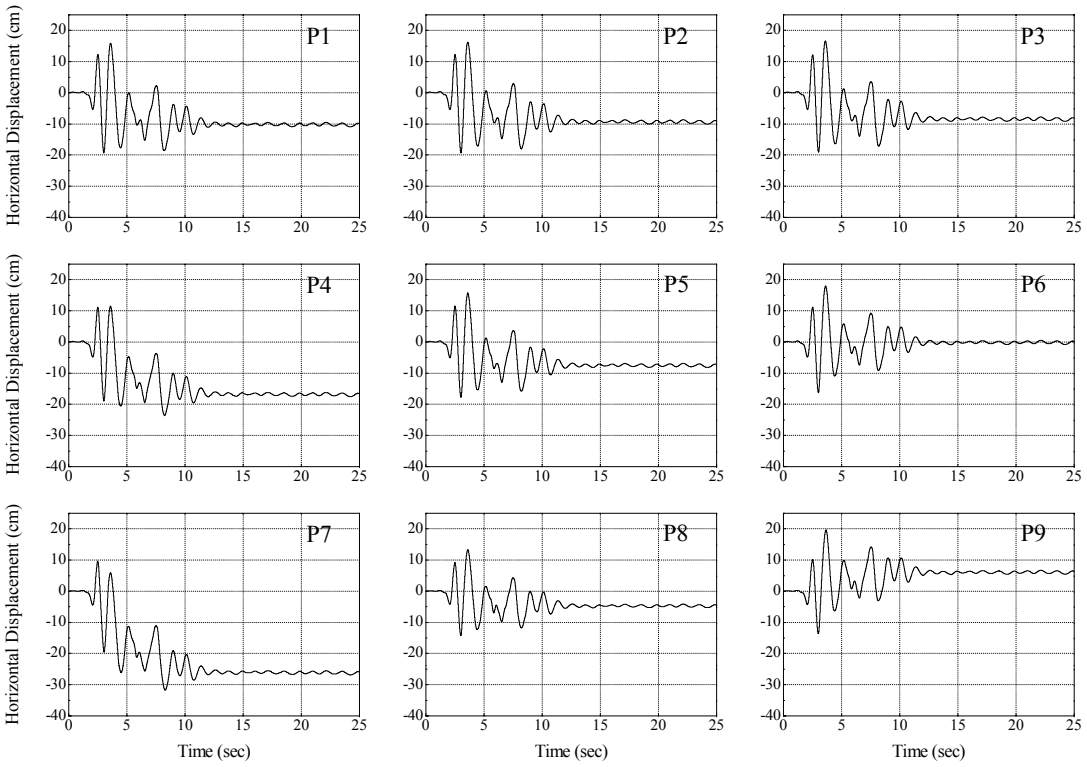

Figure 5.14 Horizontal displacement-time histories; Case1 with fully saturated clayey layer

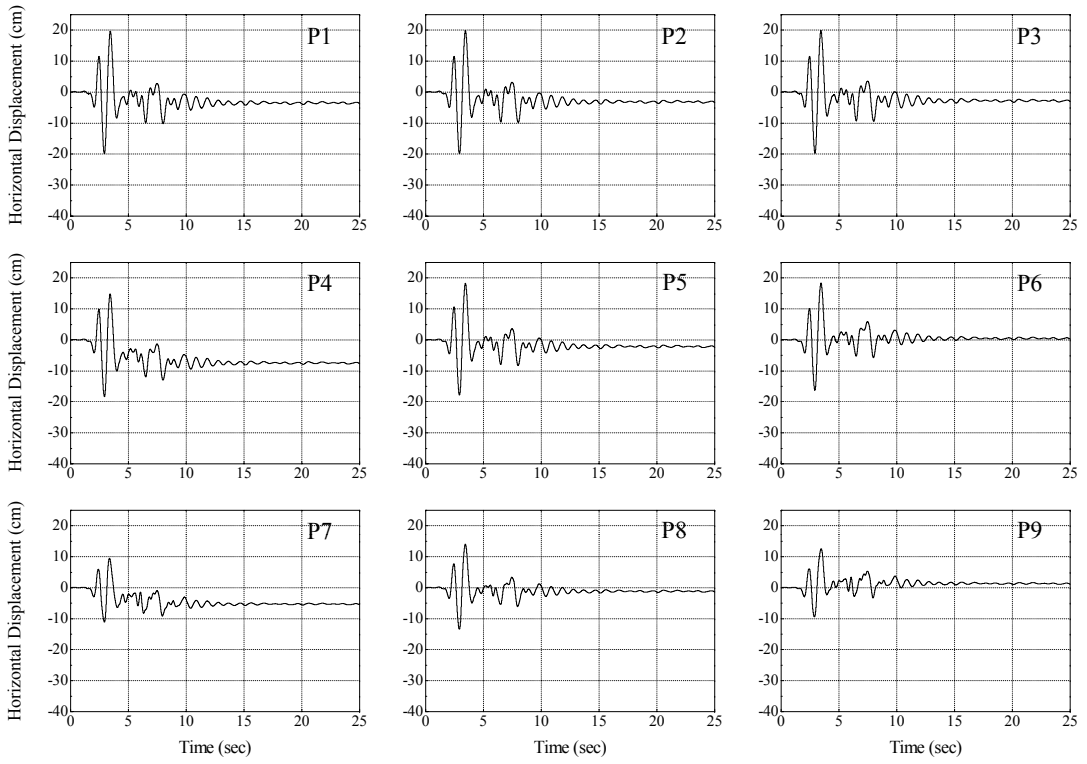

Figure 5.15 Horizontal displacement-time histories; Case2 with partially saturated clayey layer

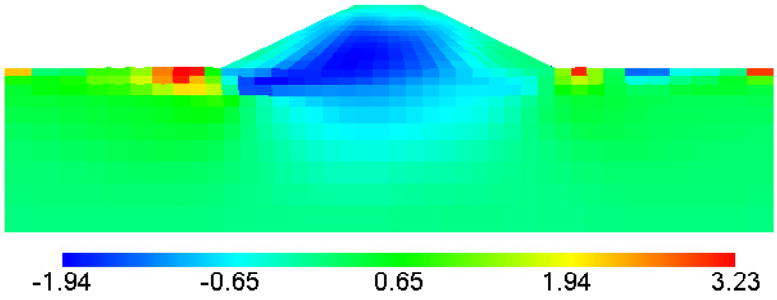

(Case 1)

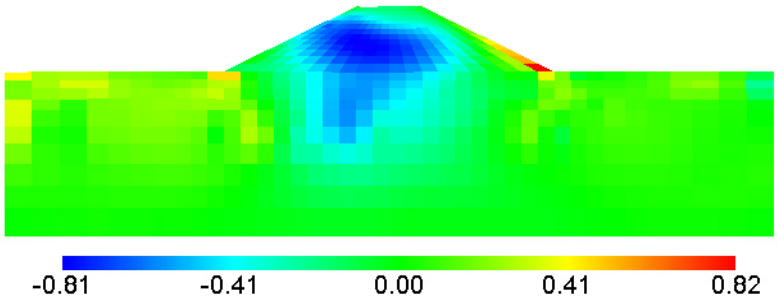

(Case 2)

Figure 5.16 Distributions of lateral strain ε_x (%); Case1 with fully saturated clayey layer, Case2 with partially saturated clayey layer

the crest. The maximum deformation takes place at the bottom of the embankment. This deformation is larger in the case with fully saturated clay layer, where the bottom center of the embankment sinks down into the soft foundation soil, and the toes of the embankment heave.

Figures 5.22 and 5.23 show the deformed meshes at the end of earthquake, $t = 25sec$. The displacements in the deformed meshes are magnified 20 times for clarity. It is seen that the behavior of the simulated embankments is consistent with the failure mode observed in the real cases, where the subsidence of the crest and lateral stretching take place in the embankment. However, the simulated failure is not severe compared to this type of damage occured in embankments during past large earthquakes due to the well compacted material used for the embankment. The severity of damage can be related to many factors such as the input waves, the material parameters, and the depth of the soft soil. Therefore, further study is still necessary to recognize the effects of these factors on this type of failure mode.

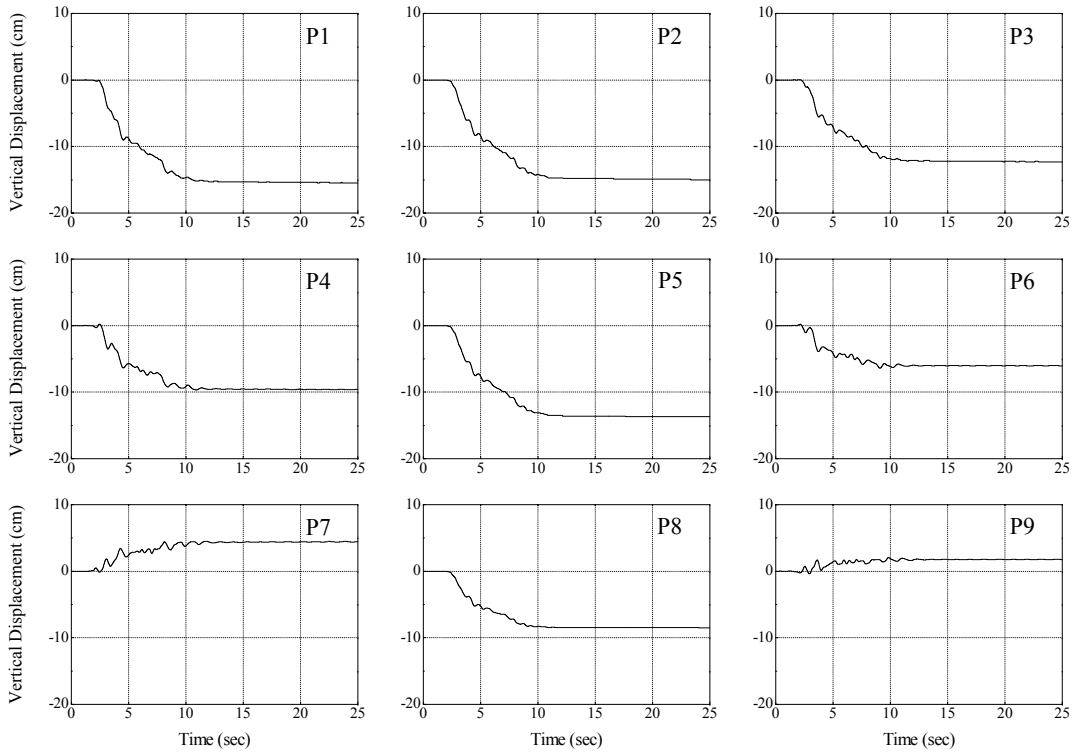

Figure 5.17 Vertical displacement-time histories; Case1 with fully saturated clayey layer

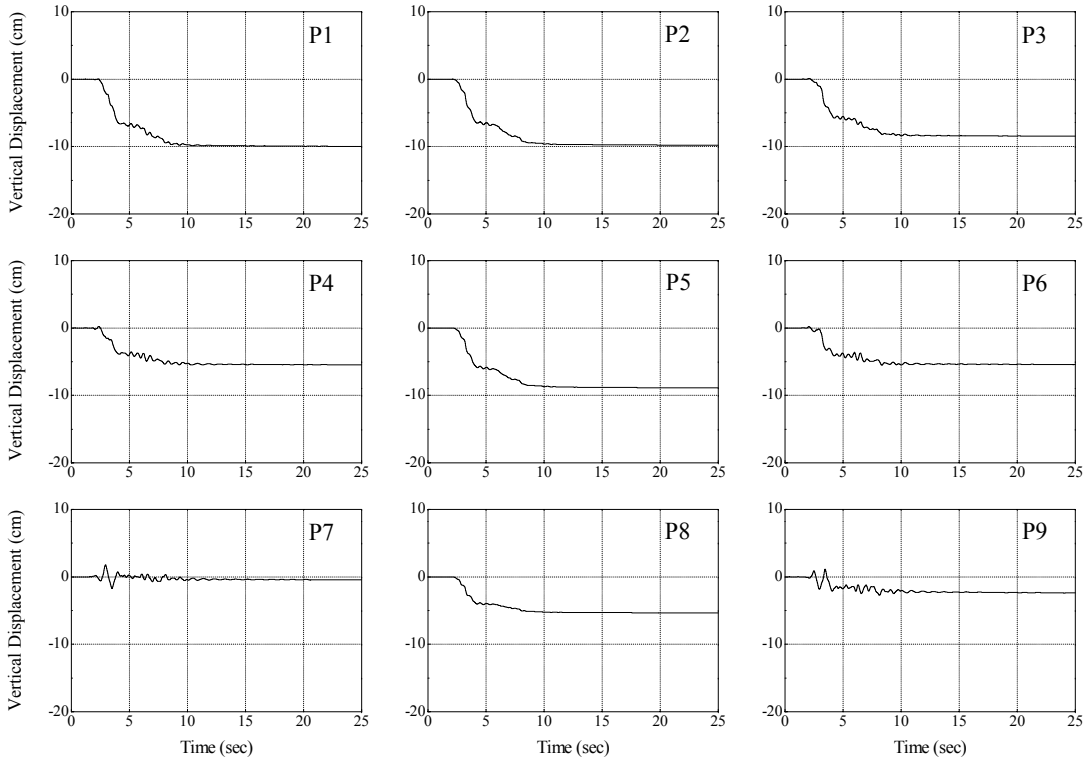

Figure 5.18 Vertical displacement-time histories; Case2 with partially saturated clayey layer

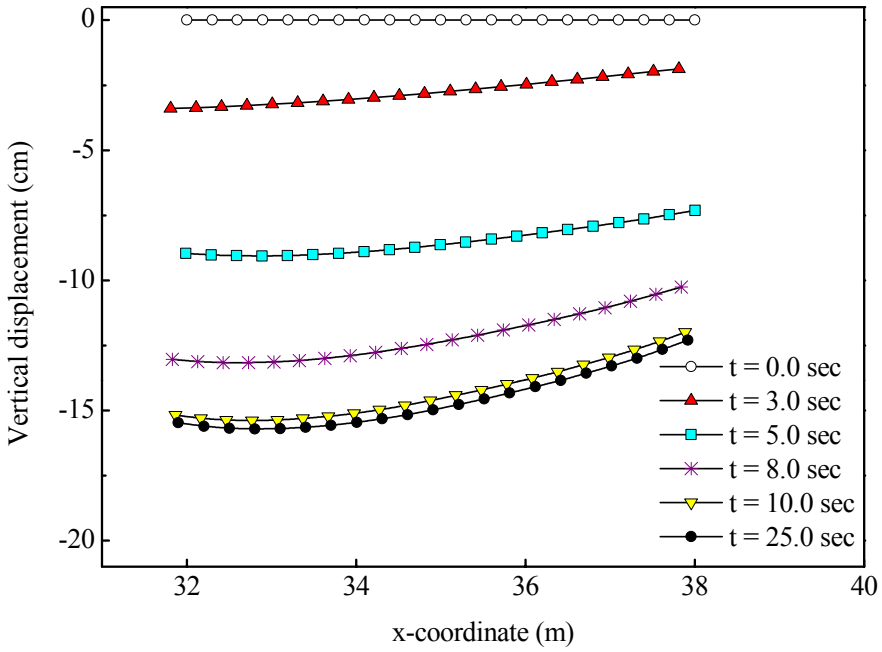

(Case 1)

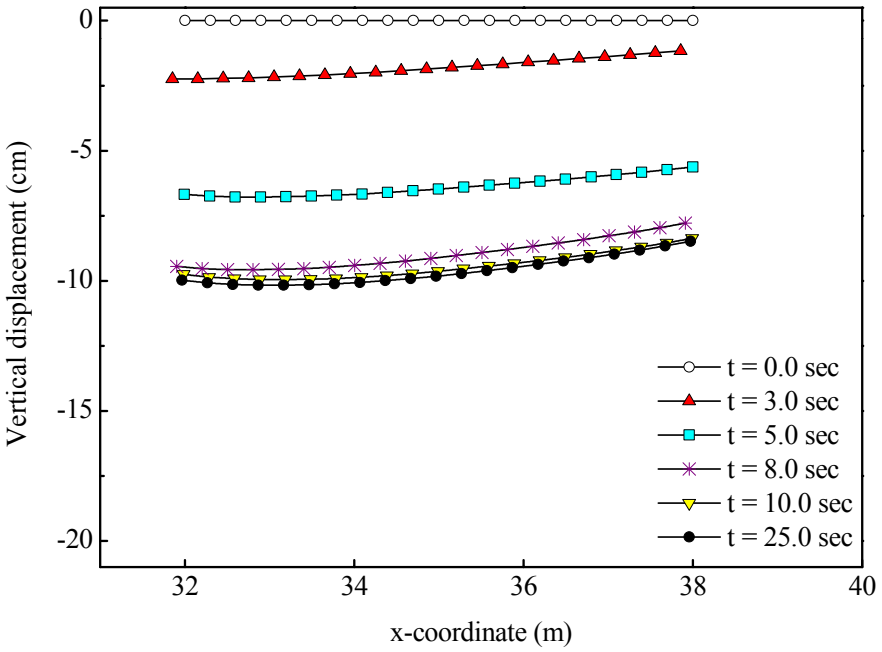

(Case 2)

Figure 5.19 Settlements at the crest of the embankment; Case1 with fully saturated clayey layer, Case2 with partially saturated clayey layer

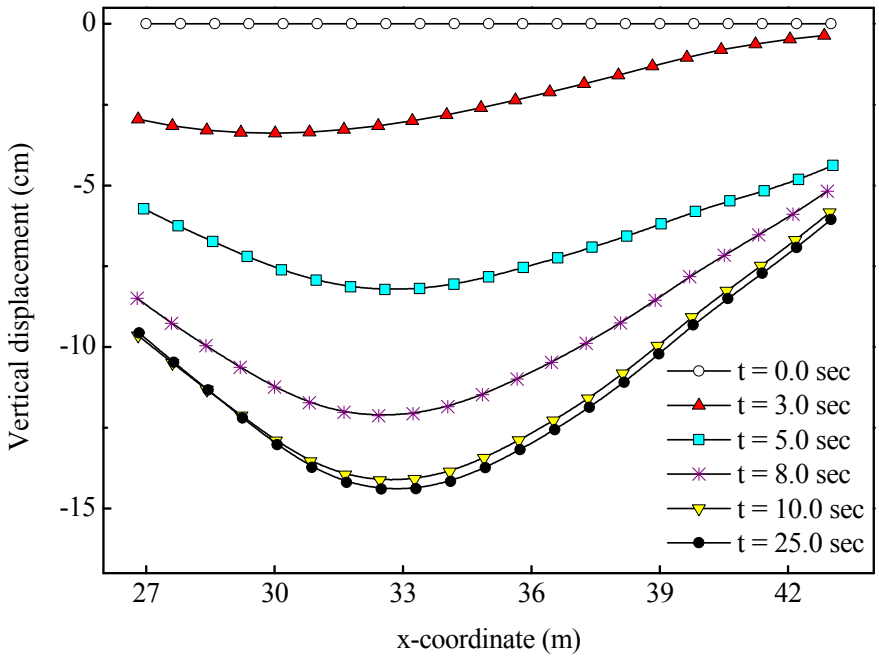

(Case 1)

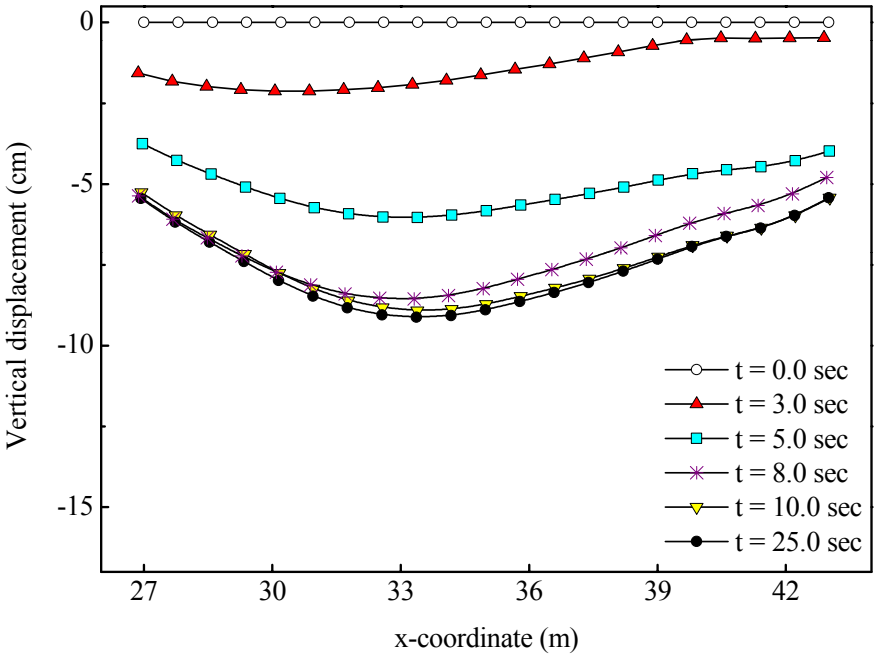

(Case 2)

Figure 5.20 Settlements at the mid-height of the embankment; Case1 with fully saturated clayey layer, Case2 with partially saturated clayey layer

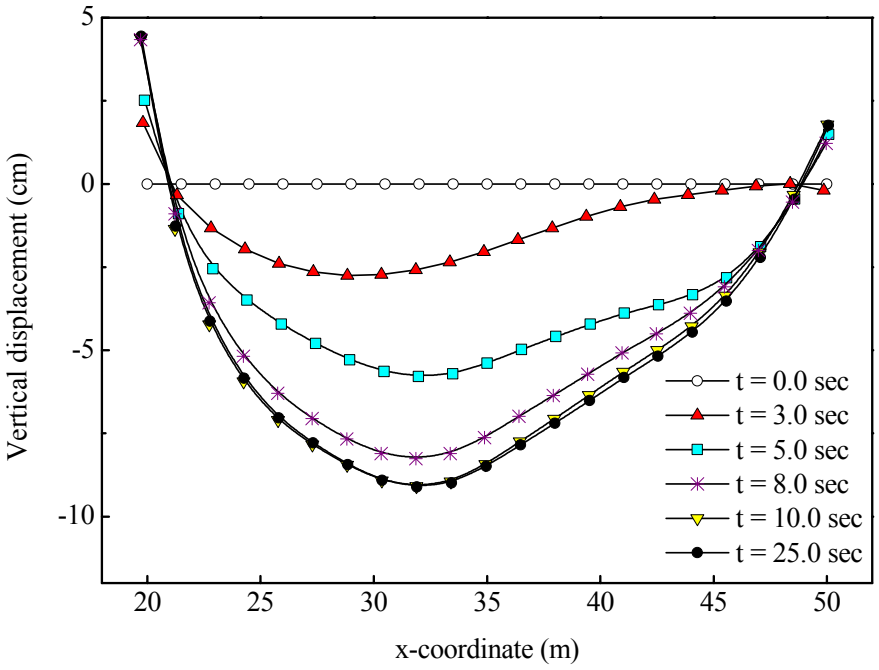

(Case 1)

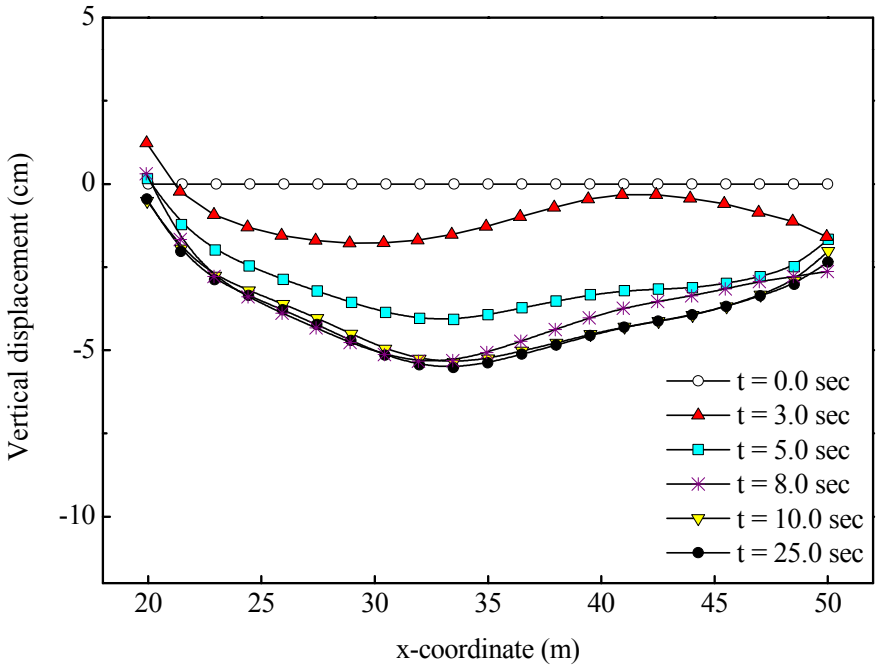

(Case 2)

Figure 5.21 Settlements at the embankment base; Case1 with fully saturated clayey layer, Case2 with partially saturated clayey layer

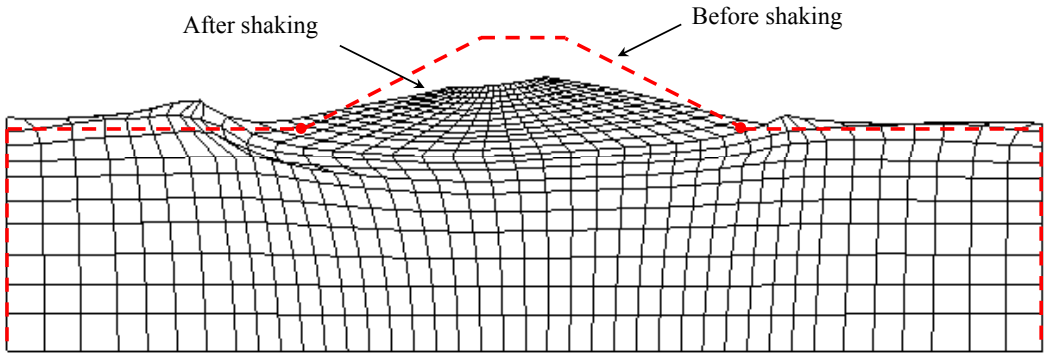

Figure 5.22 Deformed mesh for the case with fully saturated clayey foundation at time $t = 25sec$; magnified 20 times for clarity

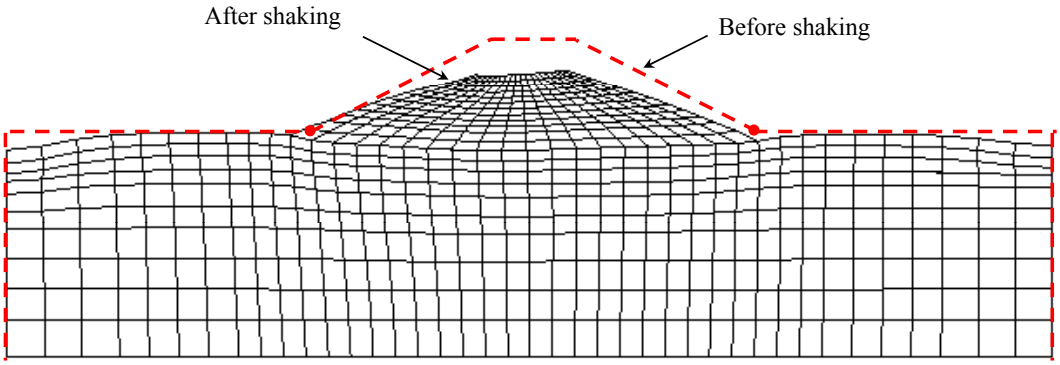

Figure 5.23 Deformed mesh for the case with partially saturated clayey foundation at time $t = 25sec$; magnified 20 times for clarity

5.3.4 Accumulated Viscoplastic Shear Strain

The distribution contours of the accumulated viscoplastic shear strain at the end of seismic loading are shown in Figure 5.24. In the case where the initial water level is at the surface of the ground, high levels of accumulated shear strain are localized in the clayey layer. By comparing between the two cases, it is seen that higher levels of γ_{vp} take place in the embankment when the clayey layer is partially saturated. In this case the maximum shear strain equal to 11.4% is observed at the toe, while in the case with fully saturated clay layer the maximum value equal to 5.7% occurs at the bottom center of the embankment.

5.4 Summary

In this chapter, the different modes of failure affecting embankments as a consequence of earthquake shaking were presented and discussed. Furthermore, the seismic behavior of a partially saturated embankment on non-liquefiable soft clay was numerically studied in two cases with different ground water levels: First, the case in which the water level was considered at the surface of the ground, and second, the case in which the water level was taken below the soft clayey layer. The simulated failure had the same tendency as the ones observed in the real cases. In other words, the subsidence of the crest and lateral stretching in the body of the embankment were observed in the simulated results. By comparing the results in the two cases, the case with unsaturated clayey layer showed higher amplification in acceleration responses. Moreover, from the distributions of accumulated viscoplastic shear strain in the embankment, higher levels of shear strain were seen in this case. In the case with fully saturated clayey layer, on the other hand, higher levels of horizontal displacements and larger settlement were observed.

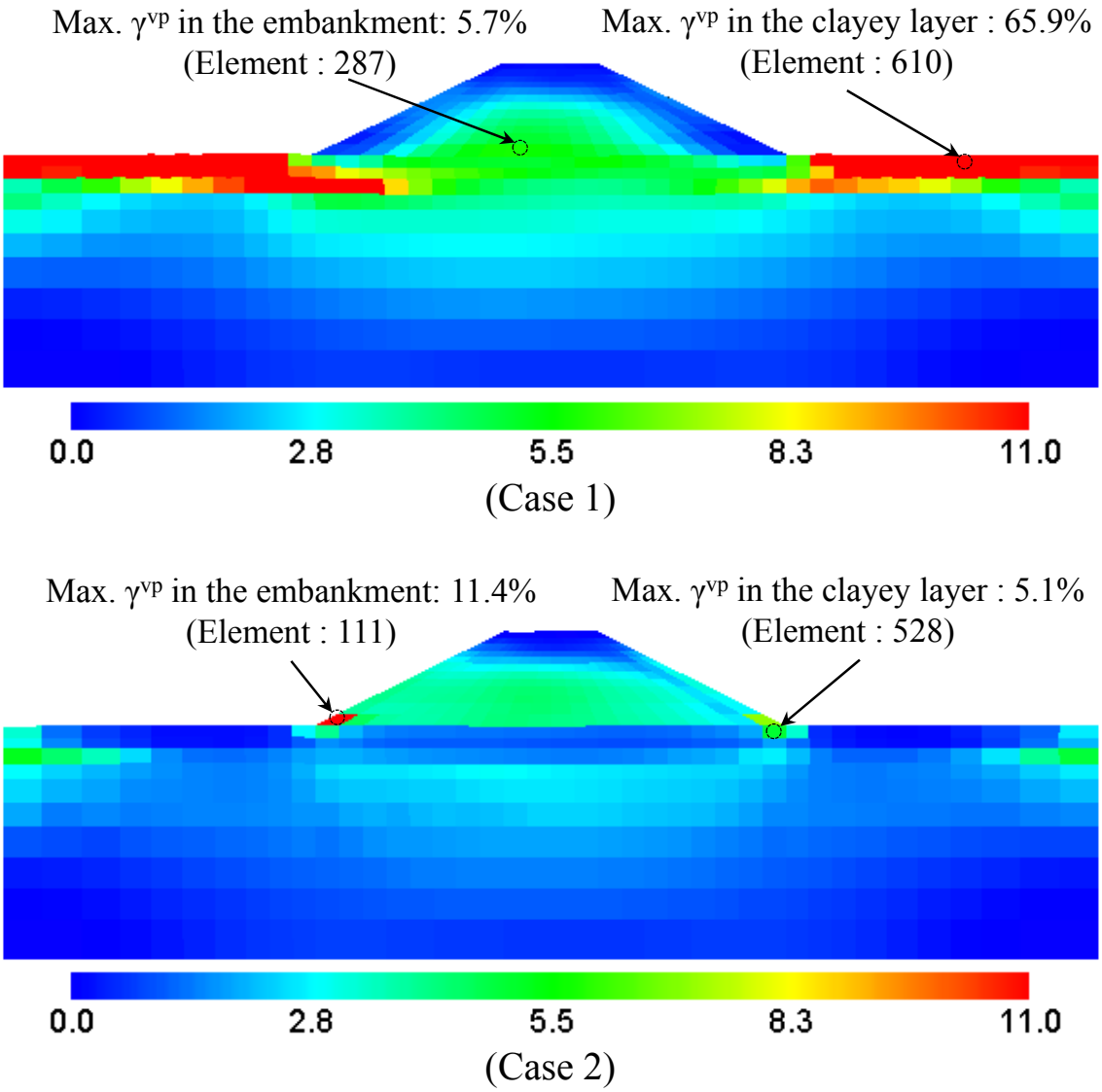

Figure 5.24 Distributions of accumulated viscoplastic shear strain (Unit: %); Case1 with fully saturated clayey layer, Case2 with partially saturated clayey layer

Chapter 6

Conclusion

6.1 Concluding remarks

In this study, a mathematical framework for large deformation dynamic analysis of partially saturated Elasto-viscoplastic soils was introduced. Using this method, the dynamic strain localization phenomenon in saturated and partially saturated clay was studied. Moreover, the seismic behavior of partially saturated embankments on non-liquefiable soft clay was numerically simulated. The conclusions obtained in each chapter are described below.

In **Chapter 2**, The cyclic Elasto-viscoplastic constitutive model presented by Sawada (2008) was extended for partially saturated soils using the skeleton stress and suction effect in the constitutive model. The performance of the model was verified, first through the modeling of fully saturated soft clay specimens under undrained cyclic and monotonic triaxial conditions, and then through the simulation of partially saturated sand specimens under cyclic suction-controlled triaxial conditions.

In **Chapter 3**, the no rate type of finite element formulation suitable for large deformation dynamic analysis was extended to the case of multiphase materials. Detailed derivations of the governing equations and the conservation laws of multiphase porous media were presented. Newmark's β method was adopted as a time integration algorithm to discretize the governing equations in time. The van Genuchten type of equation was, also, employed as a constitutive equation between the saturation and the suction. In addition, the new computer program entitled "COMVI3D-DY011" was created for the large deformation dynamic analysis of partially saturated elasto-viscoplastic soils.

In **Chapter 4**, the dynamic strain localization phenomenon in saturated and partially saturated clay was studied in the frame of finite deformation by using the multiphase mixture theory and the cyclic elasto-viscoplastic constitutive model. From the results the following concluding remarks can be made:

- In both saturated and unsaturated cases, the similar patterns of shear bands were observed. However, in partially saturated case the strain localized more prominently, and much clearer shear bands were formed.

- By comparing stress-strain relationships, it was found that in unsaturated case the peak strength was higher due to the suction. Also, it was seen that unsaturated soil reached the peak stress level in smaller axial strain.

- In unsaturated case more brittleness, i.e. strain softening, was observed due to the diminishing of suction force caused by shearing. It shows that even though suction improves the soil mechanical properties, i.e. increasing stiffness and shear strength, the hypothesis of saturated material, which is widely used in the analysis of geotechnical problems, is not at all for safety's sake since the partially saturated soil can experience diminishing of the suction which causes a drastic loss in strength.

- From the local stress-strain relationships, more brittleness was found inside the shear bands than outside of them.

- As the effect of initial suction, it was observed that in a certain value of initial suction, named critical suction (P_{cr}^{C}), shear strain was much more localized than that in other levels of suction. Furthermore, from the stress-strain relations it was seen that the shear strength increased with increasing in suction until the suction reached to the critical value (P_{cr}^{C}). Then, by increasing suction the strength dropped off to a lower value.

- As the effect of strain rate, it was observed that the lower strain rate led to the higher level of shear strain localization; besides, increasing strain rates produced greater peak values of the stress.

In **Chapter 5**, The different modes of failure affecting embankments as a consequence of earthquake shaking were presented and discussed. Furthermore, the seismic behavior of a partially saturated embankment on non-liquefiable soft clay was numerically studied in two cases with different ground water levels: First, the case in which the water level was considered at the surface of the ground, and second, the case in which the water level was taken below the soft clayey layer. The simulated failure had the same tendency as the ones observed in the real cases. In other words, the subsidence of the crest and lateral stretching in the body of the embankment were observed in the simulated results. By comparing the

results in the two cases, the case with unsaturated clayey layer showed higher amplification in acceleration responses. Moreover, from the distributions of accumulated viscoplastic shear strain in the embankment, higher levels of shear strain were seen in this case. In the case with fully saturated clayey layer, on the other hand, higher levels of horizontal displacements and larger settlement were observed.

6.2 Recommendation for future work

Based on the findings and results of this dissertation, the following topics are suggested for further investigation:

This research has majorly focused on the theoretical and numerical formulations. The proposed method can be easily applied to a wide range of geotechnical problems.

In this study strain localization phenomenon in partially saturated soils was analytically studied. In some cases the results were compared with experimental results. However, for the full validation of the method further experimental research on strain localization in unsaturated soils is required.

In the analysis of the dynamic strain localization in partially saturated soils, it is recommended to continue the analysis evaluating the effect of other relevant aspects, such as boundary conditions, material parameters, and aspect ratio of the specimen on the shear banding phenomenon. In addition, more analyses of case studies which are related to strain localization, such as excavations and slope failure, may be necessary in order to verify the proposed method.

In the present study, a van Genuchten type of soil water characteristic curve was adopted. In general, the soil water characteristic curve is dependent of the void ratio and the stress state, which are not considered in the van Genuchten formulations. Thus, it is desired to consider these features of the soil water characteristic curve in the analysis of unsaturated soil.

In chapter 5, the simulated failure was not severe compared to this type of damage observed in embankments during past large earthquakes due to the well compacted material used for the embankment. The severity of damage can be related to many factors such as the input waves, the material parameters, and the depth of the soft soil. Therefore, further study is still necessary to recognize the effects of these factors on this type of failure mode.

References

Adachi, T. and Oka, F. (1982). Constitutive equations for normally consolidated clay based on elasto-viscoplasticity, *Soils and Foundations*, **4**, 57–70.

Aifantis, E. C. (1984). On the microstructural origin of certain inelastic models, *ASME. Journal of Engineering Materials and Technology*, **106**(4), 326–330.

Aifantis, E. C., Oka, F., Yashima, A., and Adachi, T. (1999). Instability of gradient dependent elasto-viscoplasticity for clay, *International Journal for Numerical and Analytical Methods in Geomechanics*, **23**(10), 973–994.

Alonso, E. E., Gens, A., and Josa, A. (1990). A constitutive model for partially saturated soils, *Géotechnique*, **40**(3), 405–430.

Alshibli, K. A., Sture, S., Costes, N. C., Frank, M. L., and Lankto, M. R. (2000). Assessment of localized deformations in sand using X-ray computed tomography, *Geotechnical Testing Journal*, **23**(3), 274–299.

Atkin, R. J. and Craine, R. E. (1976). Continuum theories of mixtures: basic theory and historical developments, *The Quarterly Journal of Mechanics and Applied Mathematics*, **29**(2), 209–244.

Biot, M. A. (1941). Three-dimensional theory of consolidation, *Journal of Applied Physics*, **12**(2), 155–164.

Biot, M. A. (1956). Theory of propagation of elastic waves in a fluid saturated porous solid, (i): low frequency range, *International Journal of the Acoustical Society of America*, **28**, 168–178.

Biot, M. A. (1962). Mechanics of deformation and acoustic propagation in porous media, *Journal of Applied Physics*, **33**(4), 1482–1498.

Bishop, A. W. (1960). The measurement of pore pressure in the triaxial test, in *Proc. Conf. Pore Pressure and Suction in Soils*, Butterworths, London, 38–46.

Bishop, A. W. and Donald, I. B. (1961). The experimental study of partly saturated soil in the triaxial apparatus, in *Proc. 5th Int. Conference on Soil Mechanics and Foundation Engineering*, Paris, France, 13–21.

Bolzon, G., Schrefler, B. A., and Zienkiewicz, O. C. (1996). Elastoplastic soil constitutive laws generalized to partially saturated states, *Géotechnique*, **46**(2), 279–289.

Bowen, R. M. (1976). Theory of mixtures, in *Continuum Physics, Vol. III*, Eringen, A.C. ed. Academic Press, New York, 1–127.

Burland, J. B. (1990). On the compressibility and shear strength of natural clays, *Géotechnique*, **40**(3), 329–378.

Chaboche, J. L. and Rousselier, G. (1983). On the plastic and viscoplastic constitutive equations; part i and part ii, *J. Pressure Vessel Technol., Trans. ASME*, **105**(2), 153–164.

Coleman, J. D. (1962). Stress/strain relations for partly saturated soils, *Géotechnique*, **12**, 348–350.

Cormeau, I. C. (1975). Numerical stability in quasi-static elasto/viscoplasticity, *International Journal for Numerical Methods in Engineering*, **9**, 109–127.

Coussy, O. (2004). *Poromechanics*, John Wiley & Sons, London.

Cui, Y. J. and Delage, P. (1996). Yielding and plastic behavior of an unsaturated compacted silt, *Géotechnique*, **46**(2), 291–311.

Cunningham, M. R., Ridley, A. M., Dineen, K., and Burland, J. B. (2003). The mechanical behaviour of a reconstituted unsaturated silty clay, *Géotechnique*, **53**(2), 183–194.

Dafalias, Y. (1982). Bounding surface elastoplasticity-viscoplasticity for particulate cohesive media, in *Proc. of the IUTAM Sym. on Deformation and Failure of Granular Materials*, 97–107.

de Boer, R. (1998). Theory of porous media - past and present, *Zeitschrift fur Angewandte Mathematik und Mechanik*, **78**(7), 441–466.

de Borst, R. and Sluys, L. J. (1991). Localization in a cosserat continuum under static and dynamic loading conditions, *Computer Methods in Applied Mechanics and Engineering*, **90**(1-3), 805–827.

Ehlers, W. (2003). Continuum and numerical simulation of porous materials in science and technology chapter 9, in *Modeling and Mechanics of Granular and Porous Materials*, Capriz, G., Ghionna, V.N. and Giovine, P. eds. Birkhauser.

Ehlers, W. and Volk, W. (1998). On theoretical and numerical methods in the theory of porous media based on polar and non-polar elasto-plastic solid materials, *International Journal of Solids and Structures*, **35**(34,35), 4597–4617.

Ehlers, W., Graf, T., and Amman, M. (2004). Deformation and localization analysis of partially saturated soil, *Computer Methods in Applied Mechanics and Engineering*, **193**, 2885–2910.

Fillunger, P. (1936). Erdbaumechanik?, *Wien: Selbstverlag des Verfassers*.

Fredlund, D. G. and Morgenstern, N. R. (1977). Stress state variables for unsaturated soils, *Journal of the Geotechnical Engineering Division, ASCE*, **103**(GT5), 313–321.

Garcia, E., Oka, F., and Kimoto, S. (2010). Numerical analysis of a one-dimensional infiltration problem in unsaturated soil by a seepage-deformation coupled method, *International Journal for Numerical and Analytical Methods in Geomechanics*, **35**(5), 544–568.

GEER Association, . (2010). *website*, http://www.geerassociation.org, URL.

Gens, A. (1995). Constitutive laws, in *Modern Issue in Non-Saturated soils*, Gens, A., Jouanna, P. and Schrefler, B.A. eds. Vienam Austria. Sprinter, 129–158.

Hadamard, J. J. (1903). *Lecons sur la propagation des ondes et equations de l' hydrodynamique*, Libraire Scientifique A. Hermann, Paris.

Hall, S. A., Bornert, M., Desrues, J., Pannier, Y., Lenoir, N., Viggiani, G., and Bsuelle, P. (2010). Discrete and continuum analysis of localised deformation in sand using X-ray CT and volumetric digital image correlation, *Géotechnique*, **60**(5), 315–322.

Han, C. and Vardoulakis, I. (1991). Plane-strain compression experiments on water-saturated fine-grained sand, *Géotechnique*, **41**(1), 49–78.

Hardin, B. O. and Drnevich, V. P. (1972). Shear modulus and damping in soils: design equation and curves, *Journal of Soil Mechanics and Foundations, ASCE*, **98**(SM7), 667–692.

Harris, W. W., Viggiani, G., Mooney, M. A., and Finno, R. J. (1995). Use of stereophotogrammetry to analyze the development of shear bands in sand, *Geotechnical Testing Journal*, **18**(4), 405–420.

Hayano, K., Maeshiro, T., Tatsuoka, F., Sato, L., Wang, L., and Kodaka, T. (1999). Shear banding in a sedimentary soft mudstone subjected to plane strain compression, *Geotechnical Testing Journal*, **22**(1), 67–79.

Higo, Y., Oka, F., Kodaka, T., and Kimoto, S. (2006). Three dimensional strain localization of water-saturated clay and numerical simulation using an elasto-viscoplastic model, *Philosophical Magazine*, **86**, 3205–3240.

Higo, Y., Oka, F., Kimoto, S., Sanagawa, T., and Matsuhima, Y. (2011). Observation of microstructural changes and strain localization of unsaturated sands using microfocus X-ray CT, in *Proc. 9th International Workshop on Bifurcation and Degradation in Geomaterials*, Porquerolles Island, Provence, France.

Hoizumi, A. (1996). *Mechanical behavior of clay during cyclic loading and elasto-viscoplastic model*, Master thesis, Gifu University, (in Japanese).

Houlsby, G. T. (1997). The work input to an unsaturated granular material, *Géotechnique*, **47**(1), 193–196.

Hutchinson, J. W. (2001). Strain gradient plasticity theory revisited, *Material Science for 21st Century, The Society of Material Science, Japan*, **1A**, 307–315.

Ishihara, K. (1996). *Soil behavior in earthquake geotechnics*, Oxford University Press, UK.

Jennings, J. E. B. and Burland, J. B. (1962). Limitations to the use of effective stress in partly saturated soils, *Géotechnique*, **12**, 125–144.

Jommi, C. (2000). Remarks on the consitutive modeling of unsaturated soil, in *Experimental evidence and Theoretical Approaches in Unsaturated Soils*, Tarantino, A., and Mancuso, C. eds., Balkema, 139–153.

Kaliakin, V. N. and Dafalias, Y. F. (1990). Theoretical aspects of the elasto-plastic-viscoplastic bounding surface model for cohesive soils, *Soils and Foundations*, **30**(3), 11–24.

Katona, M. G. (1984). Evaluation of viscoplastic cap model, *Journal of Geotechnical Engineering, ASCE*, **110**(8), 1106–1125.

Khalili, N. and Khabbaz, M. H. (1998). A unique relationship for χ for the determination of the shear strength of unsaturated soils, *Géotechnique*, **48**(5), 681–687.

Kim, Y. S. (2004). Elasto-viscoplastic modeling and analysis for cohesive soil considering suction and temperature effects, Ph.D. thesis, Kyoto University, Department of Civil & Earth Resources Engineering.

Kimoto, S. and Oka, F. (2005). An elasto-viscoplastic model for clay considering destructuralization and consolidation analysis of unstable behavior, *Soils and Foundations*, **45**(2), 29–42.

Kimoto, S., Oka, F., Fushita, T., and Fujiwaki, M. (2007). A chemo-thermo-mechanically coupled numerical simulation of the subsurface ground deformations due to methane hydrate dissociation, *Computers and Geotechnics*, **34**, 216–228.

Kitakamigawa-Karyu River Office, . (2011). *Tohoku Regional Bureau*, Ministry of Land, Infratructure and Transport, Japan.

Kodaka, T., Higo, Y., and Takyu, T. (2001). Deformation and failure characteristics of rectangular specimens under three-dimensional condition, *Proc. 15th ICSMGE, Istanbul, Balkema*, **1**, 167–170.

Kodaka, T., Higo, Y., Kimoto, S., and Oka, F. (2007). Effects of sample shape on the strain localization of water-saturated clay, *International Journal for Numerical and Analytical Methods in Geomechanics*, **31**(3), 483–521.

Kogho, Y., Nakano, M., and Miyazaki, T. (1993). Theoretical aspects of constitutive modeling for unsaturated soils, *Soils and Foundations*, **33**(4), 49–63.

Kogho, Y., Asano, I., and Hayashida, Y. (2001). An elastoplastic model for unsaturated soils bases on cyclic plasticity, in *Proc, Int. Workshop on Deformation of Earth Materials*, Oka, F. ed., TC34 of ISSMGE. , Sendai, Japan, 129–140.

Kokusho, T., Yoshida, Y., and Esashi, Y. (1982). Dynamic properties of soft clays for wide strain range, *Soils and Foundations*, **22**, 1–18.

Kutter, B. L. and Sathialingam, N. (1992). Elastoviscoplastic modeling of the rate dependent behaviour of clays, *Géotechnique*, **42**, 142–164.

Lade, P. and Boer, R. (1997). The concept of effective stress of soil, concrete and rock, *Géotechnique*, **47**(1), 61–78.

Laloui, L. and Nuth, M. (2009). On the use of the generilised effective stress in the consitutive modelling of unsaturated soils, *Computers and Geotechnics*, **36**, 20–23.

Lambe, T. W. and Whitman, R. V. (1969). *Soil Mechanics*, John Wiley & Sons, New York.

Liang, L., Saada, A., Figueroa, J., and Cope, C. T. (1997). The use of digital image processing in monitoring shear band development, *Geotechnical Testing Journal*, **20**(3), 324–339.

Lloret, A. and Alonso, E. E. (1980). Consolidation of unsaturated soils including swelling and collapse behaviour, *Géotechnique*, **30**(4), 449–477.

Loret, B. and Khalili, N. (2000). A three phase model for unsaturated soils, *International Journal for Numerical and Analytical Methods in Geomechanics*, **24**, 893–927.

Loret, B. and Prévost, J. H. (1991). Dynamic strain localization in fluid-saturated porous media, *Journal of Engineering Mechanics*, **117**, 907–922.

Loret, B. and Rizzi, E. (1999). Strain localization in fluid-saturated anisotropic elastic-plastic porous media with double porosity, *Journal of the Mechanics and Physics of Solids*, **47**(3), 503–530.

Lu, N. and Likos, W. J. (2004). *Unsaturated soil mechanics*, John Wiley & Sons, New Jersey.

Maleki, M. and Cambou, B. (2009). A cyclic elastoplastic-viscoplastic constitutive model for soils, *Geomechanics and Geoengineering: an International Journal*, **4**(3), 209–220.

Matsui, T. and Abe, N. (1985). Elasto-viscoplastic constitutive equation of normally consolidated clay based on flow surface theory, in *Proc. of the 5th ICONMG*, A. A. Balkema, Rotterdam; Boston, 407–413.

Matsuo, O. (1996). Damage to river dikes, *Soils and Foundations*, 235–240.

Matsushima, T., Uesugi, K., Nakano, T., and Tsuchiyama, A. (2006). Effects of sample shape on the strain localization of water-saturated clay, in *Advances in X-ray tomography for geomaterials, Proc. of the Second International Workshop on X-ray CT for Geomaterials*, 255–261.

Matyas, E. L. and Radhakrishna, H. S. (1968). Volume change characteristics of partially saturated soils, *Géotechnique*, **18**, 432–448.

Michalowski, R. L. and Shi, L. (2003). Deformation patterns of reinforced foundation sand at failure, *J. Geotechnical and Geoenvironmental Engineering*, **29**(6), 439–449.

Mirjalili, M. (2010). Numerical analysis of a large-scale levee on soft soil deposits using two-phase finite deformation theory, Ph.D. thesis, Kyoto University.

Modaressi, H. and Laloui, L. (1997). A thermo-viscoplastic constitutive model for clays, *International Journal for Numerical and Analytical Methods in Geomechanics*, **21**, 313–335.

Mokni, M. and Desrues, J. (1998). Strain localization measurements in undrained plane-strain biaxial tests on Hostun RF sand, *Mechanics of Cohesive-Frictional Materials*, **4**(4), 419–441.

Mühlhaus, H. B. and Aifantis, E. C. (1991). A variational principle for gradient plasticity, *International Journal of Solids and Structures*, **28**(7), 845–857.

Muraleetharan, K. K. and Nedunuri, P. R. (1998). A bounding surface elastoplastic constitutive model for monotonic and cyclic behavior of unsaturated soils, in *Proceedings of 12th Engineering Mechanics Conference, ASCE, La Jolla, CA*, 1331–1334.

Muraleetharan, K. K. and Wei, C. F. (2000). A fully coupled analysis procedure for dynamic behavior of unsaturated soils, in *in Advances in Unsaturated Geotechnics, C.D. Shackelford, S.L. Houston, and N.-Y. Chang (Eds.), GSP No. 99, Proceedings, GeoDenver 2000 Conference, Geo-Institute, ASCE, Denver, Colorado*, 165–179.

Needleman, A. (1988). Material rate dependence and mesh sensitivity in localization problems, *Computer Methods in Applied Mechanics and Engineering*, **67**(1), 69–85.

Needleman, A. (1989). Dynamic shear band development in plane strain, *Journal of Applied Mechanics*, **56**(1), 1–9.

Nuth, M. and Laloui, L. (2008). Effective stress concept in unsaturated soils: Clarification and validation of a unified framework, *International Journal for Numerical and Analytical Methods in Geomechanics*, **32**, 771–801.

Oda, M. and Kazama, H. (1998). Microstructure of shear bands and its relation to the mechanisms of dilatancy and of dense granular soils, *Géotechnique*, **48**(4), 465–481.

Oda, M., Takemura, T., and Takahashi, M. (2004). Microstructure in shear band observed by microfocus X-ray computed tomography, *Géotechnique*, **54**(8), 539–542.

Ogisako, E., Nishio, S., Denda, A., Oka, F., and Kimoto, S. (2007). Simulation of triaxial compression tests on soil samples obtained from seabed ground in deep sea by elasto-viscoplastic constitutive equation, in *Proc. of the Seventh ISOPE Ocean Mining and Gas Hydrates Symposium, Lisbon, Portugal*, Chung and Komai eds. ISOPE, 63–68.

Oka, F. (1988). The validity of the effective stress concept in soil mechanics, in *Micromechanics of Granular Materials*, Satake, M. and Jenkins, J.T. eds. Elsevier Science Publihsers B.B., Amsterdam, 207–214.

Oka, F. (1992). A cyclic elasto-viscoplastic constitutive model for clay based on the non linear kinematic hardening rule, in *Proc. 4th. Int. Symposium on Numerical Model in Geomecahnics*, Pande, G.N. and Pietruszczak, S. eds., Swansea, UK, Balkema: Rotterdam, Vol. 1, 105–114.

Oka, F. (1996). Validity and limits of the effective stress concept in geomechanics, *Mechanics of Cohesive-Frictional Materials*, **1**, 219–234.

Oka, F. (2002). Effect of dilatancy on the strain localization of water-saturated elasto-viscoplastic soil, *International Jounal of Solids and Structures*, **39**, 3625–3647.

Oka, F. (2004). Thermo-hydro-mechanically coupled finite element analysis of cohesive soil using an elasto-viscoplastic model, in *Computational Mechanics (abstracts), WCCM 4 in conjuntion with APCOM'04*, Beijing, China.

Oka, F., Adachi, T., and Yashima, A. (1994). Instability of an elasto-viscoplastic constitutive model for clay and strain localization, *Mechanics of Materials*, **18**, 119–129.

Oka, F., Yashima, A., Adachi, T., and Aifantis, E. C. (1994a). Strain and pore water pressure localization in soft clay, in *Proc. Symp. on Material Instability, Theory and*

Applications, AMD-Vol. 183, MD-Vol. 50, ASME, Batra, R.C. and Zbib, H.M. eds., 11–18.

Oka, F., Yashima, A., Shibata, T., Kato, M., and Uzuoka, R. (1994b). FEM-FDM coupled liquefaction analysis of a porous soil using an elasto-plastic model, *Applied Scientific Research*, **52**, 209–245.

Oka, F., Adachi, T., and Yashima, A. (1995). A strain localization analysis using a viscoplastic softening model for clay, *International Journal of Plasticity*, **11**(5), 523–545.

Oka, F., Yashima, A., Tateishi, A., Taguchi, T., and Yamashita, S. (1999). A cyclic elasto-plastic constitutive model for sand considering a plastic-strain dependence of the shear modulus, *Géotechnique*, **49**(5), 661–680.

Oka, F., Yashima, A., Sawada, K., and Aifantis, E. C. (2000). Instability of gradient-dependent elasto-viscoplastic model for clay and strain localization, *Computer Methods in Applied Mechanics and Engineering*, **183**(1-2), 67–86.

Oka, F., Kodaka, T., Koizumi, T., and Sunami, S. (2001). An effective stress based liquefaction analysis based on finite deformation theory, in *Proc. 10th IACMAG, Tucson Arizona*, Balkema, 1113–1116.

Oka, F., Kodaka, T., Kimoto, S., Ishigaki, S., and Tsuji, C. (2003). Step-changed strain rate effect on the stress-strain relations of clay and a constitutive modeling, *Soils and Foundations*, **43**(4), 189–202.

Oka, F., Kodaka, T., and Kim, Y. S. (2004). A cyclic viscoelastic-viscoplastic constitutive model for clay and liquefaction analysis of multi-layered ground, *International Journal for Numerical and Analytical Methods in Geomechanics*, **28**, 131–179.

Oka, F., Kodaka, T., Kimoto, S., Ichinose, T., and Higo, Y. (2005). Strain localization of rectangular clay specimens under undrained triaxial compression conditions, in *Proc. 16th ICSMGE, Osaka*, Millpress science pub., Vol. 2, 841–844.

Oka, F., Kodaka, T., Kimoto, S., Kim, Y. S., and Yamasaki, N. (2006). An elasto-viscoplastic model and multiphase coupled FE analysis for unsaturated soil, in *Proceedings of the fourth International Conference on Unsaturated Soils*, Miller, G.A., Zapata, C.E., Houston, S.L. and Fredlund, D.G. eds. Geotechnical Special Publication, ASCE, Carefree, Arizona, Vol. 147(2), 124–131.

Oka, F., Feng, H., Kimoto, S., Kodaka, T., and Suzuki, H. (2008). A numerical simulation of triaxial tests of unsaturated soil at constant water and air content by using and elasto-viscoplastic model, in *Proc. of the First European Conference on Unsaturated Soils, E-UNSAT 2008, Durham*, Toll, D.G., Augarde, C.E., Gallipoli, D., and Wheeler, S.J. eds. Taylor and Francis Group; London, UK, 735–741.

Oka, F., Kodaka, T., Suzuki, H., Kim, Y., Nishimatsu, N., and Kimoto, S. (2010). Experimental study on the behavior of unsaturated compacted silt under triaxial compression, *Soils and Foundations*, **50**(1), 27–44.

Otani, J., Mukunoki, T., and Obara, Y. (2000). Application of X-ray CT method for characterization of failure in soils, *Soils and Foundations*, **40**(2), 111–118.

Perzyna, P. (1963). The constitutive equations for work-hardening and rate sensitive plastic materials, *Proc. Vibrational Problems*, **4**(3), 281–290.

Pierce, D., Shih, C. F., and Needleman, A. (1984). A tangent modulus method for rate dependent solids, *Computers and Structures*, **18**, 875–887.

Prévost, J. H. and Loret, B. (1990). Dynamic strain localization in elasto-(visco)-plastic solids, part 2: plane strain examples, *Computer Methods in Applied Mechanics and Engineering*, **83**, 275–294.

Rampello, S. (1991). Some remarks on the mechanical behaviour of stiff clays: the example of todi clay, experimental characterization and modeling soils and soft rocks, in *Proc. of Workshop on Experimental Characterization and Modelling of Soils and Soft Rocks, Naples*, 131–186.

Rechenmacher, A. L. and Medina-Cetina, Z. (2003). Digital-imaging based measurement of deformed shapes of axisymmetric soil specimens, in *Proc. 16th ASCE Engineering Mechanics Conference, Seattle, WA, USA*.

Rice, J. R. (1975). On the instability of dilatant hardening for saturated rock masses, *Journal of Geophysical Research*, **80**(11), 1531–1536.

Rice, J. R. (1976). The localization of plastic deformation, in *Theoretical and Applied Mechanics, Proc. of 14th ICTAM Symposium*, W. T. Koiter ed., North-Holland, Amsterdam, 207–220.

Sawada, M. (2008). *A cyclic elasto-viscoplastic constitutive equation and visualization of microstructures for soils*, Master thesis, Kyoto University, (in Japanese).

Schrefler, B. A. and Gawin, D. (1996). The effective stress principle: incremental of finite form, *International Journal for Numerical and Analytical Methods in Geomechanics*, **20**(11), 785–814.

Schrefler, B. A., Majorana, C. E., and Sanavia, L. (1995). Shear band localization in saturated porous media, *Archives of Mechanics*, **47**(3), 577–599.

Sheng, D., Sloan, W., Gens, A., and Smith, D. W. (2003). Finite element formulation and algorithms for unsaturated soils part i: Theory, *International Journal for Numerical and Analytical Methods in Geomechanics*, **27**, 745–765.

Simons, N. E. and Menzies, B. K. (1974). A note on the principle of effective stress, *Géotechnique*, **24**, 259–262.

Terzaghi, K. (1936). The shearing resistance of saturated soils and the angle between the planes for shear, in *International Conference on Soil Mechanics and Foundation Engineering*, Harvard University Press; Cambridge, MA., 54–56.

Terzaghi, K. (1943). *Theoretical soil mechanics*, John Wiley & Sons.

Thomas, H. R. and He, Y. (1998). Modeling the behaviour of unsaturated soil using and elastoplastic constitutive model, *Géotechnique*, **48**(5), 589–603.

Van Genuchten, M. T. (1980). A closed-form equation for predicting the hydraulic conductivity of unsaturated soils, *Soil Science Society of America Journal*, **44**, 892–899.

Wang, G. X. and Kuwano, J. (1999). Modeling of strain dependency of shear modulus and damping of clayey sand, *Soil Dynamics and Earthquake Engineering*, **18**, 463–471.

Watanabe, T., Oka, F., Kimoto, S., Higo, Y., and Yabuki, T. (2007). Simulation of cyclic triaxial tests of unsaturated silt by elasto-viscoplastic model, in *Proc. 62th Annual Meeting of JSCE, Hiroshima*, 211–212, (in Japanese).

Wheeler, S. J. and Karube, D. (1996). State of the art report: Constitutive modeling, in *Proc. 1st Int. Conference on Unsaturated Soils, Paris*, Alonso, E. E. and Delage, P. eds. Balkema, Rotterdam, Vol. 3, 1323–1356.

Wheeler, S. J. and Sivakumar, V. (1995). An elasto-plastic critical state framework for unsaturated soil, *Géotechnique*, **45**(1), 35–53.

Wheeler, S. J., Sharma, R. S., and Buisson, S. R. (2003). Coupling of hydraulic hysteresis and stress-strain behaviour in unsaturated soils, *Géotechnique*, **53**(1), 41–54.

Yin, J. H. and Graham, J. (1999). Elasto visco-plastic modelling of the time-dependent stress-strain behavior of soils, *Canadian Geotechnical Journal*, **36**(4), 736–745.

Yong, R. N. and Japp, R. D. (1969). Stress-strain behavior of clays in dynamic compression, *Vibration effects of earthquakes on soils and foundations, ASTM Special Technical Publication*, **450**, 233–262.

Yoshida, T., Tatsuoka, F., Siddiquee, M. S. A., Kamegai, Y., and Park, C. S. (1994). Shear banding in sands observed in plane strain compression, in *Proc. 3rd Int. Workshop on Localization and Bifurcation Theory for Soils and Rocks*, Grenoble, Chambon, R., Desrues, J. and Vardoulakis, I. eds., Balkema, 165–179.

Yoshimine, M. (2003). *2003 Tokachi-oki Earthquake, Hokkaido, Japan*, Earthquake Image Archives, http://geot.civil.metro-u.ac.jp/archives/eq/.

Yoshimine, M. (2011). *2011 off the Pacific coast of Tohoku Earthquake, Japan*, Earthquake Image Archives, http://geot.civil.metro-u.ac.jp/archives/eq/.

Zbib, H. M. and Jubran, J. S. (1992). Dynamic shear banding: a three-dimensional analysis, *International Journal of Plasticity*, **8**(6), 619–641.

Zhang, H. W. and Schrefler, B. A. (2000). Gradient-dependent plasticity model and dynamic strain localisation analysis partially saturated porous media: one dimensional model, *European Journal of Mechanics - A/Solids*, **19**(3), 503–524.

Zhang, H. W., Sanavia, L., and Schrefler, B. A. (2001). Numerical analysis of dynamic strain localisation in initially water saturated dense sand with a modified generalized plasticity model, *Computers and Structures*, **79**(4), 441–459.